Volume 1 | Issue 2 | July - December 2025

# TRANSLATIONAL CHEMISTRY

## AN INTERFACE JOURNAL



PROTEOMASS SCIENTIFIC SOCIETY

Translational Chemistry
An Interface Journal

## Editorial Board



## Review Article



## Original Article

# EDITORIAL BOARD

TRANSLATIONAL CHEMISTRY
AN INTERFACE JOURNAL
HTTPS://WWW.TRANSLATIONALCHEMISTRY.COM/


EDITORIAL BOARD | DOI: 10.5584/translationalchemistry.v1i2.246

# TRANSLATIONAL CHEMISTRY

## *AN INTERFACE JOURNAL*

## Associated Editors

REVIEW ARTICLE

TRANSLATIONAL CHEMISTRY
AN INTERFACE JOURNAL
HTTPS://WWW.TRANSLATIONALCHEMISTRY.COM/

REVIEW ARTICLE | DOI: 10.5584/translationalchemistry.v1i2.247

# Colloidal Metallic Nanoparticles: An Introduction to Concepts and Properties

Silvia Nuti[1,†,*], Carlos Lodeiro[1,2,*]

[1]BIOSCOPE Research Group, LAQV-REQUIMTE, Chemistry Department, NOVA School of Science and Technology (FCT NOVA), Universidade NOVA de Lisboa, 2829-516 Caparica, Portugal. [2] PROTEOMASS Scientific Society, 2825-466, Costa da Caparica, Portugal. [†] Current address: Department of Chemistry "Giacomo Ciamician", University of Bologna, Via Gobetti 85, 40129 Bologna, Italy.

**Received:** 11 November 2025 **Accepted:** 22 November 2025 **Available Online**: 5 December 2025

## Abstract

Metallic nanoparticles (NPs) exhibit size- and shape-dependent properties that have positioned them at the forefront of nanoscience and nanotechnology. Their synthesis spans top-down and bottom-up approaches, including direct, seed-mediated, and composite strategies, each offering distinct advantages and limitations. Understanding nucleation, growth, and stabilization processes is essential to control morphology and functionality, which in turn govern their optical, catalytic, and biological behaviours. This introductory review provides a didactic overview of metallic NPs synthesis, highlighting the connection between structure and properties. Integrating historical context, theoretical principles, and practical examples, this review outlines the key concepts linking the synthesis, structure, and behaviour of metallic NPs.

**Keywords:** Noble metals, Nanoparticles, Synthesis, Colloids, Didactic

## 1. Introduction and historical perspective

Metals, such as Gold (Au), Silver (Ag), Platinum (Pt), Copper (Cu), have been used since antiquity, when they were prized for their ornamental and economic value and for their supposed healing powers [1–4]. When these materials are brought to the nanoscale range ($10^{-9}$ m), they form structures called NP (from Ancient Greek "νᾶνος" (nânos), meaning "*dwarf*") which exhibit different properties when compared to the bulk metals, the most evident and captivating change is seen in the variation of the colour. Throughout history, several examples of the use of nanomaterials are reported. Cu and Ag nanocrystals were found in glazed pottery created by artisans in the Middle East in the 9$^{th}$ century [5]. Soluble Au was believed to have impressive curative properties, and its preparation and applications are described in two books dating back to 1618 and 1676 [6,7]. Au and Ag NPs of different sizes are the origin of the astonishing stained glass works: firstly developed in Ancient Egypt and Ancient Rome, the peak of the stained-glass windows creation was reached during the Middle Ages in the 12$^{th}$ century [8,9]. However, the finest example of the use of nanomaterials in antiquity is represented by the Lycurgus cup, a Roman cage cup-type vessel dating back to 4th century. Due to the presence of Au-Ag alloyed NPs, it exhibits different colour depending on the illumination (**Figure 1**): when it is illuminated from outside, and light is reflected, it appears green, while, when it is illuminated from the inside, and the light is transmitted, the cup displays a red colour [10].


**Figure 1.** Lycurgus Cup (British Museum, London). When viewed in reflected light, it appears green (A). However, when the light is transmitted through the glass, it appears red (B). 

It was in 1857 that the observation of metallic NPs was described by the English scientist Michael Faraday in his Bakerian Lecture [11]. He was, in fact, able to obtain a ruby coloured solution and described how the colour was produced by fine particles of Au

***Corresponding author:** Silvia Nuti, silvia.nuti3@unibo.it; s.nuti@campus.fct.unl.pt | Carlos Lodeiro, cle@fct.unl.pt

which are "very minute in their dimensions", even though he could not observe them with the microscopes available at the time [12]. Almost one hundred years later, in 1951, John Turkevich and his colleagues observed the Au colloids with an electron microscope [13]. Faraday also noted that "the particles are easily rendered evident, by gathering the rays of the sun (or a lamp) into a cone by a lens, and sending the part of the cone near the focus into the fluid; the cone becomes visible, and though the illuminated particles cannot be distinguished because of their minuteness, yet the light they reflect is golden in character, and seen to be abundant in proportion to the quantity of solid gold present."[11] observing the so-called Tyndall effect, also extensively studied in the same time frame by the Irish physicist John Tyndall.

Later on, in 1908, another important contribution to the growth of nanotechnology came from the German physicist Gustav Mie [14]. Mie theory is based on solving Maxwell's equations for electromagnetic waves interacting with a spherical particle. It describes the scattering and absorption of light by spherical particles whose size is comparable to or larger than the wavelength of the incident light and as NPs dimensions often fall within this range, the theory is particularly useful for their study. The interest towards nanotechnology and the synthesis of NPs with different composition, morphology and applications has increased significantly with a huge and constantly increasing number of documents published on this topic.

## 2. Synthesis of Metallic NPs

The synthesis of NPs holds immense importance in various fields of science and technology. The controlled synthesis of NPs enables researchers to tailor their size, shape, composition, and surface properties, allowing for precise manipulation of their characteristics and functionalities. Metallic NPs, with their unique physical and chemical properties, offer important opportunities for advancements in different areas such as medicine, electronics, energy, and environmental remediation.

### 2.1. Top-down and bottom-up approaches

The approaches for synthesising metallic NPs can be divided in two greater categories: "*top-down*" and "*bottom-up*" [15,16]. "*Top-down*" synthesis is based on the reduction of bulk materials, such as larger particles or bulk powders, to NPs through controlled mechanical, physical or chemical processes. Some of the most commonly used techniques are ball milling, mechanochemical synthesis, sputtering or laser ablation, where external forces are applied to reduce the size of the material or to induce reactions at the surface of the bulk reagents. On the other hand, "Bottom-up" synthesis focuses on building NPs from atomic or molecular precursors, gradually assembling them into the desired nanostructures. This approach includes many techniques in solid state (physical vapor deposition or chemical vapor deposition), liquid state (sol gel methods, chemical reduction, hydrothermal method, solvothermal method), gas phase (spray pyrolysis, laser ablation, flame pyrolysis) and other methods including biological synthesis, microwave or ultrasound techniques. One of the most common methodologies among the "*bottom-up*" approaches is the chemical reduction method or also called wet colloidal synthesis, in which NPs are synthesized by controlling chemical reactions in a solution. This process evolves through two different phases: nucleation and growth.

### 2.2. Nucleation and Growth of Metallic NPs in Solution

The nucleation and growth processes are the steps involved in the colloidal synthesis of metallic NPs [17,18].

#### 2.2.1. *Nucleation*

Nucleation is a thermodynamic step that leads to the formation of tiny clusters (or nuclei) from precursor species in solution. This can be initiated by, for example, the addition of a reducing agent or temperature variations. Nucleation can be distinguished by the way it occurs:

- *Heterogeneous nucleation* occurs at preferential sites such as, phase boundaries, impurities or surfaces or particles present in the system that act as nucleation sites and typically requires a lower amount of energy to be initiated.
- *Homogeneous nucleation* occurs when nuclei form spontaneously in the reaction solution. It requires a higher amount of energy together with other conditions such as supersaturation.

Nucleation is mainly explained by the Classical Nucleation Theory (CNT) [19] in which, for a spherical particle of radius *r*, the total free energy ΔG, is given by the sum of the surface energy $\gamma$ and the free energy of the bulk crystal $\Delta G_v$ (Equation 1):

$$\Delta G = 4\pi r^2 \gamma + \frac{4}{3}\pi r^3 \Delta G_v \qquad (1)$$

The free energy of the crystal, $\Delta G_v$ (Equation 2), is governed by parameters such as temperature (T), Boltzmann's constant ($k_B$), the supersaturation of the solution (S) and its molar volume (v) (Equation 3).

$$\Delta G_v = \frac{-k_B T \ln \ln (S)}{v} \qquad (2)$$

$$S = \frac{C_{actual} - C_{equilibrium}}{C_{equilibrium}} \qquad (3)$$

Because the surface free energy is positive while the crystal free energy is negative, it is possible to find a maximum free energy corresponding to a critical cluster size. The critical radius of the nucleus identifies to the minimum size required for a particle to persist in the solution without undergoing re-dissolution. Conversely, when clusters exceed the critical radius *r*, growth becomes favourable (**Figure 2**). The critical radius is expressed as follows in Equation 4:

$$r_{crit} = -\frac{2\gamma}{\Delta G_v} \qquad (4)$$

By substituting *r* in Equation 1 with critical radius from Equation 4 it is possible to obtain the expression for the critical free energy $\Delta G_C$ (Equation 5):

$$\Delta G_{crit} = \frac{16\pi\gamma^3}{\Delta G_v^2} \quad (5)$$

Consequently, nucleation can be promoted by increasing the supersaturation level, resulting in a reduction of the energy barrier for nucleation and raising the temperature, which increases the average atomic energy and facilitates the overcoming of critical energy or by introducing a change in surface free energy, achievable through the use of surfactants.

2.2.2. *Growth*

Different theories have been proposed to describe the growth of NPs following nucleation. Some theories explain the growth of NPs as atom-mediated while other as NPs-mediated. In the former, the atoms act as building blocks that aggregate on the surface of a growing nucleus, contributing to its expansion, while the latter theory involves the addition of pre-existing NPs as the fundamental units for further growth. The most representative theories are summarized below:

- *LaMer* mechanism was one of the first nucleation and growth theory to be proposed and is based on the CNT [20]. Developed for a closed system, this model describes the formation of NPs in three stages: first, an increase in the concentration of available monomers within the solution which initiates the second stage, a phenomenon called "burst nucleation," resulting in a substantial decrease of free monomers in the solution (**Figure 3**). The nucleation rate during this phase is characterized as "effectively infinite", causing minimal nucleation activity thereafter due to the diminished concentration of monomers, lastly growth continues controlled by the diffusion of monomers through the solution.
- *Ostwald and digestive ripening* are mechanisms that propose to explain the growth of NPs in solution. Ostwald ripening [21] (**Figure 4A**) occurs due to differences in solubility and surface energy between larger and smaller particles. Larger particles have lower surface energy and are more thermodynamically stable, leading to the preferential dissolution of smaller particles and subsequent growth of larger ones. On the other hand, digestive ripening [22] (**Figure 4B**) happens when bigger NPs dissolve and the smaller ones grow. Digestive ripening can be initiated with the addition of a ligand that will help the dissolution of the bigger particles. With the equilibrium of the two process a more uniform size distribution is achieved.
- *Coalescence and Oriented attachment* are two mechanisms that explain the growth of nanocrystals as "nanoparticle-mediated growth", that occurs when smaller NPs, created in the initial stages of the reaction, merge to create bigger NPs. For *coalescence* [23] (**Figure 5**) there is no preferred merging site for the NPs that will coalesce upon contact. Conversely, for *oriented attachment* [24] (**Figure 6**) to happen, the NPs must present matching crystallographic planes. This mechanism might occur following collisions of aligned nanocrystals in suspension or when misaligned NPs will rotate towards a low-energy interface configuration.

### 2.3. Stability of NPs

Once NPs are synthesised, their stability in solution refers to the ability of colloidal particles to remain dispersed in a medium without aggregating or settling over time. Stability of NPs is crucial for maintaining their properties and it is also important for their further application. Multiple parameters govern colloidal stability, including van der Waals (vdW) attraction, electrostatic double-layer (EDL) repulsion, particle-size distribution, pH, temperature, surface chemistry, and steric effects [25]. vdW attractive forces (**Figure 7A**) result from the interaction of induced, instantaneous or permanent dipoles in between NPs and tend to destabilize the colloidal dispersion. These attractive forces are counteracted by electrostatic repulsion generated by the NPs EDL (**Figure 7B**).

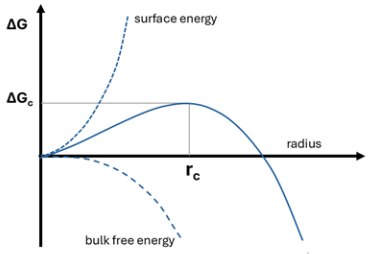


**Figure 2.**The dependence of the cluster free energy, on the cluster radius, according to the CNT.

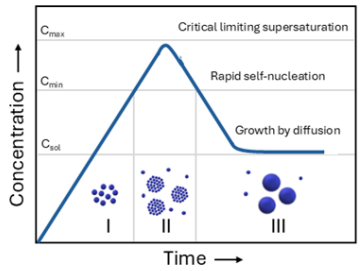


**Figure 3.** The principle of nanoparticle nucleation due to LaMer's mechanism of nucleation derived from CNT.

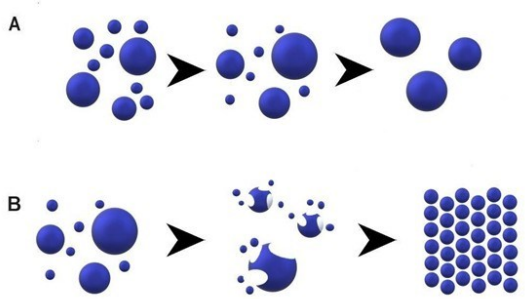


**Figure 4.** Representation of the (A) Ostwald ripening and (B) digestive ripening processes.

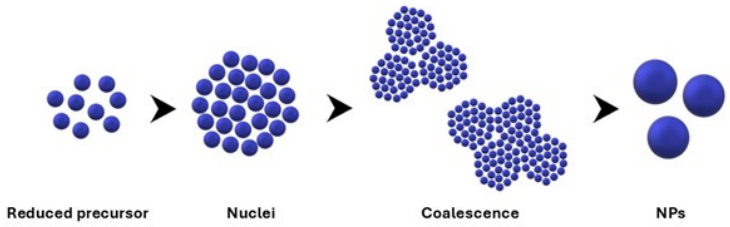


**Figure 5.** Representation of coalescence in the synthesis of NPs.

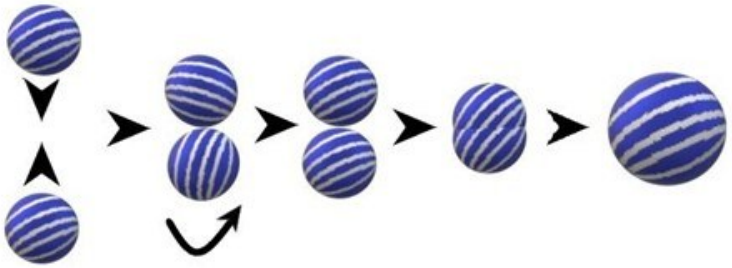

**Figure 6.** Representation of an oriented attached mechanism.

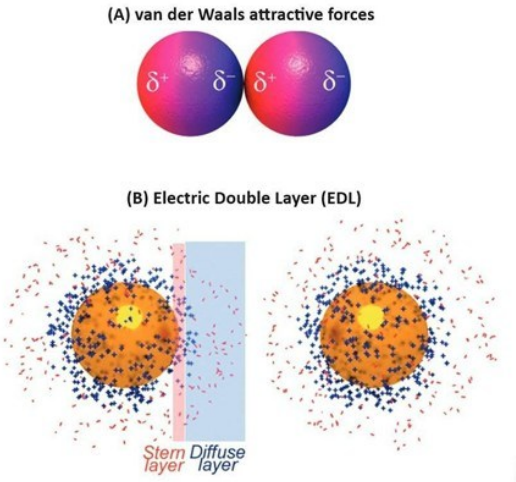


**Figure 7.** (A) Representation of Van der Waals interactions that can lead to nanoparticle aggregation. (B) Representation of the EDL, composed by the Stern layer and the Diffuse layer. Adapted with permission from reference [25]. Copyright 2015 Royal Society of Chemistry under a CC BY 3.0 License https://creativecommons.org/licenses/by/3.0/.

The EDL is formed by the Stern-layer and the diffuse layer. The surface charge of NPs, originating from surface ions or functional groups, leads to the creation of the Stern layer formed by ions with opposite charges adhering to the NP surface. The diffuse layer is formed by ions carrying a charge opposite to that of the Stern layer. The EDL results in a net charge, and when two similar particles are in proximity, the EDL causes repulsion between them. The Derjaguin–Landau–Verwey–Overbeek (DLVO) theory uses vdW forces and EDL to predict and explain NPs stability. The DLVO theory also includes contribution of pH and ionic strength of the medium. Steric stabilization (**Figure 8**), obtained through the adhesion of molecules (polymers, proteins, surfactants...) to the NPs surface, becomes a valuable tool in maintaining the dispersion of NPs, especially in challenging conditions, as it prevents the formation of attractive vdW interactions between two particles. The stability is now determined by the solubility of the molecules, average chain length, concentration or temperature. Steric stabilization will be ineffective if the obtained coating is patchy or incomplete.

### 2.4. Direct synthesis

Direct synthesis (also known as "one-pot") is the most straightforward method to synthesise metallic NPs in solution. This approach combines nucleation and growth happening simultaneously and in the same vessel. The metal precursor is reduced, and the newly formed NPs need to be stabilized by a capping agent present in the solution. One of the most commonly reproduced one-pot syntheses is the Turckevich synthesis. Firstly reported in 1951 [13], it involves the use of tetrachloroauric(III) acid ($HAuCl_4$), which is reduced and stabilized by trisodium citrate at 100 °C in water, for the preparation of spherical Au NPs with a diameter of approximately 20 nm.

Early reports of one-pot synthesis of Ag NPs, where the reduction of the metal precursor ($AgNO_3$) is achieved using sodium borohydride ($NaBH_4$) showed a less uniform size and shape distribution [26]. More recently, the one-pot synthesis of monodisperse Ag NPs, of approximately 10nm, was reported [27]. This methodology utilizes a combination of sodium citrate and tannic acid as reducing agents for $AgNO_3$. It is also possible to obtain Pt NPs via a one-pot methodology [28]. In this case the reduction of the metal precursor, hexachloroplatinic acid ($H_2PtCl_6$) is achieved with a combination of acetylthiocholine (ATC) and $NaBH_4$. While direct synthesis methodologies are popular due to their simplicity, they often lead to NPs with a spherical morphology, thus, to obtain a higher degree of control over morphology and sizes of NPs it is necessary to resort to seed-mediate syntheses.

### 2.5. Seed-mediated synthesis

In seed-mediated syntheses methodologies, pre-formed particles are used as "seeds" and act as nucleation sites for the formation of the desired NPs. Typically, this methodology allows for a finer tuning of the NPs size and morphology. One of the first reported examples is the synthesis of Au nanorods [29] starting from pre-formed Au spherical seeds and utilizing cetyltrimethylammonium bromide (CTAB) as a surfactant for the formation of the rod-shaped NPs. Shortly after, the synthesis of Ag nanowires using pre-formed Pt seeds and a polyol process, was reported [30]. This approach is also applicable to spherical NPs. Starting from seeds obtained with a one-pot methodology, researchers have been able to grow Ag and Au spherical NPs [27,31] with a great control over their size distribution. Proceeding after the first step, and using the previously grown NPs as seeds, the process has been extended to several NPs generations obtaining spheres up to 200 nm. However, a greater understanding of the nature of the seeds and an appropriate choice of capping agents and surfactants, can lead to the synthesis of a broader variety of morphologies [32].

A seed can be characterized by two elements: the internal structure (or crystallinity) defined by planar defects such twin planes or stacking faults, and the surface structure (or faceting). Most noble metals crystallize in the face centred cubic (fcc) lattice, which can be explained as the stacking of closely packed, hexagonal arrays of atoms along the (111) direction.

- *Single-crystal seeds* do not present any planar defects and consists of only one single-crystal domain. They can be obtained when a strong reducing agent is used for their preparation.
- *Singly twinned seeds* present one planar defect, a (111) plane that serves as a twin boundary dividing the seed in two crystal domains. Metals such as Cu, Ag, Au often produce this type of seeds.
- *Multiply twinned* seeds are characterized by the presence of more than one twin defect. This type of seeds can be helpful in the synthesis of highly anisotropic NPs, thanks to the in-homogeneous distribution of the defects.
- *Plate-like seeds* are generated when stacking fault defects are present. The synthesis of this type of seeds is more intricate, due to the necessity of having a kinetic control over the growth of the NPs. Slow deposition of the atoms, use of mild reducing agents and the use of strong ligands are some of the favoured strategies [32].

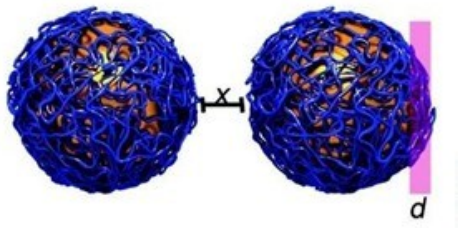


**Figure 8.** Representation of NPs covered with a polymer avoiding particle interaction due to steric repulsion. Adapted with permission from reference [25]. Copyright 2015 Royal Society of Chemistry under a CC BY 3.0 License https://creativecommons.org/licenses/by/3.0/.

Capping agents also influence the homogeneous nucleation over a pre-formed seed. Some molecules bind strongly to certain metals while other have a weaker interaction (for example, citrate will weakly bind to Au, while thiols will have a much stronger interaction). The combination between the affinity of a capping agent for a metal/specific facet will have an influence on the growth of the final NPs, as a facet that is selectively capped will be more expressed during the growth [32].

Seed-mediated protocols provide a wide range of potential morphologies beyond the nanorods and spheres mentioned earlier. Additional morphologies achievable through seed-mediated syntheses include nanoplates [33], nanocages or nanoframes [34], and branched NPs (also referred to as nanostars, nanoflowers, multipods or dendritic NPs, based on the branches number and distribution) [35]. Nanoplates represent an important class of anisotropic nanostructures distinguished by their pseudo-two-dimensional morphology with large lateral dimensions compared to thickness. One of the earliest reported examples is photoinduced method for the conversion of Ag nanospheres into triangular nanoprisms. In this process, light irradiation induces the fragmentation of spherical Ag NPs into small clusters that contribute to the growth of nanoprisms, acting as seeds, until all precursors are consumed. [36]. Around the same period truncated Ag nanoplates have been prepared through a soft-template approach using CTAB micelles [37] while PVP-assisted syntheses enabled the formation of nanoplates of other metals such as Au and Pd [37]. The formation of these plate-like structures has been associated with the presence of planar twin defects along the (111) crystallographic planes, which break the symmetry of the face-centred cubic lattice and promote two-dimensional growth. Additionally, selective ligand adsorption on specific crystal facets stabilizes the basal planes and restricts growth along the perpendicular direction, further favouring the plate morphology. One of the most striking features of this materials, when synthesised with plasmonic metals such as Au and Ag, is the possibility of tuning the LSPR band over an extensive range, from the visible to the infrared, by tuning the aspect ratio of the nanoplates by changing the synthesis conditions [38–40], making them ideal candidates for sensing applications [39].

Nanocages are a unique class of hollow nanostructures characterized by high surface-to-volume ratio, accessible inner cavities, internal and external surfaces and porous walls. hey are most commonly synthesized through galvanic replacement reactions, where a less noble metal is oxidized and dissolved while a more noble metal is reduced and deposited onto its surface. In one of the first reported examples [41] Ag nanostructures were used as templates and reacted with $HAuCl_4$, where Ag was oxidized to $Ag^+$ while $Au^{3+}$ was reduced and deposited on the template surface, forming hollow Au shells after the complete consumption of Ag. The morphology, wall thickness, and void size of the resulting hollow structures were dictated by the size and shape of the Ag templates. This methodology was later extended to other noble metals, such as Pt and Pd, to further demonstrate the potential of this approach which was subsequently adopted for the synthesis of [42] both single- and double-shell nanocages (Au-Pt, Pt-Au, Au-Pd, Pd-Au, Pd-Pt, and Pt-Pd) via sequential galvanic replacement steps. The optical and plasmonic characteristics of these hollow nanocages were found to depend strongly on the dielectric properties and shell thicknesses of the constituent metals. More recently, a seed-mediated method combining Pd nanocube templates, Pt-Ru deposition, and subsequent chemical etching to obtain multimetallic PdPtRu nanocages was reported [43]. The resulting nanocages exhibited open, hollow structures with tunable compositions and demonstrated significantly enhanced catalytic activity and durability. Overall, galvanic replacement and related template-mediated strategies have proven to be powerful synthetic routes for producing nanocages with controllable morphology, wall thickness, and composition. These advances have established nanocages as versatile materials for applications in catalysis, plasmonics, and energy conversion.

Branched NPs have been obtained with different metal precursors. Ag nanoflowers have been obtained from the reduction of $[Ag(NH_3)_2]^+$ by ascorbic acid, in the presence, polyvinylpyrrolidone (PVP) as stabilizer, trisodium citrate and employing single crystalline silver seeds [44]. Pd nanostars were obtained using a two -step seeded growth process, using $PdCl_4^{2-}$ as precursor, ascorbic acid as reducing agent, CTAB as stabilizer, and copper (II) acetate to promote the anisotropic growth of different morphologies depending on its concentration [45]. For Pt, different methodologies have been reported, either using Pt seeds [46] in presence of PVP to produce single crystal NPs or Au seeds [47] to catalyse the thermal decomposition of $PtCl_2$ in oleylamine. Rh multipods have been prepared with the reduction of $RhCl_3$ in ethylene glycol in presence of PVP using Rh seeds [48].

Great research effort has been dedicated to creating branched Au NPs, thank to their intense and highly tunable Localized surface plasmon resonance band (LSPR), enabling applications in different fields [49]. One of the first report of Au branched NPs involved the use of PVP in dimethylformamide (DMF) both as reducing and stabilizing agent and PVP coated seeds [50]. Following the first reports on the role of $AgNO_3$ as shape inducing agent for the synthesis of Au nanorods[51,52], a similar methodology has been applied for the synthesis of branched Au NPs in combination with the use of surfactants such as CTAB [53,54]. The use of branched NPs in sensing and biomedical applications has been limited by the potential toxicity of surfactants like CTAB, and by the difficulty of replacing the stabilizing agents (i.e: PVP, CTAB), for further functionalization. Surfactant-free synthesis can help to advance in the bioapplication of branched NPs. Such syntheses are for example obtained with sodium citrate and hydroquinone, ascorbic acid or albumin [55–57]. Anisotropic metal NPs represent a highly versatile class of nanostructures whose design has evolved from spheres and rods to more complex morphologies such as nanoplates, nanostars, nanocages, multipods, and chiral or hierarchical architectures. The emergence of such complex architectures further illustrates the structural diversity attainable through colloidal synthesis. The ability to modulate shapes and composition at the nanoscale enables fine control of optical, catalytic, and electronic responses, supporting applications that span from SERS and chemical sensing to photocatalysis, photothermal therapy, and energy conversion [58].

### 2.6. Synthesis of Composite NPs

Composite NPs possess a structure comprising two or more components at the nanoscale, each exhibiting distinct physical and/or chemical properties. These components possess mutual contact interfaces, leading to a strong coupling effect on a nanometer scale. Composite NPs can combine the effects of individual components or enhance intrinsic performance and exhibit novel features, surpassing the limitations of single-component properties. Examples of composite NPs studied in this thesis work include bimetallic NPs in core@shell or alloyed morphology and metal@oxide core@shell NPs such as metallic NPs with a bulk or mesoporous silica ($SiO_2$) shell.

2.6.1. *Bimetallic NPs*

Bimetallic NPs can be synthesised in solution with similar approaches compared to their mono-metallic counterparts ("*top-down*" or "*bottom-up*" approach and direct or seed-mediated syntheses). The presence of the two metallic precursors will determine the final composition of the particles [59]. For the "*bottom-up*" approach, if the two precursors are reduced simultaneously, it is likely that the NPs will present an alloyed structure (**Figure 9A**). The two metals might be present in a statistical mixture [60] or some zones of the particles might exhibit a richer composition of one of the two metals without complete segregation [61]. Conversely, if the second metal precursor is added to a pre-formed particle (like in a seed mediated synthesis) different outcomes are possible:

- *Formation of a core@shell structure:* In this case the second metal will be reduced on the surface of the NPs creating a shell that can be continuous or patchy (**Figure 9B**).
- *Formation of a hollow structure:* This process is also referred to as "galvanic replacement" and it consists of a redox process between the pre-formed metallic NPs (sacrificial template), and metal ions in solution. The difference in the electrical reduction potential between the sacrificial template and the metal ions in solution provides the driving force for the reaction in which the template will undergo oxidation and dissolution while the second metal ions will reduce and deposit at the surface of the template. The resulting hollow NPs will have a composition richer in the second metal. Carefully tuning the relationship between the two metal can lead to different compositions of the hollow structures (**Figure 9C**) [62,63].

Bimetallic NPs can also by synthesised through "*top-down*" methodologies, an example of this is the laser ablation method in which a bulk alloy is irradiated with a laser to obtain bimetallic NPs (**Figure 9D**) [64–66]. With this methodology it is also possible to obtain ligand-free NPs [67].

2.6.2. *Noble metal@oxide core@shell NPs*

Controllable integration of different materials such as noble metals (Au, Ag, Pt, and Pd) and oxides ($SiO_2$, $TiO_2$, $CeO_2$, $Cu_2O$, $Fe_2O_3$, ZnO, $SnO_2$ and $ZrO_2$ [68–70] ) into a single nanostructure has recently become a popular research topic as these nanostructures not only combine the function of individual NPs, but also bring unique collective and synergetic properties compared with single-component materials [71]. Moreover, an oxide shell can offer extra stabilization preventing the NPs aggregation or synthetisation when exposed to harsh conditions. Metallic NPs can be integrated in an oxide matrix in different ways such as: core–shell [72] or yolk-shell [73] structures, referring to a single noble metal core surrounded by a metal oxide shell or a single movable noble metal core inside a hollow metal oxide shell, respectively, but also multiple noble metal cores [74] coated with a metal oxide shell or sandwich structures [75] between multiple metal NPs and a oxide layer, or multiple noble metal NPs embedded [76] within metal oxide matrices.

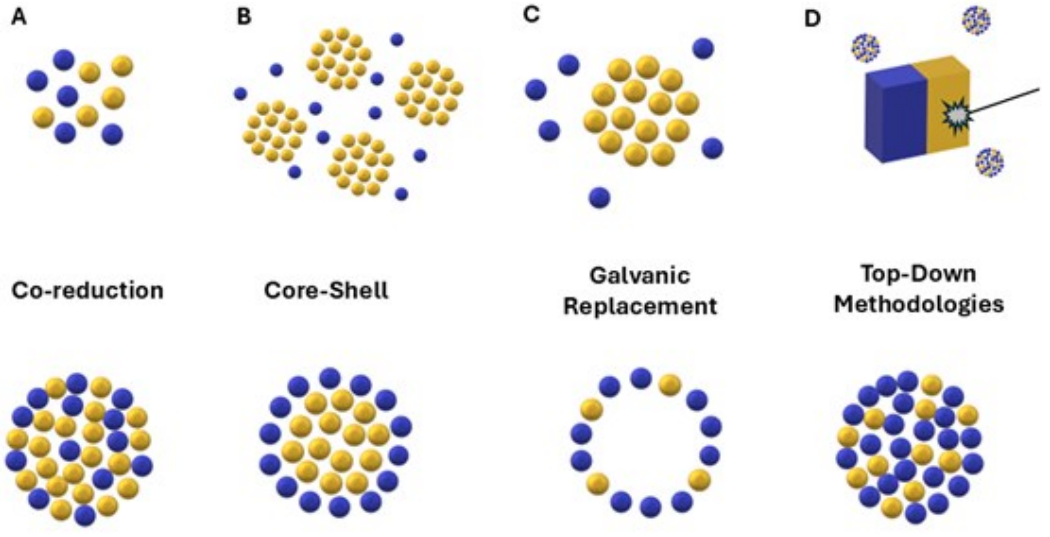


**Figure 9.** Schematic illustration of common synthetic strategies for bimetallic NPs. (A)Co-reduction: simultaneous reduction of two metal precursors yields alloyed NPs with a mixed atomic distribution. (B)Core–shell growth: sequential nucleation produces NPs where one metal forms the core and the second metal forms the shell. (C) Galvanic replacement: a sacrificial template undergoes partial dissolution, leading to hollow or porous bimetallic structures. (D)Top-down methodologies: bulk alloys are fragmented through processes such as laser ablation, sputtering, or ball milling.

Some of the first reports of these types of materials concerns the growth of Au-labeled $SiO_2$ particles [77] and a homogeneous $SiO_2$ shell on Au NPs [78]. These studies were motivated by the necessity of stabilizing the particles without hindering their properties and for this purpose $SiO_2$ has been proved to be an ideal candidate due to its inertness and transparency. Due to the scarce affinity of Au for $SiO_2$ (vitreophobic character), caused by the absence of the formation a superficial passivating oxide film in solution and to the presence of organic anions, the NPs had to undergo a functionalization step using aminopropyltrimethoxysilane (APTMS) to prime the surface for the following $SiO_2$ growth, making it vitreophilic. The $SiO_2$ growth was then promoted on the NPs acting as nucleation sites, applying the Stöber method via hydrolysis and condensation of tetraethylorthosilicate (TEOS, $Si(OC_2H_5)_4$) in an alcohol/water mixture [79]. This method had been also applied to the coating of Ag NPs [80] and the first test of this composite system in the catalysis of a redox reaction [81]. Moreover, both $Au@SiO_2$ and $Ag@SiO_2$ have been subjected to harsh condition to demonstrate core corrosion. This consequently demonstrates that the $SiO_2$ layer has an inherently porous character that allows for diffusion of metal ions and/or reagents through the pores [82]. These experiments demonstrated that the $SiO_2$ layer will not hinder the properties of the metallic core, thus paving the way for a series of applications of these nanocomposites. Further methodologies have been explored to prevent the dissolution of more sensitive cores, such as Ag, and to stabilize NPs before the $SiO_2$ coating synthesis such as the use of PVP [83], polyethylene glycol (PEG) [84], layer-by-layer (LbL) polyelectrolyte wrapping [85], use of surfactants [86], glucose [87]. To obtain composite nanomaterials with a greater variety of properties and possible applications is it also possible to synthesise a mesoporous silica coating. This type of material is characterized by the presence of ordered pores in between 2 nm and 50 nm in diameter. The first example of a tunable mesoporous silica structure (called MCM-41) (**Figure 10**) was obtained with the use of surfactants. These surfactants form micelles in the synthesis solution and the micelles form templates that create the mesoporous framework around which the silica precursor will condense to form the final structure. The template was then removed by calcination. For the MCM-41 synthesis the most used surfactant was CTAB [88]. Spherical Au NPs are among the first examples of metallic NPs individually coated with a mesoporous $SiO_2$ layer [89,90]. In the first reports, the NPs were subjected to the vitreophilization process [78], previously reported for amorphous $SiO_2$ coatings, and also were coated with a thin layer of dense $SiO_2$ before the mesoporous coating synthesis. A more direct approach for the mesoporous shell synthesis has been demonstrated on Au nanorods [91], in this process CTAB was used a both NPs stabilizer and $SiO_2$ template, without the necessity of the intermediate vitreophilization step. Similarly, the precise control over the shell thickness was achieved by regulating the TEOS amount and addition rates and/or by stopping $SiO_2$ condensation with PEG-silane at the desired thickness [92]. Since then, different metals and their respective oxides have been encapsulated in a variety of mesoporous $SiO_2$ shells architectures leading to the application of these composite nanomaterials in a variety of fields (biomedicine, catalysis, sensing, gas storage) [93,94].

### 2.7. Biogenic synthesis of NPs

Biogenic synthesis of NPs, frequently referred to as "green synthesis," consists of group of methodologies for the synthesis of NPs with the use of naturally sourced molecules and organisms [95,96]. These methodologies can be categorized into two main groups:

- *Plant-mediated:* this group of syntheses includes intracellular and extracellular (plant extracts or extracted phytochemicals) processes. Some plants have the capability of accumulating metals and produce NPs thanks to the variety of molecules present in their structure. While various methodologies exist, the predominant approach involves the utilization of plant extracts. The extracts serve dual roles as reducers and potential stabilizers or capping agents. They are added to the solution containing the metal precursor and, thus, most methodologies are classifiable as "direct syntheses".
- *Microbial synthesis:* several microorganisms such as bacteria, fungi, algae, yeasts and viruses are also reported to synthesize metallic NPs. Depending on the type of microorganism the synthesis can happen intracellularly or extracellularly. The extracellular synthesis method is favoured for its straightforward and simpler purification steps. Conversely, the intracellular synthesis presents challenges and higher costs due to the necessity of additional separation and purification steps. The formation of NPs during the microbial synthesis process occurs through the oxidation/reduction of metallic ions by biomolecules secreted by microbial cells (enzymes, sugars, carbohydrates, proteins). Nonetheless, the microbial synthesis pathways are not yet completely understood due to the variation among the different microorganisms.

Biogenic synthesis of NPs offers clear advantages: it is eco-friendly and produces biocompatible NPs. Some of the synthesised NPs might retain biological activity deriving from the source material and can subsequently be applied in areas such as antimicrobial coatings, agricultural products, and environmental remediation [97,98].

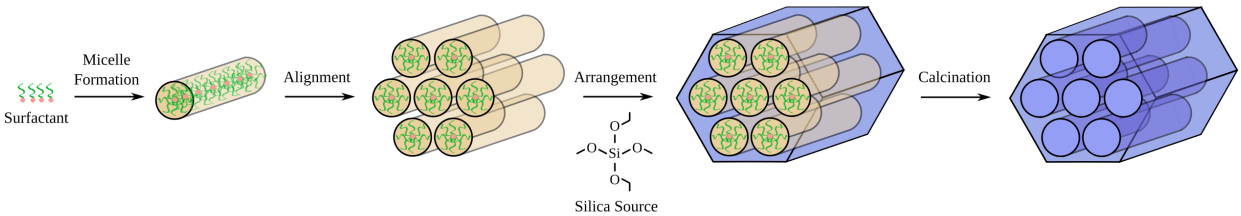


**Figure 10.** Synthesis pathway of MCM-41. Reproduced from Hermann Luyken - Own work, CC0, wikimedia.org/w/index.php?curid=32258196.

On the other hand, these protocols might also present significant drawbacks. When using plants extracts, the availability of the plants, fruits, and flowers and the composition of their extracts might depend on seasonality, geography and growth conditions, which in turn affects reproducibility, scalability, and NPs purity [97]. The plants or their extract might also have to be preserved before their use, and this increases the energy cost of the process [99]. Similarly, microorganisms might have to be grown for the purpose of synthesis, adding a costly step, in terms of time and energy, to the process. Oftentimes, the NPs obtained with biogenic synthesis lack in monodispersity (size and shape) and stability making their application and scalability more challenging [100,101]. Nevertheless, advances in synthetic protocols continue to improve the morphology and monodispersity of biogenically produced NPs [102].

## 3. Optical Properties of Metallic NPs

'Metals' optical properties are governed by conduction electrons that move freely on the metal. An electromagnetic source can influence and drive the movement of these electrons. The electromagnetic source can induce an oscillation that resonates with the shape of the metal surface and in this case a surface plasmon resonance is generated [69,103,104].

At the macroscopic level, when an electromagnetic wave interacts with the metal, the electric field of the wave can cause the collective oscillation of the electrons, this phenomenon is known as surface plasmon. The Drude's model describes the frequency at which this collective oscillation occurs as the bulk plasma oscillation frequency ($\omega_p$) (Equation 6).

$$\omega_p = \sqrt{\frac{N_h e^2}{\epsilon_0 m_h}} \qquad (6)$$

Where $N_h$ represents the mobile electrons (holes) density, $e$ is the charge of the electron, $m_h$ is the electron (hole) effective mass $\epsilon_0$ is the dielectric permittivity of vacuum.

When metals are in nanometres range, such as in NPs with a size comparable to a wavelength, and all the NPs are illuminated with the appropriate wavelength to produce resonance, then a LSPR is produced. LSPR in NPs depends on several factors, such as the metal type, the size and shape of the NP, and the surrounding media. Every metal has a complex dielectric function ($\epsilon_m$) that depends on the wavelength λ according to the Equation 7:

$$\epsilon_m(\lambda) = \epsilon_{real}(\lambda) + \epsilon_{im}(\lambda) \qquad (7)$$

The real part of the dielectric function determines the frequency at which electron oscillation resonance occurs, while the imaginary part incorporates the broadening and absorptive dissipation of this resonance due to damping and dephasing of the electron oscillations. In this context, the dielectric constants for NPs at different wavelengths are assumed to match those of bulk metals. For most metals, excluding some noble and alkali ones, $\epsilon_{im}$ is typically very large, which suppresses the excitation of surface plasmons in the visible region. Meanwhile, $\epsilon_{real}$, which correlates with the ability to absorb light, is negative for alkali and noble metals. In non-noble metals, interband transitions contribute positively to $\epsilon_{real}$, hindering the excitation of surface plasmon modes in small metal spheres. For example, both Au and Ag NPs exhibit intense LSPR, but the Ag LSPR exhibits markedly greater intensity compared to Au. This difference can be attributed to the disparities in their $\epsilon_{im}$. Ag possesses a notably smaller $\epsilon_{im}$, consequently experiencing lower dissipative losses than Au. This translates to a higher scattering quantum yield for Ag NPs, indicating a greater proportion of incident light being scattered as opposed to absorbed.

Furthermore, the narrower bandwidth and sharper LSPR peak observed in Ag NPs can be ascribed to the combination of a smaller $\epsilon_{im}$ and a steeper slope (reflecting a greater magnitude) of the real component of the dielectric function $\epsilon_{real}$. This leads to a more restricted range of resonant frequencies, resulting in a sharper peak in the LSPR spectrum. Consequently, Ag NPs surpass Au in terms of their light-scattering efficiency within the vis-NIR region [105].

The size of the NPs affects their optical and electronic properties due to the quantum confinement of the conduction electrons, thus absorption wavelength is directly proportional to the radius of NPs, so as the NP size decreases the LSPR wavelength also decreases (Equation 8):

$$\gamma = \gamma_\infty + \frac{A v_f}{R} \qquad (8)$$

where $\gamma_\infty$ is the scattering rate of the free electrons in bulk metal, $A$ is a constant, $v_f$ is the Fermi velocity of the electrons, and $R$ is the radius of the NPs. The shape of the NPs can change the surface polarization, and therefore LSPR at desired wavelengths can be achieved by synthesising NPs with different morphologies. The relationship between the LSPR shift and shape of particles can be established as in Equation 9:

$$\Delta\lambda = \frac{\Delta N}{2N}\lambda_{sp}\sqrt{\epsilon_\infty + \left(\frac{1-\eta}{\eta}\right)\epsilon_{medium}} \qquad (9)$$

Where $N$ is the electron density in the metals, $\lambda_{sp}$ is the SPR wavelength for metals, $\epsilon_\infty$ is the high-frequency contribution to the metal dielectric function, $\epsilon_{medium}$ is the dielectric constant of the medium, and $\eta$ is the particle shape factor.

In addition to the dipolar mode (**Figure 11**), which is the most commonly observed and studied mode, higher-order modes such as the quadrupole and octupole LSPR can also occur in plasmonic NPs. These higher-order modes involve more complex charge distributions within the NP, resulting in resonances at higher energies compared to the dipolar mode. The quadrupole LSPR involves the collective oscillation of electrons along two perpendicular axes, leading to a quadrupolar charge distribution within the nanoparticle. Similarly, the octupole LSPR involves the collective oscillation of electrons along three perpendicular axes, resulting in an octupolar charge distribution. Because of the more complex charge distributions involved in higher-order modes, their energies typically increase with increasing multipole order. This means that quadrupole LSPR occurs at higher energies than dipole LSPR, and octupole LSPR occurs at even higher energies than quadrupole LSPR (**Figure 12**) [106]. Moreover, LSPR is sensitive to the surrounding medium and its absorption wavelength maximum

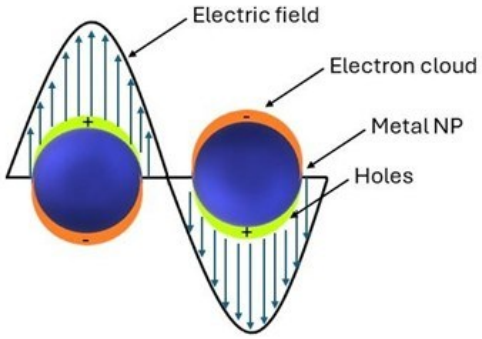


**Figure 11.** Illustration of the dipolar surface plasmon resonance, with the collective oscillation of the conduction band electrons due to an incident electric field.

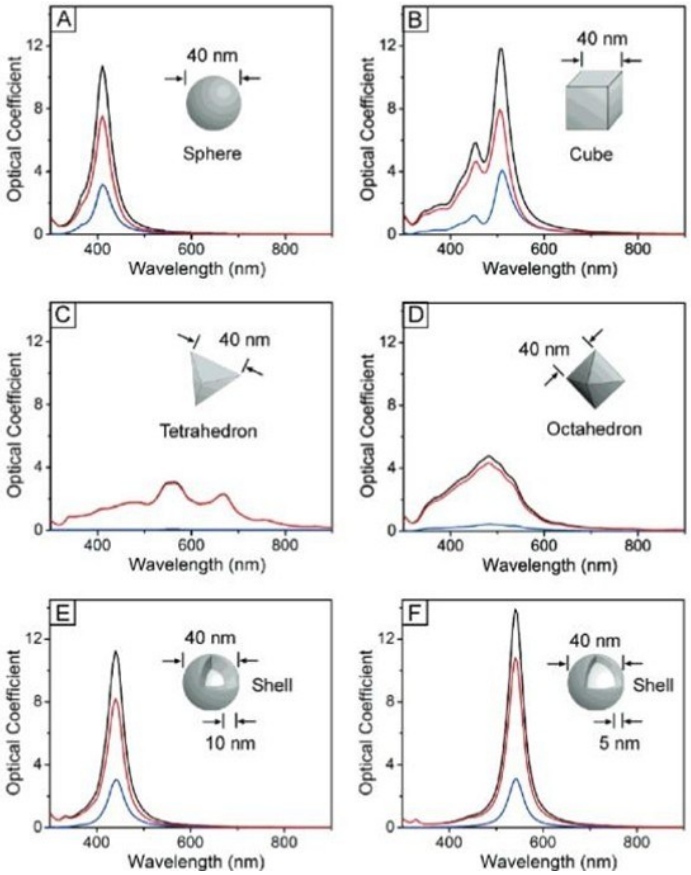


**Figure 12.** Calculated UV-vis extinction (black), absorption (red), and scattering. (blue) spectra of Ag nanostructures, illustrating the effect of a nanostructure's shape on its spectral characteristics. An isotropic sphere (A) exhibit spectra with a single resonance peak. Anisotropic cubes (B), tetrahedra (C), and octahedra (D) exhibit spectra with multiple, red-shifted resonance peaks. The resonance frequency of a sphere red-shifts if it is made hollow (E), with further red-shift for thinner shell walls (F). Reproduced with permission from reference [106] Copyright 2006 American Chemical Society.

$\lambda_{max}$ changes as the dielectric constant $\epsilon$ or refractive index $n$ of the medium is changed. The LSPR frequency can then also be shifted by varying the environment (stabilizer, functionalization or solvent molecules) and as a consequence the dielectric constant of the NPs-environment system. The field induced by the conjunct of NPs and their medium can be written in the form of effective polarizability and dipole moment as given by Equation 10:

$$\rho = \epsilon_m \alpha E_0 \qquad (10)$$

Where $\rho$ is the effective dipole moment of the NP-medium system, $E_0$ is the incident electric field, α is the dipolar polarizability and $\epsilon_m$ is the dielectric constant of embedding media. When the NPs are coated with a dielectric material of thickness $d$ and dielectric constant $\epsilon_d$, then polarizability α is defined by Equation 11:

$$\alpha = 4\pi\epsilon_0(R+d)^3 \frac{\epsilon_d\epsilon_a - \epsilon_a\epsilon_b}{\epsilon_d\epsilon_a + 2\epsilon_m\epsilon_b} \qquad (11)$$

Where α is the NP's radius and $\epsilon_\alpha$ is the dielectric constant of the NP. Similarly, $b$ is the total radius of the NP-medium system and $\epsilon_b$ is the dielectric constant of the NP-medium system. A red-shift in

absorption spectra is observed with the increase in the dielectric constant of the environment. The magnitude of the spectral shift Δ⊠ for NPs is described in Equation 12:

$$\Delta\lambda_{max} = m\Delta n\left(1 - e^{\frac{-2d}{l_d}}\right) \qquad (12)$$

Where $m$ is the bulk refractive-index response of the NPs, $\Delta n$ is the change in the refractive index induced by the adsorbate, $d$ is the effective adsorbate layer thickness, and $\ell d$ is the characteristic electromagnetic field decay length. Thus, shell materials with a higher refractive index will lead to a larger red-shift with broadening of LSPR peaks.

## 4. Application of Metallic NPs

Metallic NPs, thanks to the huge variety of structures and composition, play a crucial role in various fields, from electronics to healthcare to agriculture and environmental remediation [93,107]. Some of these applications, where plasmonic and composite NPs are applied, are discussed below.

### 4.1. Healthcare

The healthcare sector includes a diverse array of needs and applications. A few applications where NPs have an impact are presented below.

4.1.1. *Antibacterial activity and Antibiotic resistance*

In recent years, significant efforts have been directed towards addressing the ever increasing problem of antibiotic resistance [108], whether by seeking alternatives or enhancing the efficacy of existing antibiotics through the integration of nanomaterials. Additionally, great efforts have been devoted to exploring methods to prevent bacterial proliferation on surfaces and biofilm formation. Ag NPs are undoubtedly the most extensively studied NPs for mitigating antibiotic resistance as their antibacterial properties have been known for centuries [109]. However, more recently also Cu and ZnO NPs have been investigated for their intrinsic antibacterial activity [110,111]. Ag and ZnO NPs have demonstrated synergistic effect with several antibiotics against a variety of bacteria through diverse modes of action, such as metal ions release, non-oxidative and oxidative stress [112–114]. Additionally, Ag, Cu, and ZnO NPs have shown the ability to synergize with conventional antibiotics and disrupt bacterial efflux pumps, a key mechanism involved in biofilm formation [115]. Research has concluded that Ag NPs can enhance the efficacy of antibiotics against pathogens commonly encountered in veterinary medicine, regardless of antibiotic resistance [116]. NPs with antibacterial properties can be also integrated in devices. Ag, Au, Cu, ZnO and $TiO_2$ have demonstrated to be able to increase the antibacterial properties of chitosan when applied as wound dressing to avoid bacterial contamination and infections, and also by enhancing healing through the regulation of re-epithelialisation and inflammation [117]. Moreover, medical implants, catheters, and healthcare fabrics can be integrated with metallic antibacterial NPs to mitigate infection risks and bacterial transmission in healthcare setting [118]. Tri-elemental AgCuMg NPs, despite being in the early stages of development, have demonstrated antibacterial activity against both gram-positive and gram negative bacteria when integrated into coatings [119]. Similarly, hydrogel coatings loaded with Cu NPs have exhibited pronounced antibacterial properties and adhered well to stainless steel medical equipment [120]. Recent research has emphasised the significance of surface topographies in conferring antibacterial properties. Different morphologies found in nature are being studied for their potential to further enhance antibacterial surfaces. The combination of antibacterial surface topographies and antibacterial NPs holds promise in reducing infections and controlling their spread [121,122]. The primary drawbacks of using NPs for their antibacterial properties might be a limited stability on the NPs and an excessively fast ions release from the particle. Composite NPs, such as Ag@mesoporous $SiO_2$ NPs, have the potential to overcome these disadvantages and confer superior properties compared to bare NPs. Thanks to the accessible and porous network of the protective $SiO_2$ layer, the encapsulated nanocrystals can release antibacterial Ag ions in a steadier and continuous manner [123], furthermore the $SiO_2$ shell can help to prevent aggregation and increase the NPs solubility. The mesoporous channels can then be additionally used for encapsulation of active molecules, such as antibiotics, to treat antibiotic resistant infections [124] or to accelerate the healing of infected wounds [125].

*4.1.2. Imaging, diagnosis and cancer treatment*

Plasmonic NPs, due to their unique optical properties, find applications in diagnostics, particularly for biomedical imaging of tissues and for the detection of cancer cells. The composition and the shape of the NPs are adjustable, thus making it possible to tune the NPs based on the desired scattering [126]. For instance, NPs that scatter light in the near-infrared (NIR) range allow for a high-resolution deep tissue bioimaging [127]. Furthermore, NPs can be functionalized with antibodies, aptamers, or peptides to confer specific cellular binding features, thereby enhancing imaging precision and detection sensitivity. The functionalized NPs can be assembled to obtain a "detection kit" for a series of different diseases [128,129]. Coating NPs with a mesoporous $SiO_2$ shell can increase the biocompatibility and the cell up-take of the nanomaterial making them suitable for potential in vivo imaging applications. For example, biomolecule - conjugated Au nanorods encapsulated in a mesoporous $SiO_2$ shell were specifically taken up by cancer cells *in vitro* [130]. Mesoporous $SiO_2$ can also be modified with functional groups and conjugated with biomolecules for specific labelling of cells. Photoacoustic imaging, an emerging technique in biomedical imaging, can be significantly enhanced through the use of plasmonic NPs as contrast agents. In this imaging modality, a short laser pulse is directed onto the tissue under examination, causing rapid thermal expansion and the generation of ultrasound waves. These waves are then captured by ultrasound transducers and translated into high-resolution images. Au NPs are favoured in this application due to their biocompatibility, ease of functionalization, and adjustable LSPR. Current research efforts are concentrated on optimizing NPs for photoacoustic imaging within the second NIR window (1000 - 1700 nm). This spectral range

offers reduced background noise and scattering in biological tissues, thereby facilitating clearer and more precise imaging [131].

Other than diagnosis, plasmonic NPs can also find application in therapy. When plasmonic NPs are irradiated at their resonance wavelength they will generate a temperature rise in their proximity. This effect has found application in photothermal therapy, that is a non invasive technique utilized for cancer treatment. Plasmonic NPs, and particularly Au NPs are excellent candidates for this therapy due to the easy cell take-up, easy functionalization for specific cells targeting, and easy LSPR tuning. For photothermal therapy, the 650 - 900 nm range is preferred for application because minimal skin and tissue absorption allows light to penetrate deep into tissues in a non-invasive manner. The generated heat can induce thermal damage to cancer cells, leading to their destruction and vascular disruption that consist in damaging the tumour's blood vessels, compromising the tumour's viability [132,133]. Composite NPs can also add extra functionalities to the photherapic treatment such as the delivery of a drug encapsulated in a mesoporous structure [134,135] or in a hollow plasmonic structure [136]. The generated heat can act as a trigger for the release of an encapsulated drug, while profiting of the augmented cell membrane permeability due to higher temperature [93,137]. Additional functionalities, such as magnetic properties, can enhance the NPs targeting of cancer cells through magnetic-guided photothermal therapy [138].

### 4.2. Sensing

#### *4.2.1. Plasmonic sensing*

NPs are particularly sensitive to their surrounding environment and this property made them to find application as plasmonic sensors for ex-situ analysis. Plasmonic sensors can detect subtle changes reflected in modifications of the LSPR of the colloidal system. Due to their outstanding optical properties, Au and Ag NPs are mostly used for this type of sensing. Analytes can be detected ia a *yes/no* fashion or also quantified as a consequence of different phenomena [139]:

- *Analyte detection based on aggregation of NPs:* the addition of analytes to the colloidal system can cause a decrease the inter-particle distance of the NPs leading to their aggregation and to a change in shape and position of the LSPR. The amount of analyte can be estimated with spectroscopic or colorimetric techniques [140,141].
- *Analyte detection based on oxidation of NPs:* in the presence of analyte NPs can undergo oxidation, thus the number of metallic NPs in solution will decrease leading to a change in the colour of the solution and of the LSPR intensity. The analyte quantity can then be estimated observing the changes at a specific wavelength [142].
- *Analyte detection based on dimensional change of NPs:* certain analytes can cause a change the morphology/dimension of the NPs. In this case, a change in the LSPR profile will be observed, some bands will be quenched while others might appear [143].

Plasmonic NPs applied in sensing might undergo extra functionalization with different molecules such as oligonucleotides, proteins and amino acids, organic polymers, and organic compounds. Functionalized plasmonic NPs can provide specificity towards target analytes, allowing for higher selectivity and sensitivity in the detection process. Functionalization can enhance the stability and dispersibility of the NPs and further regulate the detection mechanisms [144].

#### *4.2.2. Surface-Enhanced Raman Spectroscopy*

Raman scattering is inherently a weak phenomenon up to ten orders of magnitude weaker than fluorescence [145], but it offers high specificity. The combination of Raman's specificity with the plasmonic field enhancement provided by plasmonic nanostructures, known as Surface-Enhanced Raman Spectroscopy (SERS), first observed in 1973 for pyridine adsorbed on a roughened silver electrode [146], can exponentially increase the intensity of Raman signals, enabling the detection of even single molecules of analyte [107,147,148]. Molecules adsorb onto the surface of metallic nanostructures, and when laser light is directed onto the substrates, it interacts with the LSPR of the NPs, resulting in a significant enhancement of the Raman scattering signal. SERS can be performed either in a colloidal solution or, more commonly, with the solution containing the analyte deposited on a surface previously functionalized with metallic NPs. The shape, size, and arrangement of the NPs greatly influence the enhancement of the Raman signal. Au and Ag NPs, both in pure and alloyed compositions, are the most commonly used. A greater field enhancement occurs when NPs exhibit tips, cavities, and overall anisotropic morphology [145]. Additionally, the disposition and inter-particle distances of the NPs determine the effectiveness of a SERS substrate [147], in this case $SiO_2$ shells can be employed to further regulate the arrangement and distances between NPs. Mesoporous $SiO_2$ is generally preferred, as its channels permit the diffusion of analyte molecules to come into proximity with the metallic surface. Moreover, the shell can serve a protective function, increasing the stability of the NPs and preventing possible aggregations and reshaping phenomena [93].

#### *4.2.3. Surface-Enhanced Fluorescence*

The phenomenon of fluorescence is widely used in sensing, thanks to its fastness, reliability and high sensitivity. However, the major limitation is constituted by the quantum yield and fluorescence lifetime of the fluorophore [149]. Similarly to SERS, plasmonic near -field enhancement can enhance the light emission by fluorophores located in close vicinity of metallic nanostructures, in a phenomenon known as Surface-Enhanced Fluorescence (SEF). A crucial parameter for SEF is the distance between the NPs and the analyte molecules. Fluorophores can not, in fact, be in contact with the metallic surface, otherwise their emission will be quenched, while a distance of a few nm will dramatically increase it. As spacers, either thin metal oxide layer or $SiO_2$ layers can be used, the latter being more flexible regarding the possibility of synthesising shells with different thicknesses. $SiO_2$ shells can be also further functionalized to increase the detection of specific analytes [93]. Alloyed NPs with tunable composition and $SiO_2$ shells with multiple functionalisation's, combining the scattering of NPs and the SEF effect, can provide a platform for multiplex-detection allowing for the detection of numerous targets within the same

sample, thus providing a comprehensive view of the system [107,150].

### 4.3. Catalysis

Catalytic processes have brought significant advancements in research and technology, enabling the production of fertilizers, plastics, chemicals, and environmental remediation, such as the catalytic removal of pollutants from car exhausts.

*4.3.1. Metallic NPs in catalysis*

Metallic NPs have shown potential in the field of catalysis, as their properties are different from the one of their bulk counterparts and the reduction of the size brings an increment in the high surface to volume ratio, and thus active sites for the catalysis to happen. The composition, size and shape of the NPs are of great importance in the determination of the catalytic properties of the nanocrystals. For example, Au bulk surfaces are known to be inert, but in 1987 it was discovered that Au NPs were effective for low temperature CO oxidation [151,152]. Decreasing the size of the NPs can lead to an increase in the number of corner atoms and edges, that will lead to a higher degree of surface unsaturation. This variation can impact the bond strength of reaction intermediates with the catalyst, while corners and edges also offer diverse surface configurations for molecules to adsorb [153–155]. An increase in edges and corners is also obtainable with the synthesis of anisotropic NPs. Shape, that means which crystal facets are exposed to the reagents, has a significant importance on the catalytic properties of the NPs. Specifically, NPs that present tips and edges, considered active sites for the catalytic reaction, usually display better properties. When NPs have a quasi-spherical shape and exhibit only (111) low energy facets, their catalytic efficiency is usually lower compared to NPs of the same metal but with different morphologies that expose higher energy (100) facets [156]. Furthermore, shape can also determine the selectivity of a reaction, for example in the benzene hydrogenation over cubic and cuboctahedral Pt NPs. Cuboctahedral NPs, characterized by the presence of (111) facets, lead to the formation of cyclohexane and cyclohexene, while cubic NPs, characterized by the presence of (100) facets, only lead to the formation of cyclohexane [152,157].

*4.3.2. Composite NPs in catalysis*

Composite NPs can have a prominent role in catalysis thanks to the great variety of combinations of structures and materials. Metallic NPs, for instance, can be encapsulated within various materials and with different architectures such as core@shell and yolk@shell configurations, and supported by diverse substrates including MOFs, carbon, and dendrimers (**Figure 13**) [158]. The encapsulation of single catalytic NPs in a core@shell structure can offer several advantages, such as adding extra stabilization and protection and prolonging the life of the catalyser. Multicore core@shell NPs or non coated NPs can in fact face aggregation of the cores both in colloidal solution or during high temperature catalytic processes. An aggregation will inevitably bring to a loss of catalytic sites and consequently a decrease in the catalytic efficiency [159]. The yolk@shell architecture, often referred to as nanoreactor in the catalysis field, offers additional advantages compared to the core@shell structure. As the core is able to freely move inside the protective shell, there is more surface area, and thus more catalytic sites available [160]. Encapsulated structures can furthermore manifest a greater selectivity. The pores' size, either in nanoreactors or supports architectures [161], can be finely tuned to act as a molecular sieve and regulate molecular diffusion [158]. Extra functionalities can also be added to the surface of metallic NPs to improve the catalytic reaction rates [162].

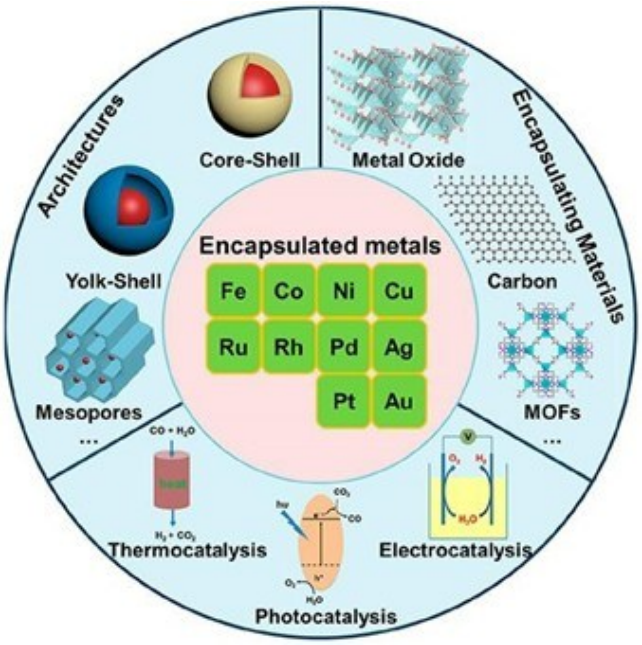


**Figure 13.** Encapsulated metal NPs with different architectures for catalytic applications. Reproduced with permission from reference [158] Copyright 2020 American Chemical Society.

Composite bimetallic NPs have emerged as a promising class of catalysts, offering unique properties and enhanced catalytic performance compared to their monometallic counterparts. By combining two different metals within the same NP, bimetallic NPs can exhibit synergistic effects, where the properties of the individual metals are combined and amplified, leading to improved catalytic activity and selectivity [163]. Bimetallic NPs can exhibit features on their surface such as migration, segregation, isolation of single atoms, surface enrichment, leading to the formation of structures with enhanced catalytic activity [164]. Pd based PdZn and PdPt bimetallic NPs, due to an increase of defects in the NPs structure and a change the electronic properties of the catalyst (ligand effect), demonstrated superior properties when compared to the Pd monometallic counterpart in the selective hydrogenation of dehydrolinalool [165]. PtAu NPs showed excellent properties in the reduction of 4-nitrophenol. The authors believe that the alloying of Pt and Au induces a strong synergistic effect that increase the catalytic activity, compared to pure Pt and pure Au NPs, by altering the electronic structure and the preferential adsoprtion of oxygen [166]. Ni@Pt NPs exhibited more than twice the catalytic activity of Pt NPs synthesized using the same method. ORR experiments demonstrated a significant enhancement in the activity of Ni@Pt catalysts compared to Pt alone. This increase in catalytic activity is attributed to alterations in geometric and/or electronic properties, which can influence the binding energy of oxygen and the adsorption of bisulfate anions [167].

*4.3.3. Photocatalytic applications*

Plasmonic metal NPs, either monometallic or bimetallic, due to their peculiar optical properties can be successfully employed in photocatalytic processes. The photocatalysts employed for a diverse range of chemical reactions under UV-visible light, are predominantly semiconductors. In such systems, semiconductors absorb photons, generating high-energy charge carriers (electron–hole pairs) within the semiconductor material. These charge carriers then dissociate and migrate to catalytically active sites situated at the semiconductor/liquid interface, where they facilitate various chemical transformations [168]. The most frequently utilized semiconductor is $TiO_2$. Because of its large band gap (3.0 - 3.2 eV), $TiO_2$ primarily absorbs light in the near UV region (<400 nm), which constitutes only a small portion of solar radiation (approximately 5%) [169]. Plasmonic NPs and semiconductors have emerged as a feasible combination to harvest a higher range of the solar spectrum. When deposited on $TiO_2$, a Schottky barrier will form at the interface between NPs and $TiO_2$, thus facilitating the electron-hole pairs separation and consequently enhancing the lacking photocatalytic activity of semiconductor materials under visible light [170].

AgAu NPs on $TiO_2$ have been used to degrade phenol in aqueous solution under visible light with more efficiency than Au NPs on $TiO_2$ [171]. The authors propose that the enhanced activity is attributed to electron transfer mechanisms. The presence of bimetallic NPs impedes charge recombination on Au NPs by facilitating electron transfer to Ag, known for its electron accepting abilities, and subsequently to the $TiO_2$ conduction band, facilitating the oxidation of phenol molecules by $O_2$– to form benzoquinone on the AgAu surface, while keeping it in a reduced state. AuPd NPs on $TiO_2$ were used to demonstrate that the relative composition and the structure of the bimetallic NPs have influence on the photochemical $H_2$ evolution from ethanol aqueous solution. Core@shell Au@Pd bimetallic NPs showed the highest activity and NPs with a higher Pd content showed enhanced photoactivity, attributed to the fact that a thicker Pd shell supposedly shields photogenerated electrons from the recombination with holes [172].

Monometallic NPs deposited on $TiO_2$ were also utilized in water splitting and $H_2$ generation. Au NPs have successfully produced $H_2$ generation under visible light illumination, several experiments demonstrated the importance of different parameter such as the phase of the $TiO_2$ [173], and the size of the Au NPs [174]. Other than Au NPs, also monometallic Ag NPs [175] and Cu NPs [176] have been used for the same catalytic reaction. Cu NPs constitute a valid alternative to the rarer and more valuable Au and Ag.

Photocatalysis mediated by plasmonic NPs has proven an excellent tool in the field of environmental remediation. Several studies highlighted the potential degradation of pollutants either by NPs in solution or supported on $TiO_2$. Molecules such as methylene blue, rhodamine B, phenol are often chose as model for pollutants. Bio-synthesised CuO NPs [177], Ag NPs [178], degraded methylene blue and crystal violet in solution under sunlight. Supported NPs offer easier handling, recovery and the combination effect of the semiconductor support. Ag and Au NPs on mesoporous $TiO_2$ were tested for the degradation, as water pollutant models, of the azo dyes (congo red, methyl orange, acid orange 10, and remazol red) under solar and visible light irradiations. Both NPs improved the performance of $TiO_2$ with the Au NPs appearing to be the most promising candidates [179]. Photocatalysis can also be applied in the degradation of a class of rapidly emerging indoor pollutants known as volatile organic compounds (VOCs), of which examples are formaldehyde, acetaldehyde, methanol, ethylene, toluene.

Au supported on $TiO_2$ can degrade formaldehyde in air and under visible light. For the oxidation to happen the moisture present in the air has a decisive effect and visible light seems to accelerate the rate-determining steps of the reaction, leading to an overall possible degradation process for this VOC in ambient conditions [180]. Au@$TiO_2$ core@shell and yolk@shell structures demonstrated photocatalytic activity for the oxidation of gaseous toluene under visible light illumination. The yolk@shell architecture, with greater surface area and numerous mesoporous channels that can enhance the absorption of VOCs and provide more active sites, proved to have the best activity and reusability [181]. Photocatalysis offers a potential solution to the energy crisis and rising $CO_2$ emissions caused by human activities. $CO_2$ is a highly stable molecule and conventional thermolysis methods used for $CO_2$ degradation require harsh conditions and thus high energy consumption [169]. $CO_2$ photocatalytic conversion aided by plasmonic NPs is a hugely studied process and promising result have already been reported in the obtention of valuable products such as $CH_4$, $CH_3OH$, and $C_2H_5OH$. NPs of different compositions supported on different $TiO_2$ structures have been tested for $CO_2$ reduction. Au NPs and Pt NPs on $TiO_2$ nanofibers surpassed the catalytic properties of the semiconductor alone thanks to the synergistic effect of the two types of metals, Au LSPR effect that improves charge separation in

the semiconductor and Pt NPs which serve as electron-sink and active site. Ag NPs loaded on $TiO_2$ nanotube arrays promote a more efficient $CO_2$ reduction thanks to the LSPRS properties of Ag. When exposed to light hot electrons will be generated on the Ag NPs which are subsequently injected into the conduction band of $TiO_2$, promoting efficient charge separation and hindering electron -hole recombination. Furthermore, the localized near-field effect induced by the Ag NPs accelerates the transport of electrons within the nanotubes, leading to improved charge carrier transport efficiency [182]. Highly crystalline Cu NPs deposited onto anatase $TiO_2$ were found to convert $CO_2$ into CO while suppressing the competitive mechanism of hydrogen evolution. This study also highlighted the importance of the careful consideration of the most beneficial amount of NPs, as an excessive quantity of Cu demonstrated to be undesirable for the reaction [183].

### 4.4. Energy

The transition from fossil to alternative fuels is crucial for a sustainable and healthy future for our planet. Plasmonic NPs have gained attention as a possible solution to increase the exploitation of solar energy [184]. Plasmonic NPs, thanks to their absorption and scattering properties, can be efficiently integrated in solar light harvesting devices to maximize their harvesting capability [93].
Au NPs, with a size of approximately 45 nm, were incorporated into organic photovoltaic solar cells (OPVs) based on polymers. The resulting plasmonic enhanced OPV device exhibited a significant increase in light absorption due to localized field enhancement induced by LSPR, without compromising the device's electrical properties [185]. A further improvement in VOCs performance can be promoted by utilizing NPs protected by a $SiO_2$ shell. Core@shell particles can, in fact, be partially embedded on the active layer interface of the device. The $SiO_2$ shell serves many purposes such as maintaining the desired inter-particle distance and preventing changes in the morphology of the particle [186].
Similarly, NPs can be incorporated in dye-sensitized solar cells (DSSC). These cells utilize the light-absorbing properties of dyes, particularly in the visible range, to sensitize a metal oxide film, usually $TiO_2$. To take advantage of the absorption properties of plasmonic NPs, the use of anisotropic NPs and mixtures of different morphologies has been explored. For example, studies have shown that Au@$Ag_2S$ nanorods [187] and mixtures of Ag NPs [188] can enhance the efficiency of DSSC devices due to their broader light absorption range compared to the commonly used spherical NPs.

## 5. Conclusions

Metallic NPs provide an exceptional platform for exploring the relationship between synthesis, structure, and functionality. As discussed throughout this review, the choice of synthetic strategy, whether top-down, bottom-up, direct, or seed-mediated, determines the resulting morphology, stability, and performance of the material. A solid understanding of the principles governing nucleation, growth, and stabilization is therefore essential to design NPs with properties tailored to specific functions. Beyond their synthesis, the optical, catalytic, and biological behaviours of metallic NPs illustrate how nanoscale features influence macroscopic performance. Their LSPRs enable powerful sensing techniques, while catalytic activity can be precisely adjusted through control of size, shape, and composition. Applications across healthcare, energy, and environmental monitoring demonstrate both their versatility and growing relevance.
By combining historical developments, theoretical insights, and practical considerations, this introductory review seeks to clarify the connections between synthetic methods and resulting properties. The intention is not only to describe the main strategies available but also to encourage critical analysis, creative experimental design, and continued exploration of improved synthetic approaches.

## Acknowledgements

S.N. thanks the FCT/MCTEC (Fundação para a Ciência e Tecnologiaand Ministério da Ciência, Tecnologia e Ensino Superior) Portugal for her doctoral grant associated with the Chemistry PhD program (SFRH/BD/144618/2019). This work was supported by the Associate Laboratory for Green Chemistry LAQV which is financed by national funds from Fundação para a Ciência e Tecnologia and Ministério da Ciência, Tecnologia e Ensino Superior (FCT/MCTES) through the the project UID/50006/2023 of the Associate Laboratory for Green Chemistry - LAQV REQUIMTE, details here: https://laqv.requimte.pt/a/74-funding. PROTEOMASS Scientific Society (Portugal) is also acknowledged by the funding provided through the General Funding Grants 2024 -2025.

## References

[1] J. Ogden, Interdiscip. Sci. Rev. 17 (1992) 261–270. DOI: 10.1179/030801892791925475

[2] S. Medici, M. Peana, V.M. Nurchi, M.A. Zoroddu, J. Med. Chem. 62 (2019) 5923–5943. DOI: 10.1021/acs.jmedchem.8b01439

[3] D.A. Scott, W. Bray, Platin. Met. Rev. 24 (1980) 147–157. DOI: 10.1595/003214080X244147157

[4] M. Radetzki, Resour. Policy 34 (2009) 176–184. DOI: 10.1016/j.resourpol.2009.03.003

[5] J. Pérez-Arantegui, J. Molera, A. Larrea, T. Pradell, M. Vendrell-Saz, I. Borgia, B.G. Brunetti, F. Cariati, P. Fermo, M. Mellini, A. Sgamellotti, C. Viti, J. Am. Ceram. Soc. 84 (2001) 442–46. DOI: 10.1111/j.1151-2916.2001.tb00674.x

[6] F. Antonii, Panacea Aurea, Sive Tractatus Duo de Ipsius Auro Potabili, Ex Bibliopolio Frobeniano, Hamburg, 1618.

[7] J. Kunckel, Nuetliche Observationes Oder Anmerkungen von Auro Und Argento Potabili, Hamburg, 1676.

[8] C. Chan, (2008). DOI: https://www.sciencehistory.org/stories/magazine/from-nanotech-to-nanoscience/

[9] The Stained Glass Association of America, (2025). DOI: https://stainedglass.org/learning-resources/history-stained-glass

[10] I. Freestone, N. Meeks, M. Sax, C. Higgitt, Gold Bull. 40 (2007) 270–277. DOI: 10.1007/BF03215599

[11] R. November, R. February, Philos. Trans. R. Soc. London 147 (1857) 145–181. DOI: 10.1098/rstl.1857.0011

[12] D. Thompson, Gold Bull. 40 (2007) 267–269. DOI: 10.1007/BF03215598

[13] J. Turkevich, P.C. Stevenson, J. Hillier, Discuss. Faraday Soc. 11 (1951) 55. DOI: 10.1039/df9511100055

[14] G. Mie, Ann. Phys. 330 (1908) 377–445. DOI: 10.1002/andp.19083300302

[15] N. Abid, A.M. Khan, S. Shujait, K. Chaudhary, M. Ikram, M. Imran, J. Haider, M. Khan, Q. Khan, M. Maqbool, Adv. Colloid Interface Sci. 300 (2022) 102597. DOI: 10.1016/j.cis.2021.102597

[16] P.G. Jamkhande, N.W. Ghule, A.H. Bamer, M.G. Kalaskar, J. Drug Deliv. Sci. Technol. 53 (2019) 101174. DOI: 10.1016/j.jddst.2019.101174

[17] J. Polte, CrystEngComm 17 (2015) 6809–6830. DOI: 10.1039/C5CE01014D

[18] N.T.K. Thanh, N. Maclean, S. Mahiddine, Chem. Rev. 114 (2014) 7610–7630. DOI: 10.1021/cr400544s

[19] R. Becker, W. Döring, Ann. Phys. 416 (1935) 719–752. DOI: 10.1002/andp.19354160806

[20] V.K. LaMer, R.H. Dinegar, J. Am. Chem. Soc. 72 (1950) 4847–4854. DOI: 10.1021/ja01167a001

[21] W. Ostwald, Zeitschrift Für Phys. Chemie 34U (1900) 495–503. DOI: 10.1515/zpch-1900-3431

[22] J.R. Shimpi, D.S. Sidhaye, B.L. V Prasad, Langmuir 33 (2017) 9491–9507. DOI: 10.1021/acs.langmuir.7b00193

[23] M. José-Yacamán, C. Gutierrez-Wing, M. Miki, D.-Q. Yang, K.N. Piyakis, E. Sacher, J. Phys. Chem. B 109 (2005) 9703–9711. DOI: 10.1021/jp0509459

[24] E.J.H. Lee, C. Ribeiro, E. Longo, E.R. Leite, J. Phys. Chem. B 109 (2005) 20842–20846. DOI: 10.1021/jp0532115

[25] T.L. Moore, L. Rodriguez-Lorenzo, V. Hirsch, S. Balog, D. Urban, C. Jud, B. Rothen-Rutishauser, M. Lattuada, A. Petri-Fink, Chem. Soc. Rev. 44 (2015) 6287–6305. DOI: 10.1039/C4CS00487F

[26] N. Shirtcliffe, U. Nickel, S. Schneider, J. Colloid Interface Sci. 211 (1999) 122–129. DOI: 10.1006/jcis.1998.5980

[27] N.G. Bastús, F. Merkoçi, J. Piella, V. Puntes, Chem. Mater. 26 (2014) 2836–2846. DOI: 10.1021/cm500316k

[28] Y. Ishida, T. Jirasupangkul, T. Yonezawa, New J. Chem. 39 (2015) 4214–4217. DOI: 10.1039/C5NJ00420A

[29] N.R. Jana, L. Gearheart, C.J. Murphy, J. Phys. Chem. B 105 (2001) 4065–4067. DOI: 10.1021/jp0107964

[30] Y. Sun, B. Gates, B. Mayers, Y. Xia, Nano Lett. 2 (2002) 165–168. DOI: 10.1021/nl010093y

[31] N.G. Bastús, J. Comenge, V. Puntes, Langmuir 27 (2011) 11098–11105. DOI: 10.1021/la201938u

[32] Y. Xia, K.D. Gilroy, H. Peng, X. Xia, Angew. Chemie Int. Ed. 56 (2017) 60–95. DOI: 10.1002/anie.201604731

[33] L. Scarabelli, M. Sun, X. Zhuo, S. Yoo, J.E. Millstone, M.R. Jones, L.M. Liz-Marzán, Chem. Rev. 123 (2023) 3493–3542. DOI: 10.1021/acs.chemrev.3c00033

[34] T.-H. Yang, J. Ahn, S. Shi, P. Wang, R. Gao, D. Qin, Chem. Rev. 121 (2021) 796–833. DOI: 10.1021/acs.chemrev.0c00940

[35] A. Guerrero-Martínez, S. Barbosa, I. Pastoriza-Santos, L.M. Liz-Marzán, Curr. Opin. Colloid Interface Sci. 16 (2011) 118–127. DOI: 10.1016/j.cocis.2010.12.007

[36] R. Jin, Y. Cao, C.A. Mirkin, K.L. Kelly, G.C. Schatz, J.G. Zheng, Science (80-. ). 294 (2001) 1901–1903. DOI: 10.1126/science.1066541

[37] S. Chen, D.L. Carroll, Nano Lett. 2 (2002) 1003–1007. DOI: 10.1021/nl025674h

[38] Q. Zhang, Y. Hu, S. Guo, J. Goebl, Y. Yin, Nano Lett. 10 (2010) 5037–5042. DOI: 10.1021/nl1032233

[39] C.H. Zhang, J. Zhu, J.J. Li, J.W. Zhao, ACS Appl. Mater. Interfaces 9 (2017) 17387–17398. DOI: 10.1021/acsami.7b04365

[40] Y. Huang, A.R. Ferhan, Y. Gao, A. Dandapat, D.H. Kim, Nanoscale 6 (2014) 6496–6500. DOI: 10.1039/c4nr00834k

[41] Y. Sun, B.T. Mayers, Y. Xia, Nano Lett. 2 (2002) 481–485. DOI: 10.1021/nl025531v

[42] M.A. Mahmoud, M.A. El-Sayed, Langmuir 28 (2012) 4051–4059. DOI: 10.1021/la203982h

[43] Z. Leng, X. Wu, X. Li, J. Li, N. Qian, L. Ji, D. Yang, H. Zhang, Nanoscale Adv. 4 (2022) 1158–1163. DOI: 10.1039/D1NA00842K

[44] L. Lu, A. Kobayashi, K. Tawa, Y. Ozaki, Chem. Mater. 18 (2006) 4894–4901. DOI: 10.1021/cm0615875

[45] Y.-H. Chen, H.-H. Hung, M.H. Huang, J. Am. Chem. Soc. 131 (2009) 9114–9121. DOI: 10.1021/ja903305d

[46] Mahmoud, C.E. Tabor, M.A. El-Sayed, Y. Ding, Z.L. Wang, J. Am. Chem. Soc. 130 (2008) 4590–4591. DOI: 10.1021/ja710646t

[47] Z. Fang, Y. Zhang, F. Du, X. Zhong, Nano Res. 1 (2008) 249–257. DOI: 10.1007/s12274-008-8029-0

[48] J.D. Hoefelmeyer, K. Niesz, G.A. Somorjai, T.D. Tilley, Nano Lett. 5 (2005) 435–438. DOI: 10.1021/nl048100g

[49] N.M. Ngo, H.-V. Tran, T.R. Lee, ACS Appl. Nano Mater. 5 (2022) 14051–14091. DOI: 10.1021/acsanm.2c02533

[50] P. Senthil Kumar, I. Pastoriza-Santos, B. Rodríguez-González, F. Javier García de Abajo, L.M. Liz-Marzán, Nanotechnology 19 (2008) 015606. DOI: 10.1088/0957-4484/19/01/015606

[51] M.B. Mohamed, K.Z. Ismail, S. Link, M.A. El-Sayed, J. Phys. Chem. B 102 (1998) 9370–9374. DOI: 10.1021/jp9831482

[52] N.R. Jana, L. Gearheart, C.J. Murphy, Adv. Mater. 13 (2001) 1389–1393. DOI: 10.1002/1521-4095(200109)13:18<1389::AID-ADMA1389>3.0.CO;2-F

[53] C.L. Nehl, H. Liao, J.H. Hafner, Nano Lett. 6 (2006) 683–688. DOI: 10.1021/nl052409y

[54] S. Chen, Z.L. Wang, J. Ballato, S.H. Foulger, D.L. Carroll, J. Am. Chem. Soc. 125 (2003) 16186–16187. DOI: 10.1021/ja038927x

[55] M. Schütz, D. Steinigeweg, M. Salehi, K. Kömpe, S. Schlücker, Chem. Commun. 47 (2011) 4216. DOI: 10.1039/c0cc05229a

[56] H. Yuan, C.G. Khoury, H. Hwang, C.M. Wilson, G.A. Grant, T. Vo-Dinh, Nanotechnology 23 (2012) 075102. DOI: 10.1088/0957-4484/23/7/075102

[57] S. Sasidharan, D. Bahadur, R. Srivastava, RSC Adv. 6 (2016) 84025–84034. DOI: 10.1039/C6RA11405A

[58] I. Jung, S. Lee, S. Lee, J. Kim, S. Kwon, H. Kim, S. Park, Chem. Rev. 125 (2025) 7321–7388. DOI: 10.1021/acs.chemrev.4c00897

[59] K. Loza, M. Heggen, M. Epple, Adv. Funct. Mater. 30 (2020). DOI: 10.1002/adfm.201909260

[60] M. Sankar, N. Dimitratos, P.J. Miedziak, P.P. Wells, C.J. Kiely, G.J. Hutchings, Chem. Soc. Rev. 41 (2012) 8099. DOI: 10.1039/c2cs35296f

[61] N. Blommaerts, H. Vanrompay, S. Nuti, S. Lenaerts, S. Bals, S.W. Verbruggen, Small 15 (2019) 1–8. DOI: 10.1002/smll.201902791

[62] T. Fu, J. Fang, C. Wang, J. Zhao, J. Mater. Chem. A 4 (2016) 8803–8811. DOI: 10.1039/C6TA02202B

[63] A.G.M. da Silva, T.S. Rodrigues, S.J. Haigh, P.H.C. Camargo, Chem. Commun. 53 (2017) 7135–7148. DOI: 10.1039/C7CC02352A

[64] I. Lee, S.W. Han, K. Kim, Chem. Commun. 1 (2001) 1782–1783. DOI: 10.1039/b105437f

[65] A.K. Verma, R.K. Soni, Opt. Laser Technol. 163 (2023) 109429. DOI: 10.1016/j.optlastec.2023.109429

[66] M. Alheshibri, Nanomaterials 13 (2023) 2940. DOI: 10.3390/nano13222940

[67] R. Intartaglia, G. Das, K. Bagga, A. Gopalakrishnan, A. Genovese, M. Povia, E. Di Fabrizio, R. Cingolani, A. Diaspro, F. Brandi, Phys. Chem. Chem. Phys. 15 (2013) 3075–3082. DOI: 10.1039/C2CP42656K

[68] G. Li, Z. Tang, Nanoscale 6 (2014) 3995–4011. DOI: 10.1039/C3NR06787D

[69] P. Rai, Sustain. Energy Fuels 3 (2019) 63–91. DOI: 10.1039/C8SE00336J

[70] R.T. Tom, A.S. Nair, N. Singh, M. Aslam, C.L. Nagendra, R. Philip, K. Vijayamohanan, T. Pradeep, Langmuir 19 (2003) 3439–3445. DOI: 10.1021/la0266435

[71] S. Liu, M.D. Regulacio, S.Y. Tee, Y.W. Khin, C.P. Teng, L.D. Koh, G. Guan, M.-Y. Han, Chem. Rec. 16 (2016) 1965–1990. DOI: 10.1002/tcr.201600028

[72] R. Ghosh Chaudhuri, S. Paria, Chem. Rev. 112 (2012) 2373–2433. DOI: 10.1021/cr100449n

[73] R. Purbia, S. Paria, Nanoscale 7 (2015) 19789–19873. DOI: 10.1039/C5NR04729C

[74] Z. Chen, Z.-M. Cui, F. Niu, L. Jiang, W.-G. Song, Chem. Commun. 46 (2010) 6524. DOI: 10.1039/c0cc01786h

[75] Y. Dai, B. Lim, Y. Yang, C.M. Cobley, W. Li, E.C. Cho, B. Grayson, P.T. Fanson, C.T. Campbell, Y. Sun, Y. Xia, Angew. Chemie Int. Ed. 49 (2010) 8165–8168. DOI: 10.1002/anie.201001839

[76] M.-H. Jung, Y.J. Yun, M.-J. Chu, M.G. Kang, Chem. – A Eur. J.

19 (2013) 8543–8549. DOI: 10.1002/chem.201300834

[77] L.M. Liz-Marzán, A.P. Philipse, J. Colloid Interface Sci. 176 (1995) 459–466. DOI: 10.1006/jcis.1995.9945

[78] L.M. Liz-Marzán, M. Giersig, P. Mulvaney, Langmuir 12 (1996) 4329–4335. DOI: 10.1021/la9601871

[79] W. Stöber, A. Fink, E. Bohn, J. Colloid Interface Sci. 26 (1968) 62–69. DOI: 10.1016/0021-9797(68)90272-5

[80] T. Ung, L.M. Liz-Marzán, P. Mulvaney, Langmuir 14 (1998) 3740–3748. DOI: 10.1021/la980047m

[81] T. Ung, L.M. Liz-Marzán, P. Mulvaney, J. Phys. Chem. B 103 (1999) 6770–6773. DOI: 10.1021/jp991111r

[82] P. Mulvaney, M. Giersig, T. Ung, L.M. Liz-Marzán, Adv. Mater. 9 (1997) 570–575. DOI: 10.1002/adma.19970090712

[83] C. Graf, D.L.J. Vossen, A. Imhof, A. van Blaaderen, Langmuir 19 (2003) 6693–6700. DOI: 10.1021/la0347859

[84] C. Fernández-López, C. Mateo-Mateo, R.A. Álvarez-Puebla, J. Pérez-Juste, I. Pastoriza-Santos, L.M. Liz-Marzán, Langmuir 25 (2009) 13894–13899. DOI: 10.1021/la9016454

[85] V. Salgueiriño-Maceira, M.A. Correa-Duarte, M. Spasova, L.M. Liz-Marzán, M. Farle, Adv. Funct. Mater. 16 (2006) 509–514. DOI: 10.1002/adfm.200500565

[86] I. Pastoriza-Santos, J. Pérez-Juste, L.M. Liz-Marzán, Chem. Mater. 18 (2006) 2465–2467. DOI: 10.1021/cm060293g

[87] O. Niitsoo, A. Couzis, J. Colloid Interface Sci. 354 (2011) 887–890. DOI: 10.1016/j.jcis.2010.11.013

[88] C.T. Kresge, M.E. Leonowicz, W.J. Roth, J.C. Vartuli, J.S. Beck, Nature 359 (1992) 710–712. DOI: 10.1038/359710a0

[89] R.I. Nooney, T. Dhanasekaran, Y. Chen, R. Josephs, A.E. Ostafin, Adv. Mater. 14 (2002) 529–532. DOI: 10.1002/1521-4095(20020404)14:7<529::AID-ADMA529>3.0.CO;2-H

[90] P. Botella, A. Corma, M.T. Navarro, Chem. Mater. 19 (2007) 1979–1983. DOI: 10.1021/cm0629457

[91] I. Gorelikov, N. Matsuura, Nano Lett. 8 (2008) 369–373. DOI: 10.1021/nl0727415

[92] W.-C. Wu, J.B. Tracy, Chem. Mater. 27 (2015) 2888–2894. DOI: 10.1021/cm504764v

[93] C. Hanske, M.N. Sanz-Ortiz, L.M. Liz-Marzán, Adv. Mater. 30 (2018) 1707003. DOI: 10.1002/adma.201707003

[94] R.K. Kankala, H. Zhang, C.-G. Liu, K.R. Kanubaddi, C.-H. Lee, S.-B. Wang, W. Cui, H.A. Santos, K. Lin, A.-Z. Chen, Adv. Funct. Mater. 29 (2019) 1902652. DOI: 10.1002/adfm.201902652

[95] P. Dikshit, J. Kumar, A. Das, S. Sadhu, S. Sharma, S. Singh, P. Gupta, B. Kim, Catalysts 11 (2021) 902. DOI: 10.3390/catal11080902

[96] S. Ying, Z. Guan, P.C. Ofoegbu, P. Clubb, C. Rico, F. He, J. Hong, Environ. Technol. Innov. 26 (2022) 102336. DOI: 10.1016/j.eti.2022.102336

[97] S. Swain, S.K. Barik, T. Behera, S.K. Nayak, S.K. Sahoo, S.S. Mishra, P. Swain, Bionanoscience 6 (2016) 205–213. DOI: 10.1007/s12668-016-0208-y

[98] V. Dhand, L. Soumya, S. Bharadwaj, S. Chakra, D. Bhatt, B. Sreedhar, Mater. Sci. Eng. C 58 (2016) 36–43. DOI: 10.1016/j.msec.2015.08.018

[99] N. González-Ballesteros, S. Prado-López, J.B. Rodríguez-González, M. Lastra, M.C. Rodríguez-Argüelles, Colloids Surfaces B Biointerfaces 153 (2017) 190–198. DOI: 10.1016/j.colsurfb.2017.02.020

[100] A. Chahardoli, N. Karimi, A. Fattahi, Adv. Powder Technol. 29 (2018) 202–210. DOI: 10.1016/j.apt.2017.11.003

[101] T. Ahmad, M. Irfan, S. Bhattacharjee, Procedia Eng. 148 (2016) 1396–1401. DOI: 10.1016/j.proeng.2016.06.558

[102] M.D. Regulacio, D.-P. Yang, E. Ye, CrystEngComm 22 (2020) 399–411. DOI: 10.1039/C9CE01561B

[103] R. Rodríguez-Oliveros, R. Paniagua-Domínguez, J.A. Sánchez-Gil, D. Macías, Nanospectroscopy 1 (2016). DOI: 10.1515/nansp-2015-0006

[104] Y. Xia, D.J. Campbell, J. Chem. Educ. 84 (2007) 91. DOI: 10.1021/ed084p91

[105] K.E. Fong, L.-Y.L. Yung, Nanoscale 5 (2013) 12043. DOI: 10.1039/c3nr02257a

[106] B.J. Wiley, S.H. Im, Z.-Y. Li, J. McLellan, A. Siekkinen, Y. Xia, J. Phys. Chem. B 110 (2006) 15666–15675. DOI: 10.1021/jp0608628

[107] L. Wang, M. Hasanzadeh Kafshgari, M. Meunier, Adv. Funct. Mater. 30 (2020) 2005400. DOI: 10.1002/adfm.202005400

[108] Antimicrobial Resistance Collaborators. Global burden of bacterial antimicrobial resistance in 2019: a systematic analysis. Lancet. 2022 Feb 12;399(10325):629-655. doi: 10.1016/S0140-6736(21)02724-0. Epub 2022 Jan 19. Erratum in: Lancet. 2022 Oct 1;400(10358):1102. doi: 10.1016/S0140-6736(21)02653-2. PMID: 35065702; PMCID: PMC8841637.

[109] L.P. Silva, A.P. Silveira, C.C. Bonatto, I.G. Reis, P. V Milreu, in: A. Ficai, A.M. Grumezescu (Eds.), Nanostructures Antimicrob. Ther., Elsevier, 2017, pp. 577–596. DOI: 10.1016/B978-0-323-46152-8.00026-3

[110] E. Sánchez-López, D. Gomes, G. Esteruelas, L. Bonilla, A.L. Lopez-Machado, R. Galindo, A. Cano, M. Espina, M. Ettcheto, A. Camins, A.M. Silva, A. Durazzo, A. Santini, M.L. Garcia, E.B. Souto, Nanomaterials 10 (2020) 292. DOI: 10.3390/nano10020292

[111] A.P. Ingle, N. Duran, M. Rai, Appl. Microbiol. Biotechnol. 98 (2014) 1001–1009. DOI: 10.1007/s00253-013-5422-8

[112] A.S. Dove, D.I. Dzurny, W.R. Dees, N. Qin, C.C. Nunez Rodriguez, L.A. Alt, G.L. Ellward, J.A. Best, N.G. Rudawski, K. Fujii, D.M. Czyż, Front. Microbiol. 13 (2023). DOI: 10.3389/fmicb.2022.1064095

[113] R. Vazquez-Muñoz, A. Meza-Villezcas, P.G.J. Fournier, E. Soria-Castro, K. Juarez-Moreno, A.L. Gallego-Hernández, N. Bogdanchikova, R. Vazquez-Duhalt, A. Huerta-Saquero, PLoS One 14 (2019) e0224904. DOI: 10.1371/journal.pone.0224904

[114] U.H. Abo-Shama, H. El-Gendy, W.S. Mousa, R.A. Hamouda, W.E. Yousuf, H.F. Hetta, E.E. Abdeen, Infect. Drug Resist. Volume 13 (2020) 351–362. DOI: 10.2147/IDR.S234425

[115] D. Gupta, A. Singh, A.U. Khan, Nanoscale Res. Lett. 12 (2017) 454. DOI: 10.1186/s11671-017-2222-6

[116] M. Smekalova, V. Aragon, A. Panacek, R. Prucek, R. Zboril, L. Kvitek, Vet. J. 209 (2016) 174–179. DOI: 10.1016/j.tvjl.2015.10.032

[117] A. Mohandas, S. Deepthi, R. Biswas, R. Jayakumar, Bioact. Mater. 3 (2018) 267–277. DOI: 10.1016/j.bioactmat.2017.11.003

[118] X. Yang, J. Hou, Y. Tian, J. Zhao, Q. Sun, S. Zhou, Sci. China Technol. Sci. 65 (2022) 1000–1010. DOI: 10.1007/s11431-021-1962-x

[119] G. Benetti, E. Cavaliere, R. Brescia, S. Salassi, R. Ferrando, A. Vantomme, L. Pallecchi, S. Pollini, S. Boncompagni, B. Fortuni, M.J. Van Bael, F. Banfi, L. Gavioli, Nanoscale 11 (2019) 1626–1635. DOI: 10.1039/C8NR08375D

[120] S. Cometa, R. Iatta, M.A. Ricci, C. Ferretti, E. De Giglio, J. Bioact. Compat. Polym. 28 (2013) 508–522. DOI: 10.1177/0883911513498960

[121] A. Elbourne, R.J. Crawford, E.P. Ivanova, J. Colloid Interface Sci. 508 (2017) 603–616. DOI: 10.1016/j.jcis.2017.07.021

[122] G. Mi, D. Shi, M. Wang, T.J. Webster, Adv. Healthc. Mater. 7 (2018) 1800103. DOI: 10.1002/adhm.201800103

[123] M. Liong, B. France, K.A. Bradley, J.I. Zink, Adv. Mater. 21 (2009) 1684–1689. DOI: 10.1002/adma.200802646

[124] Y. Wang, X. Ding, Y. Chen, M. Guo, Y. Zhang, X. Guo, H. Gu, Biomaterials 101 (2016) 207–216. DOI: 10.1016/j.biomaterials.2016.06.004

[125] Q. Liu, Y. Zhang, J. Huang, Z. Xu, X. Li, J. Yang, H. Huang, S. Tang, Y. Chai, J. Lin, C. Yang, J. Liu, S. Lin, J. Nanobiotechnology 20 (2022) 386. DOI: 10.1186/s12951-022-01600-9

[126] S. Patskovsky, E. Bergeron, D. Rioux, M. Simard, M. Meunier, Analyst 139 (2014) 5247–5253. DOI: 10.1039/C4AN01063A

[127] H. Xu, Q. Li, L. Wang, Y. He, J. Shi, B. Tang, C. Fan, Chem. Soc. Rev. 43 (2014) 2650. DOI: 10.1039/c3cs60309a

[128] K. Seekell, M.J. Crow, S. Marinakos, J. Ostrander, A. Chilkoti, W. Adam, J. Biomed. Opt. 16 (2011) 116003. DOI: 10.1117/1.3646529

[129] A. Nsamela Matombi, M. Hasanzadeh Kafshgari, L. Wang, S. Patskovsky, D. Trudel, M. Meunier, ACS Appl. Nano Mater. 3 (2020) 4171–4177. DOI: 10.1021/acsanm.0c00376

[130] Q. Zhan, J. Qian, X. Li, S. He, Nanotechnology 21 (2010) 055704. DOI: 10.1088/0957-4484/21/5/055704

[131] Y. Mantri, J. V Jokerst, ACS Nano 14 (2020) 9408–9422. DOI: 10.1021/acsnano.0c05215

[132] S.G. Alamdari, M. Amini, N. Jalilzadeh, B. Baradaran, R. Mohammadzadeh, A. Mokhtarzadeh, F. Oroojalian, J. Control. Release 349 (2022) 269–303. DOI: 10.1016/j.jconrel.2022.06.050

[133] A.V.P. Kumar, S.K. Dubey, S. Tiwari, A. Puri, S. Hejmady, B. Gorain, P. Kesharwani, Int. J. Pharm. 606 (2021) 120848. DOI: 10.1016/j.ijpharm.2021.120848

[134] Z. Liang, C. Cao, J. Gao, W. Cai, J. Li, D. Wu, Y. Kong, ACS Appl. Nano Mater. 5 (2022) 7440–7448. DOI: 10.1021/acsanm.2c01448

[135] N.T. Ha Lien, A.D. Phan, B.T. Van Khanh, N.T. Thuy, N. Trong Nghia, H.T. My Nhung, T. Hong Nhung, D. Quang Hoa, V. Duong, N. Minh Hue, ACS Omega 5 (2020) 20231–20237. DOI: 10.1021/acsomega.0c01939

[136] Z. Zhang, J. Wang, C. Chen, Adv. Mater. 25 (2013) 3869–3880. DOI: 10.1002/adma.201301890

[137] Z. Lv, S. He, Y. Wang, X. Zhu, Adv. Healthc. Mater. 10 (2021) 2001806. DOI: 10.1002/adhm.202001806

[138] A. Espinosa, J. Reguera, A. Curcio, Á. Muñoz-Noval, C. Kuttner, A. Van de Walle, L.M. Liz-Marzán, C. Wilhelm, Small 16

(2020) 1904960. DOI: 10.1002/smll.201904960

[139] A. Amirjani, D.F. Haghshenas, Sensors Actuators B Chem. 273 (2018) 1768–1779. DOI: 10.1016/j.snb.2018.07.089

[140] A. Fernández-Lodeiro, J. Fernández-Lodeiro, C. Núñez, R. Bastida, J.L. Capelo, C. Lodeiro, ChemistryOpen 2 (2013) 200–207. DOI: 10.1002/open.201300023

[141] J. Djafari, C. Marinho, T. Santos, G. Igrejas, C. Torres, J.L. Capelo, P. Poeta, C. Lodeiro, J. Fernández-Lodeiro, ChemistryOpen 5 (2016) 206–212. DOI: 10.1002/open.201600016

[142] D. Sahu, N. Sarkar, G. Sahoo, P. Mohapatra, S.K. Swain, Sensors Actuators B Chem. 246 (2017) 96–107. DOI: 10.1016/j.snb.2017.01.038

[143] S. Li, T. Wei, M. Tang, F. Chai, F. Qu, C. Wang, Sensors Actuators B Chem. 255 (2018) 1471–1481. DOI: 10.1016/j.snb.2017.08.159

[144] A. Amirjani, E. Rahbarimehr, Microchim. Acta 188 (2021) 57. DOI: 10.1007/s00604-021-04714-3

[145] A. Minopoli, A. Acunzo, B. Della Ventura, R. Velotta, Adv. Mater. Interfaces 9 (2022) 2101133. DOI: 10.1002/admi.202101133

[146] M. Fleischmann, P.J. Hendra, A.J. McQuillan, Chem. Phys. Lett. 26 (1974) 163–166. DOI: 10.1016/0009-2614(74)85388-1

[147] S. Schlücker, Angew. Chemie Int. Ed. 53 (2014) 4756–4795. DOI: 10.1002/anie.201205748

[148] N. Akkilic, S. Geschwindner, F. Höök, Biosens. Bioelectron. 151 (2020) 111944. DOI: 10.1016/j.bios.2019.111944

[149] A. Sultangaziyev, R. Bukasov, Sens. Bio-Sensing Res. 30 (2020) 100382. DOI: 10.1016/j.sbsr.2020.100382

[150] S. Tu, D. Rioux, J. Perreault, D. Brouard, M. Meunier, J. Phys. Chem. C 121 (2017) 8944–8951. DOI: 10.1021/acs.jpcc.6b11954

[151] M. Haruta, T. Kobayashi, H. Sano, N. Yamada, Chem. Lett. 16 (1987) 405–408. DOI: 10.1246/cl.1987.405

[152] A. Sápi, T. Rajkumar, J. Kiss, Á. Kukovecz, Z. Kónya, G.A. Somorjai, Catal. Letters 151 (2021) 2153–2175. DOI: 10.1007/s10562-020-03477-5

[153] K. An, G.A. Somorjai, ChemCatChem 4 (2012) 1512–1524. DOI: 10.1002/cctc.201200229

[154] Z. Li, S. Ji, Y. Liu, X. Cao, S. Tian, Y. Chen, Z. Niu, Y. Li, Chem. Rev. 120 (2020) 623–682. DOI: 10.1021/acs.chemrev.9b00311

[155] B. Hvolbæk, T.V.W. Janssens, B.S. Clausen, H. Falsig, C.H. Christensen, J.K. Nørskov, Nano Today 2 (2007) 14–18. DOI: 10.1016/S1748-0132(07)70113-5

[156] S. Linic, P. Christopher, H. Xin, A. Marimuthu, Acc. Chem. Res. 46 (2013) 1890–1899. DOI: 10.1021/ar3002393

[157] K.M. Bratlie, H. Lee, K. Komvopoulos, P. Yang, G.A. Somorjai, Nano Lett. 7 (2007) 3097–3101. DOI: 10.1021/nl0716000

[158] C. Gao, F. Lyu, Y. Yin, Chem. Rev. 121 (2021) 834–881. DOI: 10.1021/acs.chemrev.0c00237

[159] T. Zhang, H. Zhao, S. He, K. Liu, H. Liu, Y. Yin, C. Gao, ACS Nano 8 (2014) 7297–7304. DOI: 10.1021/nn502349k

[160] S. Wang, M. Zhang, W. Zhang, ACS Catal. 1 (2011) 207–211. DOI: 10.1021/cs1000762

[161] C. Wang, L. Wang, J. Zhang, H. Wang, J.P. Lewis, F.-S. Xiao, J. Am. Chem. Soc. 138 (2016) 7880–7883. DOI: 10.1021/jacs.6b04951

[162] J. Lee, J.C. Park, J.U. Bang, H. Song, Chem. Mater. 20 (2008) 5839–5844. DOI: 10.1021/cm801149w

[163] A.K. Singh, Q. Xu, ChemCatChem 5 (2013) 652–676. DOI: 10.1002/cctc.201200591

[164] I. Mustieles Marin, J.M. Asensio, B. Chaudret, ACS Nano 15 (2021) 3550–3556. DOI: 10.1021/acsnano.0c09744

[165] L.M. Bronstein, D.M. Chernyshov, I.O. Volkov, M.G. Ezernitskaya, P.M. Valetsky, V.G. Matveeva, E.M. Sulman, J. Catal. 196 (2000) 302–314. DOI: 10.1006/jcat.2000.3039

[166] J. Zhang, G. Chen, D. Guay, M. Chaker, D. Ma, Nanoscale 6 (2014) 2125–2130. DOI: 10.1039/C3NR04715F

[167] F. Godínez-Salomón, M. Hallen-López, O. Solorza-Feria, Int. J. Hydrogen Energy 37 (2012) 14902–14910. DOI: 10.1016/j.ijhydene.2012.01.157

[168] S. Linic, P. Christopher, D.B. Ingram, Nat. Mater. 10 (2011) 911–921. DOI: 10.1038/nmat3151

[169] A. Kumar, P. Choudhary, A. Kumar, P.H.C. Camargo, V. Krishnan, Small 18 (2022) 2101638. DOI: 10.1002/smll.202101638

[170] A. Zaleska-Medynska, M. Marchelek, M. Diak, E. Grabowska, Adv. Colloid Interface Sci. 229 (2016) 80–107. DOI: 10.1016/j.cis.2015.12.008

[171] A. Zielińska-Jurek, E. Kowalska, J.W. Sobczak, W. Lisowski, B. Ohtani, A. Zaleska, Appl. Catal. B Environ. 101 (2011) 504–514. DOI: 10.1016/j.apcatb.2010.10.022

[172] Y. Mizukoshi, K. Sato, T.J. Konno, N. Masahashi, Appl. Catal. B Environ. 94 (2010) 248–253. DOI: 10.1016/j.apcatb.2009.11.015

[173] J.B. Priebe, J. Radnik, A.J.J. Lennox, M.-M. Pohl, M. Karnahl, D. Hollmann, K. Grabow, U. Bentrup, H. Junge, M. Beller, A. Brückner, ACS Catal. 5 (2015) 2137–2148. DOI: 10.1021/cs5018375

[174] K. Qian, B.C. Sweeny, A.C. Johnston-Peck, W. Niu, J.O. Graham, J.S. DuChene, J. Qiu, Y.-C. Wang, M.H. Engelhard, D. Su, E.A. Stach, W.D. Wei, J. Am. Chem. Soc. 136 (2014) 9842–9845. DOI: 10.1021/ja504097v

[175] H. Liang, Q. Meng, X. Wang, H. Zhang, J. Wang, ACS Appl. Mater. Interfaces 10 (2018) 14145–14152. DOI: 10.1021/acsami.8b00677

[176] J. Nie, A.O.T. Patrocinio, S. Hamid, F. Sieland, J. Sann, S. Xia, D.W. Bahnemann, J. Schneider, Phys. Chem. Chem. Phys. 20 (2018) 5264–5273. DOI: 10.1039/C7CP07762A

[177] S.K. Karuppannan, R. Ramalingam, S.B. Mohamed Khalith, M.J.H. Dowlath, G.I. Darul Raiyaan, K.D. Arunachalam, Biocatal. Agric. Biotechnol. 31 (2021) 101904. DOI: 10.1016/j.bcab.2020.101904

[178] V. Seerangaraj, S. Sathiyavimal, S.N. Shankar, J.G.T. Nandagopal, P. Balashanmugam, F.A. Al-Misned, M. Shanmugavel, P. Senthilkumar, A. Pugazhendhi, J. Environ. Chem. Eng. 9 (2021) 105088. DOI: 10.1016/j.jece.2021.105088

[179] S.A. Anjugam Vandarkuzhali, N. Pugazhenthiran, R. V Mangalaraja, P. Sathishkumar, B. Viswanathan, S. Anandan, ACS Omega 3 (2018) 9834–9845. DOI: 10.1021/acsomega.8b01322

[180] X. Zhu, C. Jin, X.-S. Li, J.-L. Liu, Z.-G. Sun, C. Shi, X. Li, A.-M. Zhu, ACS Catal. 7 (2017) 6514–6524. DOI: 10.1021/acscatal.7b01658

[181] Y. Wang, C. Yang, A. Chen, W. Pu, J. Gong, Appl. Catal. B Environ. 251 (2019) 57–65. DOI: 10.1016/j.apcatb.2019.03.056

[182] J. Low, S. Qiu, D. Xu, C. Jiang, B. Cheng, Appl. Surf. Sci. 434 (2018) 423–432. DOI: 10.1016/j.apsusc.2017.10.194

[183] Y. Lan, Y. Xie, J. Chen, Z. Hu, D. Cui, Chem. Commun. 55 (2019) 8068–8071. DOI: 10.1039/C9CC02891A

[184] D.J. de Aberasturi, A.B. Serrano-Montes, L.M. Liz-Marzán, Adv. Opt. Mater. 3 (2015) 602–617. DOI: 10.1002/adom.201500053

[185] J.-L. Wu, F.-C. Chen, Y.-S. Hsiao, F.-C. Chien, P. Chen, C.-H. Kuo, M.H. Huang, C.-S. Hsu, ACS Nano 5 (2011) 959–967. DOI: 10.1021/nn102295p

[186] H. Choi, J.-P. Lee, S.-J. Ko, J.-W. Jung, H. Park, S. Yoo, O. Park, J.-R. Jeong, S. Park, J.Y. Kim, Nano Lett. 13 (2013) 2204–2208. DOI: 10.1021/nl400730z

[187] S. Chang, Q. Li, X. Xiao, K.Y. Wong, T. Chen, Energy Environ. Sci. 5 (2012) 9444. DOI: 10.1039/c2ee22657j

[188] R. Selvapriya, T. Abhijith, V. Ragavendran, V. Sasirekha, V.S. Reddy, J.M. Pearce, J. Mayandi, J. Alloys Compd. 894 (2022) 162339. DOI: 10.1016/j.jallcom.2021.162339

TRANSLATIONAL CHEMISTRY
AN INTERFACE JOURNAL
HTTPS://WWW.TRANSLATIONALCHEMISTRY.COM/

REVIEW ARTICLE | DOI: 10.5584/translationalchemistry.v1i2.251

# Cationic Compounds in Antimicrobial Therapy: Structure–Activity Relationships and Emerging Technologies

Gaspare Crisà [1], Sara Amata [1], Carla Rizzo [1,*], Silvestre Buscemi [1], Antonio Palumbo Piccionello [1,*]

[1]Department of Biological Chemical and Pharmaceutical Sciences and Technologies, Section of Chemistry, University of Palermo, Viale delle Scienze, Ed. 17, 90128 Palermo, Italy.

**Received:** 10 December 2025 **Accepted:** 17 December 2025 **Available Online**: 29 December 2025

ABSTRACT

The phenomenon of antibiotic resistance is one of the most pressing challenges of our modern age. The development of multidrug-resistant bacteria poses a serious threat to public health. Therefore, it is necessary to develop new therapeutic strategies that are a viable alternative to conventional antibiotics and, at the same time, effectively and concretely overcome their current limitations. The most promising synthetic approaches are oriented towards the use of cationic compounds, which have a physicochemical mechanism of action based on electrostatic interactions with bacterial membranes; targeting this mechanism reduces the possibility of resistance developing. Cationic compounds include antimicrobial peptides, cationic polymers, quaternary ammonium and quaternary phosphonium salts, and Gemini surfactants. This review offers a comprehensive summary of recent advancements in cationic antimicrobial platforms, highlighting the structure-activity relationships, mechanisms of action, and design strategies, illustrating how these molecules can achieve enhanced efficacy and biocompatibility for humans. Natural AMPs and their synthetic analogues have facilitated the creation of novel polymer topologies and self-assembling systems exhibiting rapid, multi-target efficacy. Cationic polymers serve as the foundation for the creation of "contact-active" antibacterial coatings and anti-biofilm materials by adjusting their charge and hydrophobicity. finally, Gemini surfactants and cationic systems create structural synergy by integrating antibacterial efficacy, biodegradability, and potential theranostic applications. Furthermore, the issues concerning environmental sustainability, biocompatibility, and the incorporation of intelligent and stimulus-responsive systems are also addressed. Developing novel antimicrobial compounds that are effective, selective, and sustainable necessitates a multidisciplinary collaboration among chemistry, materials science, and microbiology.

**Keywords:** Cationic antimicrobials; Antimicrobial peptides; Quaternary ammonium-phosphonium salts; Gemini surfactants; Antimicrobial resistance; Structure–activity relationships.

## 1. Introduction

### 1.1. Antibiotic resistance: global overview and limitations of traditional therapies

One of the greatest threats to global public health is associated with the worrying increase in infections caused by multi-drug resistant (MDR) bacteria. According to a well-known assessment commissioned by the British government, antimicrobial resistance es expected to cause more than 10 million deaths per year by 2050, with a severe economic impact on global health systems [1]. The socio-economic consequences of antibiotic resistance are substantial, including increased treatment costs, longer hospital admissions, and mortality related to this phenomenon [2].

This occurrence is intensified by a combination of biological and anthropogenic factors. The main molecular mechanisms underlying the emergence, spread, and transmission of resistance genes among bacteria are mainly due to genetic mutations in the bacteria themselves and horizontal gene transfer through plasmids and transposons [3,4]. Another emerging factor influencing the selection of resistant strains is, alongside environmental dispersion, the improper use of antibiotics in both medical and agricultural contexts [5].

### 1.2. Biofilm and microbial persistence

Biofilms are crucial to the persistence of bacterial infections. Biofilms are three-dimensional structures consisting of microbial communities embedded in an extracellular matrix. This

***Corresponding author:** Antonio Piccionello; antonio.palumbopiccionello@unipa.it | Carla Rizzo; carla.rizzo03@unipa.it

extracellular matrix serves as a physical and chemical barrier against pharmaceuticals and the host's immune responses. This results in resistance to antimicrobial treatment, rendering it ineffective and increasing the chance of relapse following traditional treatment. Biofilms are implicated in various infections and have been shown to play a critical role in the chronicity of human diseases. The onset of biofilm-related infections is not only responsible for an increase in severe symptoms but also has a significant impact on related mortality [6,7].

### 1.3. Cationic molecules: a new frontier in antimicrobials

The ineffectiveness of conventional drugs has directed research towards the study of novel strategies and antimicrobial agents capable of overcoming the resistance mechanisms of multi-resistant bacteria. Among the emerging strategies, particular attention is being paid to cationic compounds, which include antimicrobial peptides, cationic polymers, quaternary ammonium salts, phosphonium and gemini surfactants. The distinguishing characteristic of these compounds is the presence of positive charges, which promote interaction with negatively charged bacterial membranes, particularly anionic lipids, lipopolysaccharides and teichoic acids [8]. The electrostatic interaction between these compounds and the membranes causes destabilisation of the phospholipid bilayer, loss of membrane potential, and consequent cell death. In contrast with traditional antibiotics that target specific molecular sites, cationic agents exert a multifaceted physicochemical mechanism that is challenging to evade through mere point mutations. Furthermore, they have fast kinetics of action and provide significant efficacy against bacteria resistant to conventional antibiotics [9,10]. Simultaneously, materials engineering has enabled the incorporation of these antimicrobial compounds into advanced controlled-release systems on surfaces, rendering them antibacterial. These are employed to prevent of hospital-acquired infections. Cationic coatings for catheters and implantable devices have demonstrated efficacy in reducing biofilm formation, even in complex clinical conditions [11]. All this has paved the way for a new multifunctional approach to fighting infections. The aim of this review is to provide the first comprehensive and up-to-date overview (2022-2025) of the principal cationic antibacterial platforms, including quaternary ammonium compounds (QACs), cationic polymers, antimicrobial peptides (AMPs) and gemini surfactant systems. Unlike recent reviews available today, which all focus on individual cationic classes such as QACs [12,13], cationic polymers [14], AMPs [15,16] or gemini surfactants [17], this work offers a cross-sectional view of the entire landscape of cationic antibacterial materials. The review highlights the main common mechanisms of action and structure activity relationship (SAR) studies, integrating approaches usually carried out separately and demonstrating the interdisciplinarity and connection between them in guiding new design strategies. Recent advancements, together with a direct comparison of structural variations, stimulus-responsive materials and novel synthetic methodologies, enable the enhancement and acceleration of the synthesis of new antimicrobial agents. Overall, this review fills a gap in the current landscape, offering a broad and comparative analysis of cationic platforms, which is essential for accelerating the design of compounds capable of addressing the problem of antibiotic resistance. A comparative summary of the main cationic systems analysed is reported in **Figure 1.**

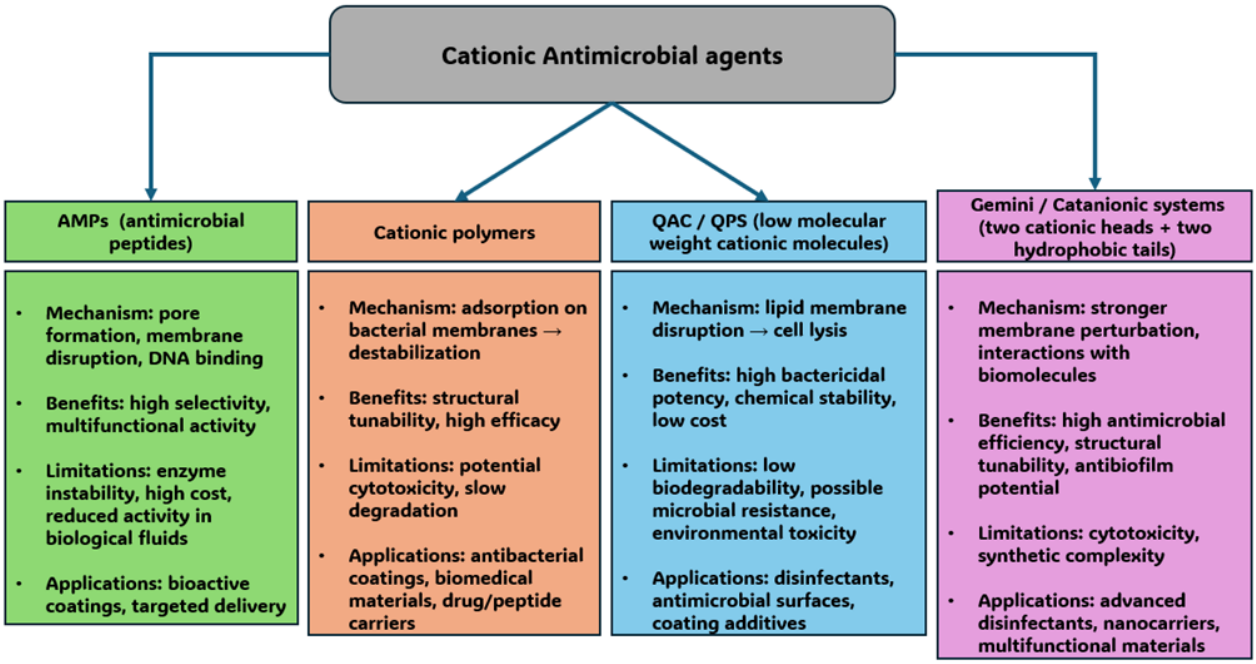


**Figure 1** | Comparison of the main classes of cationic antimicrobial compounds.

## 2. Antimicrobial Peptides (AMPs)

Antimicrobial peptides are naturally produced by several species, including humans, and are essential to the innate immune system. The first antimicrobial peptide, gramicidin, was discovered in 1939 by microbiologist Renè Dubos in a strain of Bacillus with anti-pneumococcal properties [18]. To date, the APD (Antimicrobial Peptide Database) contains over 5 000 AMPs, of which 3 000 are isolated from animal eukaryotes. These peptides are produced in response to bacterial infections and are capable of neutralising various pathogens [16,19–21]. Their adaptability mostly stems from their amphipathic structure, characterized by a net positive charge, and their ability to selectively recognise and interact with bacterial membranes, which are abundant in anionic phospholipids.

### 2.1 Mechanism of action and selectivity towards bacterial cells

The primary characteristic that has shifted attention towards AMPs as therapeutic agents is their physical and multimodal mechanism of action (**Figure 2**). Their mechanism involves electrostatic interactions with negatively charged bacterial membranes, leading to destabilisation through the insertion of hydrophobic portions, resulting in loss of membrane integrity and subsequent cell lysis. Secondary structures, such as α-helices and β-sheets, help form amphipathic regions that can induce pore formation (barrel-stave or toroidal) and membrane destabilization. This rapid, non-target-specific physical mechanism is responsible for their effectiveness against resistant strains and reduced the likelihood of resistance to development [22,23]. Numerous studies indicate that AMPs do not only target the membrane. In addition to causing physical damage to the phospholipid bilayer, certain peptides are able to penetrate the microbial cells and interfere with essential processes such as DNA, RNA and protein synthesis, as well as key enzyme activity and oxidative homeostasis. This multifunctionality broadens their therapeutic profile, making them a model of inspiration for the development of new synthetic cationic compounds capable of targeting multiple microbial targets simultaneously, while maintaining a low propensity for resistance [15]. The design of antimicrobial peptides exhibiting high bactericidal activity while maintaining low cytotoxicity towards human cells, characterized by good selectivity, can be achieved by modulating peptide length, overall hydrophobicity and charge distribution. These principles form the basis for the development of formulations and polymeric conjugates that increase their stability, bioavailability and specific targeting, while maintaining safety and compatibility with the host [23].

### 2.2 Synthetic peptides and mimetics: rational design and self-assembly

The clinical application of natural AMPs is severely limited due to high costs, metabolic instability and protein degradation. These factors have stimulated research and development into the synthesis of cationic peptidomimetics capable of preserving antimicrobial activity while improving stability characteristics [24–26]. To increase resistance to proteolysis, the most effective approach is to insert D-amino acids and the reinforcement of stability through stabilised cyclic or β-turn structures. Finally, interaction with membranes is promoted by the introduction of aromatic cationic units. Recent studies indicate that the strategic substitution of specific amino acids allows the modulation of key properties, such as positive charge and amphipathicity, thereby improving antimicrobial activity while minimizing cytotoxicity towards human cells. Peptides designed in this manner exhibit self-

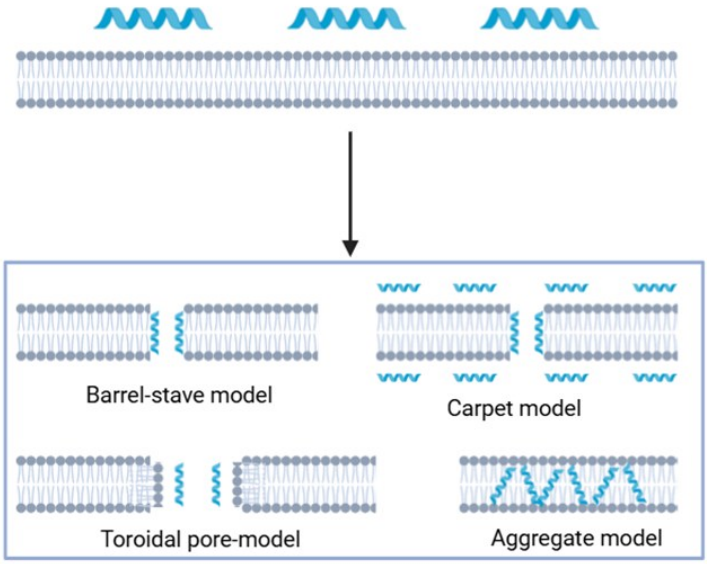


**Figure 2** | Main mechanisms of action of AMPs against bacterial membranes. After initial adsorption on the phospholipid surface, these molecules can destabilise the membrane through different mechanisms; Barrel stave, carpet model, toroidal pore model and aggregate model.

assembling in nanoparticles, promoting rapid destabilisation of bacterial membranes and exhibiting strong efficacy both *in vivo* and *in vitro* against multi-resistant Gram-negative pathogens. This highlights how rational design based on the study of the structural and physicochemical characteristics of AMPs can be a valuable guide for the discovery and synthesis of new peptidomimetics that are safe and effective [27]. Li *et al.* have recently developed new bis-pyridine cationic mimetics of antimicrobial peptides (**Figure 3**), demonstrating significant antibacterial activity against both Gram-positive and Gram-negative strains while exhibiting low haemolytic toxicity. These compounds are stable in complex body fluids, with rapid bactericidal activity, a prolonged post-antibiotic effect and a rapid reduction in *S. aureus* load. Furthermore, the bacteria showed a low propensity to develop resistance. Finally, these compounds also shown excellent anti-biofilm properties, effectively preventing biofilm formation and degrading established biofilms. These characteristics confirm the potential of these compounds as new antimicrobial agents mimicking AMPs [28].

### 2.3 Nanostructured delivery systems

A notable area of investigation involves the encapsulation of antimicrobial peptides in nanoparticles or polymeric vesicles. This strategy not only protects the peptides from proteolytic degradation and facilitates a more controlled release of these compounds. The optimisation of AMPs administration can be enhanced through the use of delivery systems based on biodegradable nanoparticles. Ali et al. have demonstrated in their studies that encapsulating antimicrobial peptides in poly(lactic-co-glycolic acid) (PLGA) nanoparticles reduces the MIC (Minimal Inhibitory Concentration) value by approximately 50% compared to the free peptide, significantly improves penetration and therefore effectiveness against biofilms, and preserves excellent biocompatibility of the compound. In complex infectious models, these systems have resulted in a reduction exceeding 95% in bacterial load, thereby confirming their effectiveness in more realistic biological systems. This demonstrates how the combined approach based on amino acid modification of peptides and encapsulation in nanoparticles represents an innovative and promising strategy to overcome the limitations of natural AMPs, improving, stability, antimicrobial activity and safety [29]. Another method entails the integration of quaternary ammonium and phosphonium groups into antimicrobial peptides. These provide the ability to enhance antimicrobial activity via multiple mechanisms of action. Cationic compounds exhibit selective interactions with bacterial membranes. Their activity is mainly attributed to the induction of respiratory dysfunction through the generation of reactive oxygen species and damage to intracellular biomolecules. These synergistic mechanisms are essential and promising for combating bacterial infections, especially those caused by antibiotic-resistant pathogens. Recent studies have shown how this combination of antimicrobial peptides with antibiotics can exert a synergistic action against S. suis through membrane disruption, ROS (Reactive Oxygen Species) induction and biofilm formation inhibition [30]. This multimodality and synergy pave the way for therapies that can be combined and used in tandem to target bacteria on multiple fronts simultaneously, improving treatment efficacy.

### 2.4 Biomedical applications and functionalised surfaces

An effective strategy for preventing bacterial colonisation and biofilm formation on medical devices is the immobilisation of antimicrobial peptides on biomedical surfaces. Unlike traditional therapeutic formulations, AMPs immobilised on surfaces provide extended local activity, reducing the risk of resistance and ensuring long-lasting efficacy. Recent studies have shown that the covalent immobilisation of antimicrobial peptides on the surfaces of catheters and orthopaedic implants surfaces can significantly reduce biofilm formation, hence enhancing the functionality and safety of these devices. A review conducted by Nicolas et al. analysed various techniques for immobilisation on biomedical devices surfaces, highlighting the mechanisms of action by which they prevent bacterial adhesion and biofilm formation. The authors, analysing immobilisation techniques on various materials in the biomedical field, emphasised the importance of maintaining the antimicrobial activity of AMPs during the immobilisation process [31]. The self-assembling properties, structural versatility and modular synthesis of AMPs have established them as one of the most promising antimicrobial platforms for tackling the global emergency of antibiotic resistance. The study of the properties of natural peptides has inspired and driven research towards the design of new synthetic cationic molecules capable of replicating their effectiveness but with greater stability and safety.

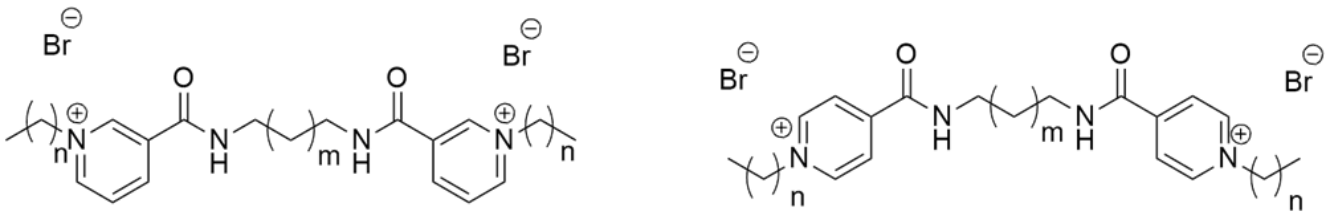


**Figure 3** | General structure of bis-pyridine cationic compounds [26].

## 3. Cationic polymers and salts

### 3.1 Cationic polymers: molecular design and advanced architectures

In recent years, numerous studies on cationic polymers have demonstrated their potential as effective antibacterial compounds against both Gram-positive and Gram-negative strains, exhibiting rapid action and a low likelihood of resistance development. Unlike traditional antibiotics, their target is the bacterial membrane; they act through electrostatic interactions between the positive charges along the polymer chain and the negatively charged bacterial surfaces [11]. An important feature of cationic polymers lies in their modularity, which permits the modification of their structural features through changes in their chemical and physical attributes. Recent studies have highlighted and identified three main parameters that influence the activity and selectivity of these compounds: cationic charge density, the balance between hydrophobicity and hydrophilicity, and polymer architecture. Excessive cationic charge increases the risk of haemolysis and cytotoxicity, while reduced hydrophobic content reduces affinity for the bacterial membrane, effectively compromising its antimicrobial activity [32]. Tyagi *et al.* conducted studies that demonstrated how varying the degree of polymerisation and the distribution of hydrophobic and cationic groups along the polymer chain leads to polymers with high antibacterial activity and low toxicity to human cells. The research emphasizes that the ability to interact with the bacterial membrane and the formation of pores is influenced by the architecture, which can be linear or branched. This provides supplementary tools for the rational synthesis of novel antimicrobial materials. Precise modification of chemical-structural parameters is therefore essential for developing effective and safe cationic polymers capable of acting against multi-resistant bacteria [33].

### 3.2 Miktoarm, star and imidazole copolymer architectures

An advanced approach to the design of antimicrobial agents is represented by core-cross-linked (CCS) cationic star polymers. Recently, Laroque *et al.* developed and conducted studies on diblock and miktoarm polymers, combining non-polar and cationic arms to modulate charge exposure. *In vitro* investigation demonstrated that miktoarms with cationic units more accessible to the bacterial membrane exhibit superior antibacterial activity against *Staphylococcus aureus*, while diblock polymers with partially shielded cationic units display reduced efficacy. In conclusion, these studies have shown how the miktoarm type can optimise interaction with the bacterial membrane, highlighting how crucial the balance between the number and length of cationic arms is to maximise antimicrobial efficacy with lower cytotoxicity [34]. Liu *et al.* developed imidazole-based cationic copolymers (**Figure 4**), which exhibited high bactericidal activity against *MRSA (Methicillin-Resistant Staphylococcus aureus)*, *S. aureus*, *E. faecalis*, *E. coli*, and *P. aeruginosa*. These compounds were associated with high biocompatibility with erythrocytes and mammalian cells. The antibacterial action was attributed to electrostatic interactions between these compounds and the membranes, along with the insertion of hydrophobic segments, resulting in membrane permeabilisation and depolarisation. Furthermore, they were determined to be highly effective in eradicating biofilms. An additional significant feature is their ability not to induce bacterial resistance after repeated exposure, thus highlighting their potential as safe and selective antibacterial agents for clinical applications, including medical coatings [35]. Similar research was conducted by Zhoung *et al.* on cationic main chain polymers containing imidazole units and adjusted hydrophobicity. These compounds showed good antibacterial activity against Gram-positive and Gram -negative pathogens, including resistant strains and mycobacteria. These polymers are absorbed by the cell in a manner dependent on the membrane potential ($\Delta\Psi$), and their effectiveness is maintained on actively growing bacteria but is limited on bacteria in the stationary phase. Furthermore, the polymers exhibit significant selectivity, minimal toxicity to mammalian cells, and do not induce resistance in non-fermentative bacteria. Finally, research using animal models has validated the therapeutic effectiveness against systemic skin infections, once again highlighting the potential of these copolymers as antibacterial agents [36].

### 3.3 Multifunctional and photoactive materials

Biofilms provide a significant challenge in hospital environments, prompting research into polymers capable of self-assembling or function as active vectors. Nabawy *et al.* have developed cationic alternating poly (phenylene ethynylene) (PPE) copolymers (CP_Cn_TMA) (**Figure 5**) with variable alkyl side chain lengths achieving a balance between hydrophobic groups and positive charges that effectively eradicate both Gram-positive and Gram-negative bacteria. They are efficient against multi-resistant clinical isolates due to their ability to penetrate biofilm and reduce more than 80% of extracellular biomass without inducing resistance and keeping low toxicity towards fibroblasts and red blood cells. Furthermore, they have also demonstrated efficacy in mouse models of skin infections [37].

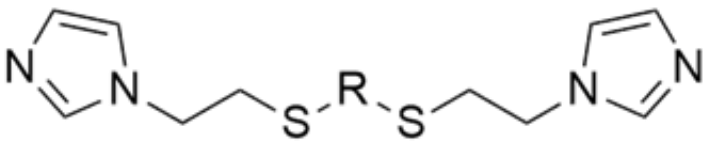


**Figure 4** | General structure of bi-imidazole monomer [33].

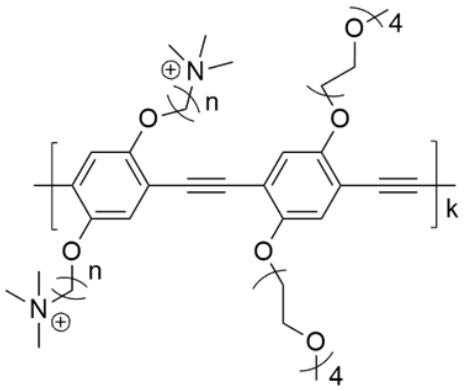

**Figure 5** | General structure of CP_Cn_TMA alternating copolymers [37].

Other studies have integrated photoactive groups into polymers to produce photodynamic materials capable of generating ROS under light, thereby increasing efficacy without increasing systemic toxicity. Ma *et al.* developed D–A type BPDS-COFs (Covalent Organic Frameworks based on 4,4'-bipyridine-2,2'-disulfonate) functionalised with pyridine (PY) and quaternary ammonium (QA) groups, effectively combining photoelectric and antibacterial activity. The material synthesised exhibits excellent crystallinity and porosity, along with enhanced hydrophilicity and chemical stability. This configuration promotes the separation of photo-induced electrons and the generation of active oxygen species capable of damaging bacterial membranes, proteins and nucleic acids. These systems achieve sterilisation rates of over 99% with low cytotoxicity towards fibroblasts, showing high antibacterial efficacy against *E. coli*, *S. aureus* and *P. gingivalis*, both in the absence and presence of visible light [38]. These systems push towards a new generation of intelligent and selective therapeutic agents.

### 3.4 Versatility of cationic units: ammonium, sulphonium and phosphonium

Recent studies have been conducted comparing the properties of polymers containing ammonium, sulfonium and phosphonium cations highlighting crucial differences. Compounds containing quaternary ammonium have been extensively researched due to their significant antibacterial activity; nonetheless, aromatic derivates pose environmental concerns mainly related to their persistence and toxicity. Polymers containing the imidazolium group, on the other hand, are characterised by greater rigidity and π -π interaction potential with membranes, resulting in a more rigid structure that increases their affinity for bacterial surfaces. Polymers containing the sulfonium group, on the other hand, show less haemolysis and better reactivity compared to their ammonium analogues, attributable to a different electronic distribution, which reduces interaction with eukaryotic membranes. Finally, polymers containing the phosphonium group offer superior chemical stability and a wider therapeutic window. These polymers exhibit enhanced antimicrobial activity compared to QACs, demonstrating increased efficacy against Gram-negative bacteria, hence positioning them as a promising strategy for clinical applications [39,40]. This difference is mainly related to the difference in electronegativity between nitrogen and carbon compared to phosphorus and carbon. This difference affects the electrostatic interactions that occur with bacterial membranes, improving the effectiveness of the polymer. In addition, the chemical stability of phosphonium groups contributes to a longer duration of antimicrobial activity [41]. Another extensively explored class is 1,4 Diazabicyclo[2,2,2]octane (DABCO)-based systems (**Figure 6**), which combine a highly cationic rigid core with excellent thermal and chemical stability.

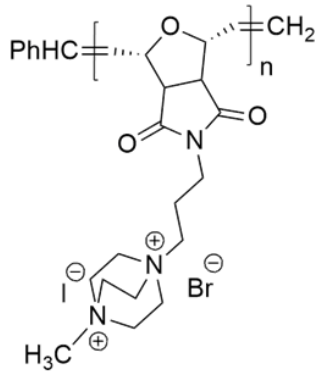

**Figure 6** | General structure of DABCO-based homopolymer [42].

Temur *et al.* conducted studies on these materials and found an effective balance between antimicrobial activity and biocompatibility. Experimental data showed minimal haemolysis and $IC_{50}$ higher than the efficient concentrations. These systems exhibited stability in PBS and physiological solution, without any loss of activity over 28 days. SEM (Scanning Electron Microscope) and TEM (Transmission Electron Microscope) investigation verified that polymer activity induces bacterial membrane degradation through vacuole formation and intracellular content depletion, aligning with a "carpet" mechanism. Furthermore, the results obtained indicate that these polymers are selective, stable and highly promising for biocompatible antimicrobial applications with high activity even against multi-resistant bacteria [42].

### 3.5 Smart surfaces and devices

Cationic polymers are used to coat medical devices, particularly intravascular catheters, orthopaedic implants and implantable cardiovascular systems. The antibacterial contact activity enables the prevention of microbial adherence and biofilm formation on surfaces, hence combating the onset of device-associated illnesses. Moreover, they provide durable coatings due to their structural stability and the possibility of covalent anchoring to surfaces, which minimises the uncontrolled release of the active ingredient, preserving its long-term effectiveness [43].

### 3.6 Antibacterial coatings and biomedical surfaces

Recent research has concentrated on employing cationic polymers as coatings for hospital surfaces and implantable devices as a major preventative technique, functioning either as bactericidal surfaces or anti-adhesion surfaces (**Figure 7**) [44]. Materials functionalised with quaternary ammonium salts, derivatised ammonium or polymeric cationic groups can act as antimicrobial barrier, limiting microbial adhesion and therefore biofilm formation. The strategy most used today exploits the positive charge immobilised on the surface, so that it can interact with the bacterial membrane, generating local destabilisation and leading to the loss of cell integrity. This mechanism is called "contact-active" and is particularly advantageous compared to materials that release antibiotics, as it avoids resistance phenomena associated with the diffusion of bioactive molecules in the microenvironment [45]. Emerging technologies are based on bio-inspired polymers, cationic hydrogels, amphiphilic copolymers and polymeric nanocapsules. Wolf-Brandstetter *et al.* have investigated cationic amphiphilic copolymers capable of adsorbing onto surfaces like titanium, yielding a sustained antimicrobial effect with high biocompatibility. These materials are particularly suitable for applications in prostheses and catheters, as they combine "contact-active" antibacterial activity with compatibility with human cells and reduce the risk of microbial resistance [46]. Zeng *et al.* have developed cationic polymeric nanocapsules. These nanocapsules are based on pyridine quaternary ammonium salts, possess a hollow architecture, high surface charge density, and the ability to exert effective "contact-active" antimicrobial activity against Gram-negative pathogens by breaking down the membrane through electrostatic interaction with anionic phospholipids, eliminating the necessity for cell membrane penetration [47]. Recent research tends to replace contact-active coatings with smart antibacterial materials overcoming static effect with "on-demand" response to physiological stimuli (pH, enzymes, ROS), or by integrating multi-target anti-biofilm strategies, or by combining with advanced nanotechnologies that merge theranostic and antimicrobial functions [48,49]. These innovations could revolutionise the control of medical device-related infections, offering better and more durable solutions. Concurrently, low molecular weight cationic structures, such as quaternary ammonium and phosphonium salts, still represent the simplest and most historically established part of cationic polymers, providing a basic model for comparing structure -activity relationships.

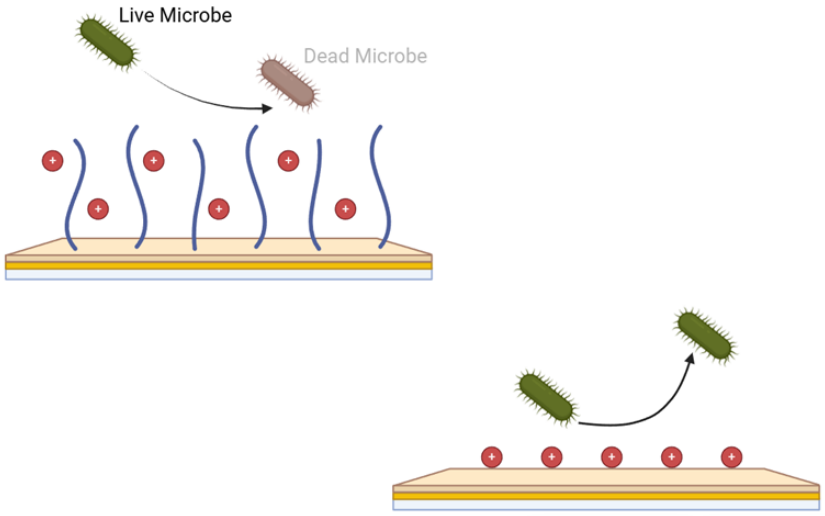


**Figure 7** | Schematic representation of the main mechanisms of action of surfaces functionalised with cationic molecules or cationic polymers. At the top, the bactericidal mechanism; at the bottom, the anti-adhesion mechanism.

### 3.7 Quaternary ammonium and phosphonic salts

Quaternary ammonium salts (QACs) are well-established and versatile classes of compounds used to eredicate bacteria. They were originally employed as disinfectants, antiseptics, and antibacterial agents in industrial and cosmetic contexts. Their antibacterial capacity and activity lie in their simple yet effective mechanism of action. Quaternary ammonium salts interact with bacterial cell membranes thanks to the presence of a permanent cationic structure, which promotes a strong electrostatic bond with negatively charged bacterial surfaces. This interaction is followed by the insertion of the hydrophobic portion of the compound into the phospholipid bilayer, resulting in the the physical-chemical destabilisation of the membrane, the dissipation of membrane electrical potential, concurrent the leakage of intracellular components and, finally, cell lysis. Quaternary ammonium salts differ from traditional antibiotics because in the latter act on specific enzymatic targets or metabolic pathways, while QACs exert a direct mechanical action that reduces the chances of resistance developing in the conventional manner. Despite their advantages, the use of quaternary ammonium salts poses some limitations. Effective antimicrobial properties necessitate a balance between the density of the cationic charge, the hydrophobic portion of the molecule, and the ability to diffuse within the bacterial membrane without damaging eukaryotic cells, hence ensuring adequate selectivity. A further issue lies in the environmental persistence of some compounds and their potential toxicity at elevated concentrations. Thanks to further studies on antimicrobial polymers and ionic liquids, QACs have been re-proposed as adjustable antimicrobials. These molecules allow for minor structural modifications from a basic structure to enhance their properties, including selectivity, stability and biological compatibility [50–52].

### 3.8 Structure-activity: the balance between hydrophobicity and charge

The antibacterial properties of quaternary ammonium salts depend on the structure of the molecule, mainly on the length of the alkyl chain, the nature and number of cationic heads, and the presence of aromatic groups or heterocycles. Recent studies on cationic amphiphilic AIEgens (Aggregaton-Induced Emssion luminogens) by Deng *et al.* have confirmed the importance of these parameters, showing how alkyl chain length and charge density directly influence the antibacterial activity of these compounds and their selectivity towards bacterial cells. The article demonstrates how molecules with intermediate chains (C8-C12) are more effective against Gram-positive bacteria by directly disrupting the cell membrane without involving specific enzymatic targets, while maintaining low cytotoxicity towards human cells. Analyses were conducted using SEM/TEM, Z-potential measurements, membrane depolarisation, and molecular simulations, which demonstrated how these molecules interact directly and optimally with the bacterial phospholipid bilayer, inducing perturbations and disorganisation of the phospholipids themselves. Finally, in vivo results confirmed the efficacy and biocompatibility of these compounds. These results provide an insight for the design of new-generation quaternary ammonium compounds that can also be used as antimicrobial coatings for medical devices [53]. Simultaneously, additional research has demonstrated that in the production of mono- and bi-cationic pyridine compounds (**Figure 8**), the length of the alkyl chains and the presence of bi-cationic units can increase antibacterial activity even against resistant clinical strains and limit biofilm formation [54]. The properties of quaternary ammonium salts are additionally influenced by their conformational structure and self-assembling capabilities. Particularly effective QACs exhibited greater conformational flexibility, attributed to the presence of aromatic rings that allowed π-π interactions with bacterial membranes. On the other hand, self-assembly phenomena in micelles or functional nanostructures increased the density of cationic and hydrophobic units, improving their stability and affinity for the bacterial membrane. These characteristics increase antimicrobial efficacy, selectivity towards bacterial cells and stability in solution [55]. The findings presented above support the concept of a fundamental structure that can be modified and modulated by varying both its chemical composition and structure to design selective, powerful compounds with good biocompatibility.

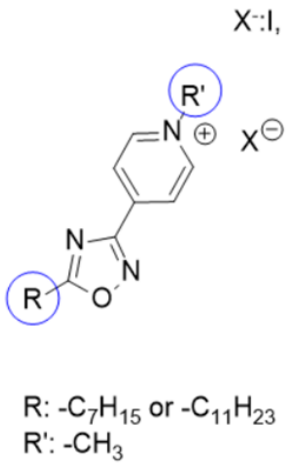


**Figure 8** | General structure of mono-cationic pyridine compound [52].

### 3.9 From chemistry to biomedicine: QACs as smart materials

Recently, the use of quaternary ammonium salts has evolved far beyond their traditional application. These compounds have been incorporated into various advanced platforms to increase their effectiveness, durability and selectivity. Examples of these platforms include functionalised polymers, which combine cationic charges and hydrophobic groups to optimise antibacterial activity and biocompatibility, as well as durable antibacterial coatings for medical devices that can prevent bacterial colonisation and biofilm formation without releasing the active ingredient. Finally, other platforms include nanocapsules for controlled release, which allow the concentration of the QAC released to be modulated, thereby improving antibacterial efficacy and reducing cytotoxicity towards eukaryotic cells [47]. Santoro and Izzo have demonstrated how the covalent anchoring of quaternary ammonium groups to polymeric surfaces allows materials with intrinsic and non-leaching antimicrobial activity to be obtained, which is a fundamental requirement for use in medical devices [56]. Recent experimental research have confirmed the effectiveness of this approach. Surfaces and nanocomposites containing functionalised quaternary ammonium salts have good antimicrobial properties without releasing the active ingredient and are also capable of reducing biofilm formation and bacterial colonisation on implantable substrates [57]. Other systems are based on DABCO, which fall into the category of cationic antimicrobial materials. Temur *et al.* demonstrated that cationic polymers derived from DABCO are active against multi-resistant strains, have good thermal and chemical stability, and a very low haemolysis profile. These polymers are obtained by ROMP (Ring Opening Metathesis Polymerisation), with different molecular lengths [42]. These results therefore confirm that the design of cationic molecules with defined structures represents a way to generate bacterial agents.

### 3.10 Emerging resistance and environmental impact

The extensive use of quaternary ammonium salts, especially during the SARS-CoV-2 pandemic, has heightened selective pressure on pathogens, causing the emergence of strains tolerant to these biocides. Kuznetsova *et al.* have reported in their studies that nosocomial bacteria such as *E. coli*, *K. pneumoniae*, *P. aeruginosa* and *S. aureus* already show reduced sensitivity to chlorhexidine and benzalkonium chloride-based disinfectants, alongside a significant prevalence of genes associated with efflux pump transduction. These bacteria employ adaptive strategies such as membrane remodelling or the formation of structured biofilms capable of circumventing the activities of these biocides [58]. These mechanisms, frequently concomitant with the onset of antibiotic resistance, indicate that disproportionate use of QACs can also contribute to the spread of multi-resistant bacteria. Besides the problems related with the emergence of antibiotic resistance, another concern relates to the negative environmental impact of excessive use of quaternary ammonium salts. A monitoring research was conducted in three German rivers revealed an increase in quaternary ammonium salts in sediments during and after the pandemic, with concentrations exceeding the ecotoxicological no-effect thresholds for long-chain compounds prior to 2020 [59]. This has raised concerns about the chronic effects they will have on aquatic ecosystems, as incomplete removal in treatment plants contributes to their large-scale accumulation.

### 3.10 Posphonium salts (QPSs): a more sustainable alternative

In light of these issues, research is shifting towards the discovery of new compounds. Alfei *et al.* studied phosphonium salt compounds [60], (**Figure 9**) these are quaternary compounds comprising triphenylalkylphosphonium derivatives. These compounds have shown promising properties against biofilm proliferation in vitro, greater chemical stability than QACs, and a wider therapeutic window. The modulation of QPS synthesis, which is simple and versatile, is aimed at obtaining compounds that can develop less resistance. Phosphonium salts constitute a significant approach for addressing chronic infections, also associated with medical devices that are consequential to the colonisation of multi-resistant biofilm -producing bacteria; moreover, they exhibit reduced environmental persistence, thereby mitigating he ecotoxicological risks associated with QACs [61]. Innovative approaches are implemented to obtain more degradable molecules that exhibit less environmental persistence and possess targeted and modifiable activity over time. Thus, the evolution and future research of quaternary ammonium salts cannot be exempt from a risk assessment including antimicrobial resistance, ecotoxicity and sustainability in applications. Future research should focus on harmonizing chemical innovation with environmental sustainability to develop compounds that effectively combat microbes while minimizing ecological damage. One of the main objectives is to limit the indiscriminate use of quaternary ammonium salts, thus avoiding selective pressures that favour the onset of resistance, and to develop hybrid and synergistic systems combining both QACs and QPSs with polymers, peptides or other antimicrobial molecules to increase efficacy at reduced dosages. Finally, integrating nanotechnological strategies using nanoparticles or functionalised coatings that optimise the release and penetration of molecules within biofilms. The challenge will be to balance the antimicrobial potency, safety and sustainability of these compounds; however, further studies are needed to achieve therapeutic efficiency while minimising environmental and clinical costs. **Table 1** illustrates the structure-activity relationships of the compounds discussed above. The correlation is based on characteristics such as charge density, hydrophobicity and molecular topology, and can be extended to other complex amphiphilic systems such as gemini and catanionic compounds, which will be discussed in the next section.

## 4. Gemini surfactants and catanionic systems

### 4.1 Gemini surfactants

Gemini surfactants are compounds characterised by the presence of two polar cationic heads and two hydrophobic chains connected by a spacer that is modular and confers more favourable chemical-physical properties, including greater surface efficiency and enhanced antimicrobial activity. These structures represent an

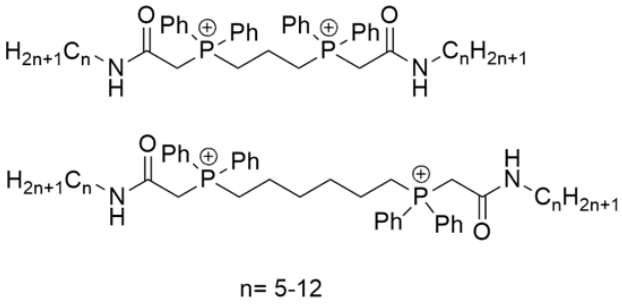


**Figure 9** | General structure of phosphonium salt compounds [59].

**Table 1** | Structure–activity relationship (SAR) trends of cationic systems.

| Parameter | Structural variable (from examples in text) | Effect on antimicrobial activity | Effect on cytotoxicity | Qualitative trend (as described) |
|---|---|---|---|---|
| **Cationic charge density** | Number and type of charged groups (ammonium, imidazolium, pyridinium) | Increases binding to bacterial membranes and killing efficiency | Excessive charge density increases haemolysis and toxicity | Optimal balance between electrostatic attraction and selectivity is required |
| **Hydrophobicity** | Alkyl chain length, aromatic substituents, backbone rigidity | Enhances membrane insertion and biofilm penetration | High hydrophobicity reduces selectivity and solubility | Moderate amphiphilicity gives best antimicrobial-toxicity balance |
| **Molecular topology** | Linear vs. branched vs. star-shaped architectures | Multivalent interactions increase surface coverage and activity | Branched or dense systems may reduce biocompatibility | Topology tuning can improve selectivity and membrane affinity |
| **Spacer length (gemini surfactants)** | Number of methylene units connecting cationic heads | Affects membrane insertion and CMC; moderate length improves synergy | Long spacers increase lipophilicity and cytotoxicity | 6–8 carbons often give optimal efficiency/toxicity ratio |

evolution from conventional cationic surfactants. The modularity of these compounds lies in the ability to make structural changes in terms of the nature or length of the hydrophobic unit and the spacer. These changes optimise the interaction of these compounds with biological membranes. Numerous cationic Gemini systems based on quaternary ammonium (**Figure 10**), pyridinium, imidazolium and amide structures have been developed, increasing and broadening the spectrum of activities and versatility compared to traditional monocationic surfactants [17]. These structures have a lower CMC (critical micelle concentration) than their monocationic analogues. Recent studies have confirmed that this characteristic promotes antibacterial activity. For example, Gemini with optimised chain lengths show both efficient micellisation at low concentrations and reduced MICs against Gram-positive and Gram-negative bacteria [62,63]. However, it should be emphasised that the reduction in CMC is not the only indicator of the antimicrobial efficacy of these compounds. Additional considerations, as previously noted, include the length of the hydrophobic chain, the nature of the spacer and the presence of heterocyclic functionalities. The spacer, a structural component linking the two cationic heads, plays a crucial role in the design of Gemini surfactants. The choice of one spacer over another modulates the conformational flexibility of the molecule, the charge density and electrostatic interaction with bacterial phospholipids, membrane penetration and disorganisation, as well as selectivity for eukaryotic cells. Studies by Bao *et al.* indicates that an aliphatic spacer of intermediate length achieves the best compromise between antimicrobial activity and biosafety; specifically, heterocyclic Gemini with dodecyl chains and short spacers show high antibacterial activity against *S. aureus* (up to ~100% inhibition), enhanced surfactant properties with diminished surface tension, lower micellisation concentration, and adequate biocompatibility for both medical and industrial applications. These results highlight the predominant role of the spacer within these compounds, as it can increase their antimicrobial efficacy while reducing undesirable effects. Finally, the introduction of aromatic units can enhance their action thanks to π-π interaction with lipid and protein components [64]. Gemini surfactants are employed in diverse sophisticated biological applications thanks to their self-assembling properties and ability to modulate their amphiphilic qualities. Their bicationic structure allows synergistic interaction with biological membranes, enhancing the eradication of resistant biofilms and the development of highly adhesive antibacterial coatings, beneficial in medical devices and hospital surfaces [65]. Thanks to their self-assembling properties in micelles, vesicles or nanocapsules, they serve as excellent carriers for anti-cancer drugs, increasing their availability and selectivity towards neoplastic cells. Recent studies have shown that nanoparticles formulated with Gemini surfactants, encapsulating curcumin and tamoxifen, can significantly improve selective cytotoxicity towards breast cancer cells [66]. He *et al.* have recently developed peptides conjugated to quaternary ammonium Gemini moieties. These structures are capable of self-assembling into cationic nanoparticles with good antimicrobial activity and low cytotoxicity. Antimicrobial efficiency relies on a multimodal mechanism of action that includes both the physical disruption of the bacterial membrane and the suppression of ribosomal protein synthesis, ensuring high efficacy even against multi-resistant strains. Furthermore, these nanomaterials have demonstrated activity in vivo, preventing systemic skin infections and surpassing the efficacy of vancomycin, thus highlighting the potential of these Gemini-based peptides [67]. Hafidi *et al.* studied and developed systems consisting of arginine-based Gemini surfactants (**Figure 11**). These compounds consisted of two cationic arginine heads connected to two hydrophobic chains of different lengths, and they showed strong antimicrobial activity against clinically relevant bacteria and fungi. They also demonstrated the ability to eradicate mature biofilms of MRSA, *C. albicans* and *C. tropicalis* at low concentrations. Their efficacy is dictated by their hydrophobic content, while their physiologically compatible cationic structure ensures low cytotoxicity and reduced hemolysis, making them promising for pharmacological applications [68].

### 4.2. Catanionic systems: synergy and reduced toxicity

Other systems combine a cationic and an anionic surfactant. This combination results in supramolecular aggregates with adjustable charge; through structural variations, their affinity for bacterial membranes can be modulated, thereby improving their selectivity, reducing cytotoxicity and increasing stability in physiological

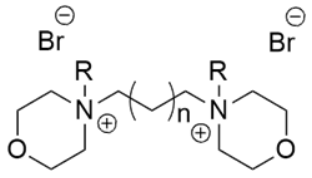


**Figure 10** | Example of structure of cationic Gemini compound based on quaternary ammonium [15].

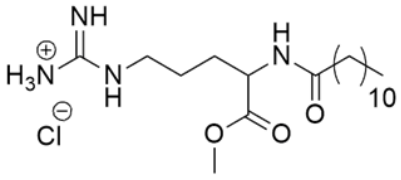


**Figure 11** | Structure of arginine-based surfactants [66].

fluids. Studies have been conducted on the influence of variations in the cationic/anionic ratio on antimicrobial efficacy. Investigations conducted on cationic vesicles with arginine-based surfactants have demonstrated that these modifications significantly influence surface charge, aggregation, and toxicity, while maintaining good antimicrobial efficacy [69]. Kowalczyk *et al.* conducted studies on mixtures of monomeric cationic surfactants and Gemini/dimer surfactants with varying molar ratios of the cationic to the anionic portion. The results indicated that minor increments of anionic surfactant effectively preserve the antibacterial activity of these systems [70]. Furthermore, these systems can also be used for the delivery of bioactive molecules [71]; for example, they can be adapted for anti-tumor applications, through drug delivery, or for environmental sensing systems, exploiting their ability to incorporate functional molecules that are able to respond to specific environmental stimuli. Surfactants have demonstrated significant capabilities in combining antibacterial efficacy, biological safety and multifunctionality, opening innovative opportunities for the design and further investigation of these substances.

### 4.3. Biodegradability and sustainability

To overcome the environmental problems caused by the excessive use of quaternary ammonium salts, recent research is also focusing on the sustainability of these compounds. Research is being conducted on the redesign of surfactants in accordance with the principles of green chemistry. New synthesis strategies aim to introduce biodegradable hydrophobic chains that decompose swiftly without environmental accumulation, integrate cationic heads inspired by natural amino acids (such as histidine, arginine or tryptophan) to improve biological compatibility, and use clean, low-environmental-impact synthesis methods, reducing the use of toxic solvents. For example, recent studies conducted on histidine-based cationic surfactants have shown excellent biodegradability and low cytotoxicity of these compounds, making them promising for pharmaceutical applications while also being sustainable [72]. The characteristics of surface efficiency, self-assembling capacity and structural versatility make these Gemini and catanionic systems one of the most promising classes in the antimicrobial field.

## 5. Applications and perspectives

The significant versatility of cationic organic compounds allows their application in several fields where both antibacterial characteristics and surfactant properties are required. These substances have been studied in surface antibacterial coatings to prevent the aggregation of bacterial colonies for the formation of biofilms and also for the development of new macromolecules that have higher biological tolerability and a lower capacity to develop resistance. Their characteristics and properties are based on the mechanisms mentioned above and are influenced by positive charge density, structure and hydrophobicity. These parameters regulate the interactions of these compounds with microbial membranes. **Table 2** provides an overview of the main applications and current research directions and summarizes the representative systems described in this review, together with the type of application or surface, their antimicrobial mechanism and the main observations or limitations highlighted in recent studies. Current research focuses on increasing specificity of action and reducing toxicity to host cells, as well as developing more sustainable and biodegradable formulations. Future activities should continue to integrate microbial efficacy with environmental and biological compatibility, while enabling practical and safe applications of these cationic materials in medical and industrial contexts.

### 5.1 Sustainability perspective

From a sustainability standpont, the rational design of novel cationic antimicrobial systems should prioritize environmental safety alongside antimicrobial activity. Essential design principles include the development of biodegradable or cleavable cationic strcutures, the reduction of long-term environmental persistence, and the modulation of charge density and hydrophobicity to minimize ecotoxicity while maintaining activity [73]. The use of renewable or bio-based building blocks, as well as stimuli-responsive or degradable formulations that limit unnecessary release, represents an additional strategy to minimize environmental impact [74,75]. Integrating life-cycle considerations at the early phases of material design will be essential to ensure effective, safe, and sustainable cationic antimicrobial systems for widespread medical and industrial applications.

## Concluding Remarks

The spread of antibiotic-resistant strains is one of the global health emergencies that poses a serious threat to our society. The use of cationic compounds such as antimicrobial peptides, cationic polymers, quaternary ammonium salts and Gemini surfactants represents innovative therapeutic strategies that can offer significant help in combating and curbing this threat. Their physical mechanism of action, which targets bacterial membranes, is advantageous compared to that of traditional antibiotics, as it presents a reduced likelihood of resistance development. Among these systems, cationic polymers and QACs stand out for their structural tunability and synthetic scalability, making them particularly suitable for industrial translation, including antimicrobial coating, medical device surfaces, and water-treatment technologies. Their adaptability in hydrophilic/lipophilic balance enables optimization for selectivity and cytotoxicity, facilitating compliance with regulatory requirement for biomedical and consumer application. Gemini surfactants, thanks to their bicationic structure, achieve high efficacy at low concentrations, represent attractive candidates for biofilm-resistant material, advanced surface treatments, and long-lasting antimicrobial coating. Their efficiency at reduced dosages is especially relevant from both toxicological and sustainability perspectives, supporting potential large-scale development. Antimicrobial peptides remain highly promising due to their broad-spectrum activity and functional versatility, particularly for clinical and therapeutic applications. However, challenges related to stability, cost-effective synthesis, and regulatory approval remain key barriers that must be

**Table 2** | Representative applications and perspectives of cationic organic systems, summarizing the main functional categories, mechanisms, and remarks on performance.

| Application / Focus Area | Example Systems (mentioned in the review) | Mechanism / Functionality | Performance Notes / Perspectives |
|---|---|---|---|
| Antibacterial coatings | Cationic polymers; QACs; DABCO-based | Contact-active antibacterial action through electrostatic interaction | Reduction of E. coli and S. aureus adhesion; suitable for medical devices; minimal leaching |
| Biofilm inhibition / prevention of adhesion | Polyimidazolium polymers; cationic copolymers; pyridinium-based nanocapsules | Membrane destabilisation or electrostatic repulsion | Active against resistant strains; some systems disrupt early-stage biofilms |
| Nanostructure delivery systems | Self-assembling cationic polymers, nanoparticles carriers with AMPs | Enhanced penetration into biofilms; controlled release; | Lower MIC values than free agents; improved biocompatibility |
| Gemini surfactants and catanionic systems | Gemini ammonium/ pyridinium, amphiphilic surfactants | Dual-head cationic interaction with membranes; self-assembly into micelles/ vesicles | High antibacterial and antibiofilm efficiency; good selectivity and tunability; |
| Cationic peptides and peptide mimics | Natural AMPs; bis-pyridyl AMP mimetics; AMP-functionalized surfaces | Membrane disruption, intracellular targeting, ROS induction, multimodal action | High selectivity; activity against MDR bacteria and persisters; limitations: stability and synthesis costs |
| Sustainability-oriented and next-generation materials | Biodegradable cationic polymers; quaternary phosphonium salts (QPSs) | Membranolytic action with less environmental impact | Greater biocompatibility, reduced toxicity, alternatives to QACs |

addressed before widespread clinical adoption. To facilitate the transition to the clinical application of these compounds toward real-word applications, future research should focus on studying possible solutions to increase biocompatibility and reduce systemic toxicity. Defining structure-activity relationships will guide the synthesis of new compounds, thoroughly evaluating the field of environmental persistence and degradation by-products. Developing smart formulations with modulable and multifunctional activities and conducting standardized and comparable preclinical and clinical tests will be achieved as final goals. Equal attention should be devoted to environmental persistence, biodegradability, and degradation by-products, especially for materials intended for long-term or large-scale use. Thanks to the integration of knowledge from various fields such as chemistry, biology, nanotechnology and materials engineering, cationic molecules could truly represent promising platforms for therapeutic innovation in the treatment of infections and constitute an effective weapon against bacterial resistance.

## Acknowledgements

University of Palermo is acknowledged for financial support.

## References

[1] "Jim O'Neill, Antimicrobial Resistance: Tackling a Crisis for the Health and Wealth of Nations; Review on Antimicrobial Resistance. 2014."

[2] P. Dadgostar, "Antimicrobial Resistance: Implications and Costs," IDR, vol. Volume 12, pp. 3903–3910, Dec. 2019, doi: 10.2147/IDR.S234610.

[3] J. M. A. Blair, M. A. Webber, A. J. Baylay, D. O. Ogbolu, and L. J. V. Piddock, "Molecular mechanisms of antibiotic resistance," Nat Rev Microbiol, vol. 13, no. 1, pp. 42–51, Jan. 2015, doi: 10.1038/nrmicro3380.

[4] J. L. Martinez and F. Baquero, "Mutation Frequencies and

Antibiotic Resistance," Antimicrob Agents Chemother, vol. 44, no. 7, pp. 1771–1777, July 2000, doi: 10.1128/AAC.44.7.1771-1777.2000.

[5] S. A. Kraemer, A. Ramachandran, and G. G. Perron, "Antibiotic Pollution in the Environment: From Microbial Ecology to Public Policy," Microorganisms, vol. 7, no. 6, p. 180, June 2019, doi: 10.3390/microorganisms7060180.

[6] K. Zhang, X. Li, C. Yu, and Y. Wang, "Promising Therapeutic Strategies Against Microbial Biofilm Challenges," Front. Cell. Infect. Microbiol., vol. 10, p. 359, July 2020, doi: 10.3389/fcimb.2020.00359.

[7] C. Tascini et al., "The role of biofilm forming on mortality in patients with candidemia: a study derived from real world data," Infectious Diseases, vol. 50, no. 3, pp. 214–219, 2018, doi: 10.1080/23744235.2017.1384956.

[8] C. Zhou and Y. Wang, "Structure–activity relationship of cationic surfactants as antimicrobial agents," Current Opinion in Colloid & Interface Science, vol. 45, pp. 28–43, Feb. 2020, doi: 10.1016/j.cocis.2019.11.009.

[9] Z. Yu et al., "Cationic antibacterial polymers for development of bactericidal materials: Strategies, mechanisms, and applications," Advances in Colloid and Interface Science, vol. 346, p. 103658, Dec. 2025, doi: 10.1016/j.cis.2025.103658.

[10] R. E. W. Hancock and H.-G. Sahl, "Antimicrobial and host-defense peptides as new anti-infective therapeutic strategies," Nat Biotechnol, vol. 24, no. 12, pp. 1551–1557, Dec. 2006, doi: 10.1038/nbt1267.

[11] Z. Yu et al., "Cationic antibacterial polymers for development of bactericidal materials: Strategies, mechanisms, and applications," Advances in Colloid and Interface Science, vol. 346, p. 103658, Dec. 2025, doi: 10.1016/j.cis.2025.103658.

[12] J. Fedorowicz and J. Sączewski, "Advances in the Synthesis of Biologically Active Quaternary Ammonium Compounds," IJMS, vol. 25, no. 9, p. 4649, Apr. 2024, doi: 10.3390/ijms25094649.

[13] M. N. Nadagouda et al., "Antimicrobial activity of quaternary ammonium salts: structure-activity relationship," Med Chem Res, vol. 31, no. 10, pp. 1663–1678, Oct. 2022, doi: 10.1007/s00044-022-02924-9.

[14] H. Javadi, A. Lehnen, and M. Hartlieb, "Bioinspired Cationic Antimicrobial Polymers," Angew Chem Int Ed, vol. 64, no. 24, p. e202503738, June 2025, doi: 10.1002/anie.202503738.

[15] Q. Zhang, "Antimicrobial peptides: from discovery to developmental applications," Appl Environ Microbiol, vol. 91, no. 4, pp. e02115-24, Apr. 2025, doi: 10.1128/aem.02115-24.

[16] M. Del Olmo and C. Andreu, "Current Status of the Application of Antimicrobial Peptides and Their Conjugated Derivatives," Molecules, vol. 30, no. 15, p. 3070, July 2025, doi: 10.3390/molecules30153070.

[17] Y. Gyani Devi, A. Koya Pulikkal, and J. Gurung, "Research Progress on the Synthesis of Different Types of Gemini Surfactants with a Functionalized Hydrophobic Moiety and Spacer," ChemistrySelect, vol. 7, no. 45, p. e202203485, Dec. 2022, doi: 10.1002/slct.202203485.

[18] A. Moretta et al., "Antimicrobial Peptides: A New Hope in Biomedical and Pharmaceutical Fields," Front. Cell. Infect. Microbiol., vol. 11, p. 668632, June 2021, doi: 10.3389/fcimb.2021.668632.

[19] R. I. Lehrer and T. Ganz, "Antimicrobial peptides in mammalian and insect host defence," Current Opinion in Immunology, vol. 11, no. 1, pp. 23–27, Feb. 1999, doi: 10.1016/S0952-7915(99)80005-3.

[20] K. V. R. Reddy, R. D. Yedery, and C. Aranha, "Antimicrobial peptides: premises and promises," International Journal of Antimicrobial Agents, vol. 24, no. 6, pp. 536–547, Dec. 2004, doi: 10.1016/j.ijantimicag.2004.09.005.

[21] W. Liang and J. Diana, "The Dual Role of Antimicrobial Peptides in Autoimmunity," Front. Immunol., vol. 11, p. 2077, Sept. 2020, doi: 10.3389/fimmu.2020.02077.

[22] X. Li, S. Zuo, B. Wang, K. Zhang, and Y. Wang, "Antimicrobial Mechanisms and Clinical Application Prospects of Antimicrobial Peptides," Molecules, vol. 27, no. 9, p. 2675, Apr. 2022, doi: 10.3390/molecules27092675.

[23] V. V. S. K. Pushadapu, P. S. Babu, S. Danaboina, Z. Qamar, S. A. Khan, and J. Ali, "Antimicrobial Peptides as Biomacromolecular Therapeutics against Antimicrobial Resistance: Structural Insights and Mechanistic Advances," Int J Pept Res Ther, vol. 31, no. 5, p. 81, July 2025, doi: 10.1007/s10989-025-10744-9.

[24] K. H. Min, K. H. Kim, M.-R. Ki, and S. P. Pack, "Antimicrobial Peptides and Their Biomedical Applications: A Review," Antibiotics, vol. 13, no. 9, p. 794, Aug. 2024, doi: 10.3390/antibiotics13090794.

[25] W. V. T. Hof, E. C. I. Veerman, E. J. Helmerhorst, and A. V. N. Amerongen, "Antimicrobial Peptides: Properties and Applicability," Biological Chemistry, vol. 382, no. 4, Jan. 2001, doi: 10.1515/BC.2001.072.

[26] A. Giuliani and A. C. Rinaldi, "Beyond natural antimicrobial peptides: multimeric peptides and other peptidomimetic approaches," Cell. Mol. Life Sci., vol. 68, no. 13, pp. 2255–2266, July 2011, doi: 10.1007/s00018-011-0717-3.

[27] L. Liu, X. Cui, H. Zhang, J. Yao, L. Li, and Y. Cai, "Optimized strategies for designing antimicrobial peptides targeting multidrug-resistant Gram-negative bacteria," Biomedicine & Pharmacotherapy, vol. 189, p. 118264, Aug. 2025, doi: 10.1016/j.biopha.2025.118264.

[28] Y. Li et al., "Design, synthesis and antibacterial evaluation of bis-pyridinium cationic antimicrobial peptide mimics with low hemolytic toxicity," European Journal of Medicinal Chemistry, vol. 299, p. 118012, Dec. 2025, doi: 10.1016/j.ejmech.2025.118012.

[29] M. Ali et al., "Physical and Functional Characterization of PLGA Nanoparticles Containing the Antimicrobial Peptide SAAP-148," IJMS, vol. 24, no. 3, p. 2867, Feb. 2023, doi: 10.3390/ijms24032867.

[30] Y. Pan et al., "Antimicrobial peptide-antibiotic synergy exerts anti-streptococcus suis infection by membrane disruption, ROS induction and biofilm inhibition," International Immunopharmacology, vol. 161, p. 115053, Aug. 2025, doi: 10.1016/j.intimp.2025.115053.

[31] M. Nicolas et al., "Strategies for Antimicrobial Peptides Immobilization on Surfaces to Prevent Biofilm Growth on Biomedical Devices," Antibiotics, vol. 11, no. 1, p. 13, Dec. 2021, doi: 10.3390/antibiotics11010013.

[32] Y. Yang, Z. Cai, Z. Huang, X. Tang, and X. Zhang, "Antimicrobial cationic polymers: from structural design to functional control," Polym J, vol. 50, no. 1, pp. 33–44, Jan. 2018, doi: 10.1038/pj.2017.72.

[33] A. Tyagi and A. Mishra, "Optimal Balance of Hydrophobic Content and Degree of Polymerization Results in a Potent Membrane-Targeting Antibacterial Polymer," ACS Omega, vol. 6, no. 50, pp. 34724–34735, Dec. 2021, doi: 10.1021/acsomega.1c05148.

[34] S. Laroque, K. E. S. Locock, and S. Perrier, "Cationic Star Polymers Obtained by the Arm-First Approach Influence of Arm Number and Positioning of Cationic Units on Antimicrobial Activity," Biomacromolecules, vol. 26, no. 1, pp. 190–200, Jan. 2025, doi: 10.1021/acs.biomac.4c00882.

[35] C. Liu et al., "Imidazolium-Based Main-Chain Copolymers With Alternating Sequences for Broad-Spectrum Bactericidal Activity and Eradication of Bacterial Biofilms," Macromolecular Bioscience, vol. 24, no. 5, p. 2300489, May 2024, doi: 10.1002/mabi.202300489.

[36] W. Zhong et al., "Designer broad-spectrum polyimidazolium antibiotics," Proc. Natl. Acad. Sci. U.S.A., vol. 117, no. 49, pp. 31376–31385, Dec. 2020, doi: 10.1073/pnas.2011024117.

[37] A. Nabawy et al., "Cationic conjugated polymers with tunable hydrophobicity for efficient treatment of multidrug-resistant wound biofilm infections," Biomaterials, vol. 316, p. 123015, May 2025, doi: 10.1016/j.biomaterials.2024.123015.

[38] B. Ma, X. Lin, T. Zhu, X. Zheng, and J. Zhu, "Enhanced antimicrobial performance of D-A covalent organic framework with pyridinium and quaternary ammonium groups and ROS activity," Surfaces and Interfaces, vol. 62, p. 106226, Apr. 2025, doi: 10.1016/j.surfin.2025.106226.

[39] H. Akram et al., "A convergence of synthesis and antimicrobial research: imidazolium based dicationic ionic liquids," BMC Chemistry, vol. 19, no. 1, p. 220, July 2025, doi: 10.1186/s13065-025-01574-3.

[40] Y. Gong et al., "Ammonium, Phosphonium, and Sulfonium Polymers for Antimicrobial Applications: A Comparative Study," ACS Appl. Polym. Mater., vol. 6, no. 12, pp. 6966–6975, June 2024, doi: 10.1021/acsapm.4c00461.

[41] Y. Xue, H. Xiao, and Y. Zhang, "Antimicrobial Polymeric Materials with Quaternary Ammonium and Phosphonium Salts," IJMS, vol. 16, no. 2, pp. 3626–3655, Feb. 2015, doi: 10.3390/ijms16023626.

[42] B. Z. Temur et al., "New Generation Antibiotics Derived from DABCO-Based Cationic Polymers," Antibiotics, vol. 14, no. 9, p. 856, Aug. 2025, doi: 10.3390/antibiotics14090856.

[43] H. Qiu et al., "The Mechanisms and the Applications of Antibacterial Polymers in Surface Modification on Medical Devices," Front. Bioeng. Biotechnol., vol. 8, p. 910, Nov. 2020, doi: 10.3389/fbioe.2020.00910.

[44] G. C. Lainioti and D. Druvari, "Designing Antibacterial-Based Quaternary Ammonium Coatings (Surfaces) or Films for Biomedical Applications: Recent Advances," IJMS, vol. 25, no. 22, p. 12264, Nov. 2024, doi: 10.3390/ijms252212264.

[45] P. Elena and K. Miri, "Formation of contact active antimicrobial surfaces by covalent grafting of quaternary ammonium compounds," Colloids and Surfaces B: Biointerfaces, vol. 169, pp. 195–205, Sept. 2018, doi: 10.1016/j.colsurfb.2018.04.065.

[46] C. Wolf-Brandstetter, R. Methling, and D. Kuckling, "Adsorbable and Antimicrobial Amphiphilic Block Copolymers with Enhanced Biocompatibility," Macro Materials & Eng, vol. 310, no. 8, p. 2500078, Aug. 2025, doi: 10.1002/mame.202500078.

[47] M. Zeng et al., "Constructing antibacterial polymer nanocapsules based on pyridine quaternary ammonium salt," Materials Science and Engineering: C, vol. 108, p. 110383, Mar. 2020, doi: 10.1016/j.msec.2019.110383.

[48] M. A. Cassa, P. Gentile, J. Girón-Hernández, G. Ciardelli, and I. Carmagnola, "Smart self-defensive coatings with bacteria-triggered antimicrobial response for medical devices," Biomater. Sci., vol. 12, no. 21, pp. 5433–5449, 2024, doi: 10.1039/D4BM00936C.

[49] Y. Xie, H. Liu, Z. Teng, J. Ma, and G. Liu, "Nanomaterial-enabled anti-biofilm strategies: new opportunities for treatment of bacterial infections," Nanoscale, vol. 17, no. 10, pp. 5605–5628, 2025, doi: 10.1039/D4NR04774E.

[50] M. N. Nadagouda et al., "Antimicrobial activity of quaternary ammonium salts: structure-activity relationship," Med Chem Res, vol. 31, no. 10, pp. 1663–1678, Oct. 2022, doi: 10.1007/s00044-022-02924-9.

[51] W. A. Arnold et al., "Quaternary Ammonium Compounds: A Chemical Class of Emerging Concern," Environ. Sci. Technol., vol. 57, no. 20, pp. 7645–7665, May 2023, doi: 10.1021/acs.est.2c08244.

[52] A. N. Vereshchagin, N. A. Frolov, K. S. Egorova, M. M. Seitkalieva, and V. P. Ananikov, "Quaternary Ammonium Compounds (QACs) and Ionic Liquids (ILs) as Biocides: From Simple Antiseptics to Tunable Antimicrobials," IJMS, vol. 22, no. 13, p. 6793, June 2021, doi: 10.3390/ijms22136793.

[53] Z. Deng et al., "Unveiling the Role of Alkyl Chain in Boosting Antibacterial Selectivity and Cell Biocompatibility," JACS Au, vol. 5, no. 2, pp. 675–683, Feb. 2025, doi: 10.1021/jacsau.4c00915.

[54] S. Amata et al., "Synthesis and Antibacterial Activity of Mono- and Bi-Cationic Pyridinium 1,2,4-Oxadiazoles and Triazoles," IJMS, vol. 25, no. 1, p. 377, Dec. 2023, doi: 10.3390/ijms25010377.

[55] B. Sharma, L. Pérez-García, G. R. Chaudhary, and G. Kaur, "Innovative approaches to cationic and anionic (catanionic) amphiphiles self-assemblies: Synthesis, properties, and industrial applications," Advances in Colloid and Interface Science, vol. 337, p. 103380, Mar. 2025, doi: 10.1016/j.cis.2024.103380.

[56] O. Santoro and L. Izzo, "Antimicrobial Polymer Surfaces Containing Quaternary Ammonium Centers (QACs): Synthesis and Mechanism of Action," IJMS, vol. 25, no. 14, p. 7587, July 2024, doi: 10.3390/ijms25147587.

[57] E. Weiss et al., "Quaternary Ammonium Silica Nanoparticles for Antimicrobial Implantable Medical Devices: An In Vitro Study," Life, vol. 14, no. 12, p. 1654, Dec. 2024, doi: 10.3390/life14121654.

[58] M. V. Kuznetsova et al., "Nosocomial Escherichia coli, Klebsiella pneumoniae, Pseudomonas aeruginosa, and Staphylococcus aureus: Sensitivity to Chlorhexidine-Based Biocides and Prevalence of Efflux Pump Genes," IJMS, vol. 26, no. 1, p. 355, Jan. 2025, doi: 10.3390/ijms26010355.

[59] S. Lennartz et al., "Downstream effects of the pandemic? Spatiotemporal trends of quaternary ammonium compounds in suspended particulate matter of German rivers," Journal of Hazardous Materials, vol. 480, p. 136237, Dec. 2024, doi: 10.1016/j.jhazmat.2024.136237.

[60] S. Alfei, "Shifting from Ammonium to Phosphonium Salts: A Promising Strategy to Develop Next-Generation Weapons against Biofilms," Pharmaceutics, vol. 16, no. 1, p. 80, Jan. 2024, doi: 10.3390/pharmaceutics16010080.

[61] S. R. Brayton et al., "Soft QPCs: Biscationic Quaternary Phosphonium Compounds as Soft Antimicrobial Agents," ACS Infect. Dis., vol. 9, no. 4, pp. 943–951, Apr. 2023, doi: 10.1021/acsinfecdis.2c00624.

[62] K. A. Mechken, M. Menouar, Z. Talbi, S. Saidi-Besbes, and M. Belkhodja, "Self-assembly and antimicrobial activity of cationic gemini surfactants containing triazole moieties," RSC Adv., vol. 14, no. 27, pp. 19185–19196, 2024, doi: 10.1039/D4RA02177K.

[63] I. Kowalczyk, A. Szulc, A. Koziróg, A. Komasa, and B. Brycki, "Surface and Antimicrobial Properties of Ester-Based Gemini Surfactants," Molecules, vol. 30, no. 12, p. 2648, June 2025, doi: 10.3390/molecules30122648.

[64] Y. Bao, L. Gao, F. Wang, and J. Ma, "Heterocyclic cationic Gemini surfactants for efficient antibacterial, dispersion and fixation," Process Safety and Environmental Protection, vol. 159, pp. 168–177, Mar. 2022, doi: 10.1016/j.psep.2021.12.058.

[65] Y. Gyani Devi, A. Koya Pulikkal, and J. Gurung, "Research Progress on the Synthesis of Different Types of Gemini Surfactants with a Functionalized Hydrophobic Moiety and Spacer," ChemistrySelect, vol. 7, no. 45, p. e202203485, Dec. 2022, doi: 10.1002/slct.202203485.

[66] Z. F. Ashin et al., "Synergistic effect of curcumin and tamoxifen loaded in pH-responsive gemini surfactant nanoparticles on breast cancer cells," BMC Complement Med Ther, vol. 24, no. 1, p. 337, Sept. 2024, doi: 10.1186/s12906-024-04631-x.

[67] Y. He et al., "Enhancing Antibiotic-Resistant Bacterial Infection Therapy: Self-Assembling Gemini Quaternary Ammonium-Functionalized Peptide Nanoassemblies with Multiple Antibacterial Mechanisms," ACS Nano, vol. 19, no. 7, pp. 6977–6992, Feb. 2025, doi: 10.1021/acsnano.4c14689.

[68] Z. Hafidi, M. T. García, S. Vazquez, M. Martinavarro-Mateos, A. Ramos, and L. Pérez, "Antimicrobial and biofilm-eradicating properties of simple double-chain arginine-based surfactants," Colloids and Surfaces B: Biointerfaces, vol. 253, p. 114762, Sept. 2025, doi: 10.1016/j.colsurfb.2025.114762.

[69] A. Pinazo, R. Pons, A. Marqués, M. Farfan, A. Da Silva, and L. Perez, "Biocompatible Catanionic Vesicles from Arginine-Based

Surfactants: A New Strategy to Tune the Antimicrobial Activity and Cytotoxicity of Vesicular Systems," Pharmaceutics, vol. 12, no. 9, p. 857, Sept. 2020, doi: 10.3390/pharmaceutics12090857.

[70] I. Kowalczyk, A. Koziróg, A. Szulc, A. Komasa, and B. Brycki, "Antimicrobial Properties of Monomeric and Dimeric Catanionic Surfactant System," Molecules, vol. 30, no. 1, p. 164, Jan. 2025, doi: 10.3390/molecules30010164.

[71] S. Stagnoli et al., "Unique catanionic vesicles as a potential 'Nano-Taxi' for drug delivery systems. In vitro and in vivo biocompatibility evaluation," RSC Adv., vol. 7, no. 9, pp. 5372–5380, 2017, doi: 10.1039/C6RA27020D.

[72] I. Polidori, D. To, G. Kali, and A. Bernkop-Schnürch, "Histidine-based ionizable cationic surfactants: novel biodegradable agents for hydrophilic macromolecular drug delivery," Drug Deliv. and Transl. Res., vol. 14, no. 9, pp. 2370–2385, Sept. 2024, doi: 10.1007/s13346-023-01511-8.

[73] D. Crnčević et al., "A dual antibacterial action of soft quaternary ammonium compounds: bacteriostatic effects, membrane integrity, and reduced in vitro and in vivo toxicity," RSC Adv., vol. 15, no. 2, pp. 1490–1506, 2025, doi: 10.1039/D4RA07975B.

[74] L. Pierau, C. Elian, J. Akimoto, Y. Ito, S. Caillol, and D.-L. Versace, "Bio-sourced monomers and cationic photopolymerization–The green combination towards eco-friendly and non-toxic materials," Progress in Polymer Science, vol. 127, p. 101517, Apr. 2022, doi: 10.1016/j.progpolymsci.2022.101517.

[75] J. Guo et al., "Stimuli-responsive antimicrobial polymer systems: From structural design to biomedical applications," Giant, vol. 24, p. 100366, Aug. 2025, doi: 10.1016/j.giant.2025.100366.

ORIGINAL ARTICLE

TRANSLATIONAL CHEMISTRY
AN INTERFACE JOURNAL
HTTPS://WWW.TRANSLATIONALCHEMISTRY.COM/

ORIGINAL ARTICLE | DOI: 10.5584/translationalchemistry.v1i2.248

# Smartphone-based Colorimetric Protein Quantification in Human Urine Using Gold Nanoparticles

Beatriz Quintas[¥,1], Joana Galhano[¥,1], Hugo M. Santos[*,1,2], Elisabete Oliveira[*,1,2,3]

[1]BIOSCOPE Research Group, LAQV-REQUIMTE, Chemistry Department, NOVA School of Science and Technology, NOVA University of Lisbon, 2829-516, Caparica, Portugal. [2]PROTEOMASS Scientific Society, 2825-466, Costa de Caparica, Portugal. [3]Canterbury Christ Church University, School of Human and Life Sciences, Life, Sciences Industry, Liaison Lab, Sandwich, UK. [¥]Both authors contributed equally to this work.

**Received:** 25 November 2025 **Accepted:** 27 November 2025 **Available Online**: 5 December 2025

## Abstract

Proteinuria, the presence of elevated protein levels in urine, is an important biomarker associated with various diseases. This study presents a portable, smartphone-based approach for colourimetric protein detection using gold nanoparticles (AuNPs). By inducing the aggregation of AuNPs in the presence of albumin, facilitated by sodium chloride, distinct colour changes were observed and quantified *via* smartphone image analysis. The method was tested using three smartphone models on urine samples from six volunteers, demonstrating a detection limit of 1.19 µg/mL and the ability to visually detect protein concentrations as low as 25 µg/mL. Furthermore, we successfully quantified the urinary proteome of a CRC patient, obtaining a protein concentration of 37 ± 3 µg/mL, which closely agrees with the value of 41 ± 1 µg/mL determined by the Bradford assay. This technique offers a rapid, cost-effective, and non-invasive tool for urinary protein detection, with promising applications in routine clinical diagnostics and disease monitoring.

**Keywords:** Protein quantification, Proteinuria, Colourimetric detection, RGB analysis, Smartphone-based analysis, Point-of-care testing.

## 1. Introduction

Proteinuria, characterised by elevated concentrations of protein in the urine, is often associated with an increased risk of renal failure [1,2], along with other health conditions like heart disease, diabetes, and infections [3]. Typically, healthy kidneys filter out less than 150 mg of protein daily, with approximately 20 mg of that being albumin [4]. Protein concentrations in urine ranging from 30 to 300 mg per day are classified as microalbuminuria, while those exceeding 300 mg per day are classified as proteinuria [3]. Additionally, if the daily concentration exceeds 3.5 g of protein, it is categorised as nephrotic range proteinuria. Proteinuria may arise from direct damage to the kidney's glomeruli or from the immune system's response to an infection occurring elsewhere in the body [5]. Frontline protein concentration evaluation in urine is often performed through a urine dipstick analysis. Although it does not require complex sample preparation before analysis as some other methods, it has low sensitivity for lower protein concentrations, for individuals with an albumin/creatinine ratio (ACR) ≥ 30 mg/g, being only recommended as a screening tool in older outpatients with ACR ≥ 300 mg/g [6]. As such, these dipsticks might prove inconclusive for some evaluations with a lower protein concentration.

Other methods can be used for a more accurate protein concentration determination, such as mass spectrometry, immunoassays, fluorescence spectroscopy or Raman spectroscopy. However, these require more extensive sample preparation protocols, are more labour-intensive and time-consuming, and also require expensive equipment [3]. Other colorimetric methods, such as the Bradford assay or the Bicinchoninic Acid (BCA) Assay, can also be used to estimate total protein concentration. However, all these have specific limitations, such as incompatibility with surfactants, a wide range of requirements on needed reagents, or lack of specificity for proteins [7]. Apart from these more conventional methods for protein detection, nanomaterials can also be used to detect protein in urine. Several studies in the literature report protein-nanoparticle interactions, often accompanied by colorimetric alterations and the occurrence of precipitation [8]. Moreover, the formation of a protein corona is also described when protein and nanoparticles dynamically interact with each other, forming hard and soft coronas. These interactions depend on many factors, namely, the surface functionalisation of the nanoparticles, nanoparticle surface charge and size, protein composition, and incubation time [9–12]. The adsorption of different proteins to form a protein corona *via* colorimetric changes was quantitatively

***Corresponding author:** Hugo M. Santos and Elisabete Oliveira (hmsantos@fct.unl.pt and ej.oliveira@fct.unl.pt)

characterised by UV-vis absorption spectroscopy [13]. In this assay, four models of proteins were successfully determined with a concentration range of up to 80 µg/mL in water and up to 200 µg/mL in human urine. Moreover, this assay also stands out from conventional commercial protein assays since it allows instantaneous quantification. However, despite being a faster and easier technique, absorption spectroscopy is still necessary for quantification. In recent years, there has been increasing interest in integrating smartphones and image processing programs into chemical analysis, facilitating environmentally friendly, rapid, and cost-effective analytical procedures [14]. Extensive research has been conducted on digital image colourimetry (DIC) as a versatile qualitative and quantitative analysis technique across various sample types, including heavy metals [15], pesticides [16], antibiotics [17], and food products [18]. Despite its versatility, DIC has been underutilised for protein quantification, leaving a significant gap in the research and application of this technique for protein analysis and detection of proteinuria.

Taking advantage of these points, our work sheds light on the development of a more accurate method. Gold nanoparticles (AuNPs) show distinct colours according to the protein-nanoparticle ratios. This allows for a visual determination of albumin in water and protein in urine samples with a minimum concentration of 25 µg/mL. To make the method accessible to everyone, a mathematical model was developed based on the Red-Green-Blue (RGB) characteristics of the colorimetric responses. This model enables the calculation of protein concentration from a simple smartphone image, providing a convenient, fast, and portable solution for protein quantification. As such, the use of nanotechnology combined with DIC methods for protein quantification could bring some advantages for preliminary screenings, not requiring extensive equipment and utilizing a simple sample preparation.

## 2. Materials and methods

### 2.1. Chemicals and Starting Materials

Hydrogen tetrachloroaurate (III) trihydrate (99.99%) was purchased from Thermo Scientific. Sodium citrate, tribasic dihydrate (≥ 99%), Bovine Serum Albumin (BSA ≥ 96%) and Bradford reagent were purchased from Sigma-Aldrich. Reagents were used as received.

### 2.2. Instrumentation

The Nanoparticle size and zeta potential were determined using a Dynamic Light Scattering (DLS) Malvern NanoZetasizer, with a 633 nm laser diode (PROTEOMASS Scientific Society, Caparica, Portugal). UV-Vis absorption spectra were acquired in a Jasco V-650 Spectrophotometer (Jasco Corporation, Tokyo, Japan). 96-well plate readings were performed using a CLARIOSTAR Spectrophotometer (BMG Labtech) (PROTEOMASS Scientific Society Facility). Transmission Electron Microscopy (TEM) images were obtained in a JEOL JEM-2100-HT operating at 200 kV; TEM images were collected using a "OneView" 4k×4k CCD camera. Photography of the 96-well plates for the RGB assessment assay was taken using smartphones, models OPPO Reno8 Lite, Samsung Galaxy S21 FE 5G and an iPhone 14 Pro. The Simplicity® UV ultrapure water purification system from Merck Millipore was used to produce ultrapure water for all the experiments.

### 2.3. Gold Nanoparticle Synthesis and Characterization

AuNPs were synthesised according to an already established Turkevich method [19]. Briefly, 4.9 mg of hydrogen tetrachloroaurate (III) was dissolved in 12.5 mL of ultrapure $H_2O$, and the obtained solution was heated at 100 ºC under stirring at 300 rpm. Then, 1.25 mL of a 10 mg/mL sodium citrate aqueous solution was added to the reactional mixture, and it was left under reflux for approximately 15 minutes until a deep red colour was observed. After the colorimetric alteration, the solution was left to cool down to room temperature. Until further use, the obtained nanoparticles were stored as obtained at 4 ºC to avoid degradation.
The obtained nanoparticles were promptly characterized by acquiring the respective absorption spectrum, and their size and zeta potential were determined through DLS measurements. TEM images were collected to evaluate particle size and morphology.

### 2.4. Albumin Colorimetric Detection with AuNPs in Aqueous Media

To analyse possible protein interactions with **AuNPs** the following experiments were conducted and measured by DLS and UV-Vis spectrum: **AuNPs** (1.7 mL $H_2O$ + 300 µL AuNPs + 1.01 mL $H_2O$); **AuNPs-BSA** (1.7 mL $H_2O$ + 300 µL AuNPs + 10 µL BSA 2 mg/mL + 1 mL $H_2O$); **AuNPs-BSA-NaCl** (1.7 mL $H_2O$ + 300 µL AuNPs + 10 µL BSA 2 mg/mL + 1 mL NaCl 5 M); **AuNPs-NaCl** (1.7 mL $H_2O$ + 300 µL AuNPs + 10 µL $H_2O$ + 1 mL NaCl 5 M). To further evaluate the system's colorimetric behaviour, a high-throughput miniature set of experiments following similar conditions was performed in a 96-well plate. In a 96-well plate, a gradient concentration of BSA in aqueous solution, ranging from 0 to 97 µg/mL, was prepared with a total volume of 170 µL per well. Next, 30 µL of the synthesised AuNPs were added to each well. Finally, 20 µL of an aqueous 5 M NaCl solution was added to each well. Respective controls, without BSA and NaCl, were also performed under the same conditions.

### 2.5. Total Protein Colorimetric Detection with AuNPs in Urine Samples

2.5.1. *Urine sample collection and treatment*

Six urine samples from healthy volunteers and one from a colorectal cancer patient (CRC patient) were collected in sterile collection flasks following informed consent. Before handling, the urine was filtered through a paper filter to remove precipitates. The filtered urine was then diluted 1:20 using ultrapure $H_2O$ and used throughout the study.

2.5.2. *Total Protein Colorimetric Detection with AuNPs in Urine Samples*

Healthy urine samples were spiked with varying concentrations of BSA (from a stock solution of 2 mg/mL) ranging from 0 to 97 µg/mL. In a 96-well plate, 170 µL of each spiked urine solution and CRC patient urine was added, followed by 30 µL of AuNPs and 20 µL of NaCl. One row of wells without NaCl was used as a negative control to evaluate the response without NaCl.

### 2.6. Protein Quantification

2.6.1. *Total Protein Quantification using Bradford Assay*

Total protein quantification of CRC patient urine was performed through a Bradford protein assay [20]. A calibration curve was generated using the following concentrations of BSA stock solutions in ultrapure $H_2O$: 0, 0.25, 0.5, 1.0 and 1.4 g/L. Five microliters of each stock solution were added to a 96-well plate, followed by 250 µL of the Bradford reagent. Five microliters of each urine sample were also added to the 96-well plate with 250 µL of the Bradford reagent. Each experiment was performed in duplicate. The UV-Vis measurements were conducted at 595 nm.

2.6.1. *Protein Quantification using the RGB Method*

A calibration curve was obtained by photographic collection of a BSA aqueous gradient in water from 0 to 97 µg/mL in the presence of AuNPs and NaCl in a transparent 96-well plate. Smartphone models used for photographic collection were Samsung Galaxy S21 FE 5G, OPPO Reno 8 Lite and iPhone 14 Pro. After photograph collection, an RGB analysis of each well was conducted with the image software ImageJ. Mean and specific channel values (red channel, green channel, and blue channel) were collected through specific analysis of the respective well and used to calculate the Response value using the following formula [21]:

$$\text{Response (\%)} = 100 \times ([RGB]_{sample} - [RGB]_{mean})/([RGB]_{mean} - [RGB]_{ref}) \quad (1)$$

Where $[RGB]_{sample}$: RGB value obtained for the well holding the sample; $[RGB]_{mean}$: RGB value obtained for the wells without adding NaCl; $[RGB]_{ref}$ = 255. The obtained Response values were plotted in a linear regression model against $\log_{10}$[BSA] present in each well, yielding the following equation [21]:

$$\text{Response (\%)} = m \log[BSA] + b \quad (2)$$

Where m: slope of the linear regression curve; b: y-intercept of the obtained linear regression curve. Additionally, the limit of detection (LOD) was also calculated from the following formula [21]:

$$LOD = 3.3 \times(\sigma/m) \quad (3)$$

Where: σ is the standard deviation of the response and m: slope of the linear regression curve obtained from the previous equation.

## 3. Optical Properties of Metallic NPs

### 3.1. AuNPs Synthesis and Characterization

Citrate-capped gold nanoparticles (AuNPs) were synthesised following a well-reported Turkevich method [22]. The obtention of a deep-red characteristic colouration in the reactional mixture indicated a well-achieved AuNPs solution. The obtained nanoparticles were first characterised by UV-Vis spectroscopy and DLS analysis, summarising the results in **Figure 1**. AuNPs present a well-defined absorption profile consistent with those reported in the literature for spherical AuNPs, with a typical plasmonic band appearing at 523 nm. Their hydrodynamic diameter (HD) was 32.5 ± 0.3 nm, with a polydispersity index (PDI) of 0.556 ± 0.002. The obtained zeta-potential (ζ) was -30.2 ± 0.7 mV, confirming the successful citrate capping of the particles. TEM was also performed to verify the dispersity, size and morphology of the synthesized nanoparticles. The obtained nanoparticles present a well-defined spherical shape with an average diameter of 14 ± 2 nm. These values are in accordance with others reported in the literature for similar particles [22].

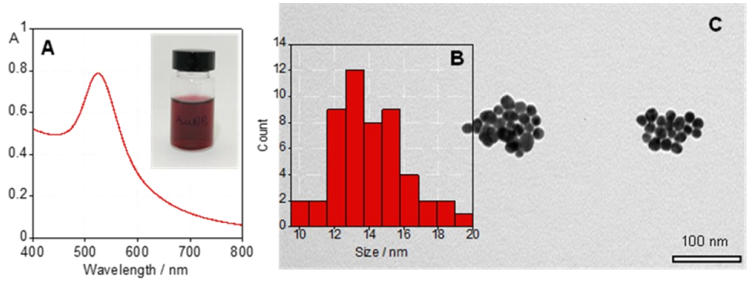


D

| | Particle Diameter (nm) TEM | HD (nm) | PDI | Zeta Potential (mV) |
|---|---|---|---|---|
| AuNPs | 14 ± 2 | 32.5 ± 0.3 | 0.556 ± 0.002 | -30.2 ± 0.7 |

**Figure 1.** Characterisation of AuNPs: (A) absorption spectra; inset: colourimetric evaluation of the freshly synthesised AuNPs; (B) Size distribution for nanoparticles from TEM analysis; (C) TEM image; and (D) size and particle surface charge of the synthesised nanoparticles.

### 3.2. AuNPs-Protein Interaction in Aqueous Environments

To evaluate any interactions that might occur between the nanoparticles and protein, AuNPs were diluted with a dilution factor of 0.18 to a total volume of 2 mL, yielding a homogeneous deep-red nanoparticle suspension. Subsequently, 10 µL of a 2 mg/mL BSA aqueous solution was added to the solution. BSA was selected as a model protein, as albumin is the most prevalent protein in physiological contexts, and the bovine counterpart has similar characteristics to that of the human one. Upon addition of the protein, no colorimetric alterations were verified; however, after the addition of 1 mL of a 5 M NaCl aqueous solution, a substantial colorimetric alteration occurred from red to purple, as seen in **Figure 2**. Upon the addition of NaCl, in the absence of BSA, the nanoparticles lost their deep-red colouration, turning into a clear/grey solution. At each stage, the absorption spectra were collected, and other properties were analysed through DLS, as summarised in **Figure 2**. BSA was added to the AuNPs suspension to a final concentration of 10 µg/mL in the cell. Despite this addition, no colorimetric alterations were observed, with the suspension maintaining its characteristic red colouration. However, from analysis of the UV-Vis spectra, a slight alteration of the absorption maximum was observed, with a shift occurring from 523 to 526 nm. This slight redshift is consistent with reports in the literature regarding protein-AuNPs interaction, possibly through the formation of a "protein corona" [23]. A slight alteration in the hydrodynamic diameter obtained for the AuNPs in the presence and absence of BSA was also verified. This alteration can be derived from forming a "soft corona", meaning the formation of a dynamic layer of protein at the surface of the nanoparticles.

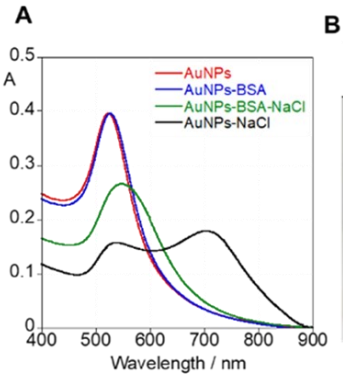


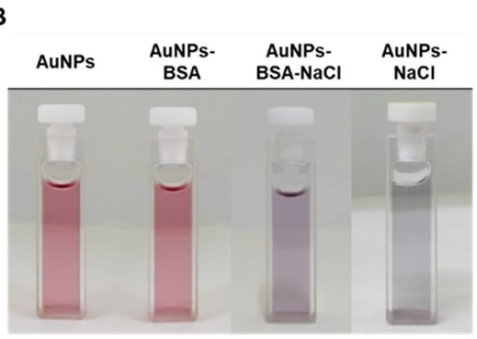


| C | HD (nm) | PDI | Zeta potential (ζ) (mV) |
|---|---|---|---|
| AuNPs | 32.5 ± 0.3 | 0.556 ± 0.002 | -30 ± 1 |
| AuNPs-BSA | 33.4 ± 0.2 | 0.542 ± 0.003 | -21 ± 1 |
| AuNPs-BSA-NaCl | 276 ± 29 | 0.198 ± 0.008 | 55 ± 22 |
| AuNPs-NaCl | 538 ± 27 | 0.24 ± 0.03 | -3.8 ± 0.4 |

**Figure 2.** (A) Absorption spectra of free AuNPs (red); AuNPs in the presence of BSA (blue); AuNPs in the presence of BSA and NaCl (green); AuNPs in the presence of NaCl (black). (B) Colourimetric alterations of the tested conditions; (C) Hydrodynamic diameter, polydispersity index and zeta potential of AuNPs in response to the different tested conditions.

This interaction is, however, clearly noticeable from the zeta-potential data obtained for both solutions. Without the addition of BSA, the AuNPs presented a surface charge of ca. -30 mV, a typical charge for citrate-capped AuNPs, due to the negative charge of the citrate moiety [24]. However, upon BSA addition, this charge was altered to ca. -21 mV. This alteration is indicative of BSA-AuNPs surface interactions, partially neutralising the inherent negative surface charge of the nanoparticles. Interestingly, when adding 1 mL of an aqueous solution of NaCl 5 M, drastically increasing the ionic strength of the solution, a colorimetric alteration took place, changing from red to purple hue. Once again, this alteration was accompanied by a visible alteration in the absorption spectra, where the maximum peak suffered a redshift to 547 nm and a decrease in the absorbance intensity, followed by an increase in the hydrodynamic diameter from 33 nm to 276 nm. Such high values indicate aggregation or clustering phenomena in solution, modulated by the increased ionic strength induced by adding NaCl. Moreover, the zeta-potential measurements indicate a very pronounced charge alteration from the negative values obtained without NaCl. This drastic shift from negative to positive occuring in response to the increased ionic strength of the solution. Several mechanisms might be responsible, however, considering the hydrodynamic diameter values obtained, aggregation phenomena are the most likely to occur. However, another explanation might involve the compression of the electric double layer [25]. This compression could reduce the negative charge available at the surface of the particles, leading to a charge reversal. This effect might also become more pronounced if the free ions in solution adsorb preferentially to the protein corona, particularly $Na^+$ ions, resulting in a more positive zeta potential.

To best understand the role of NaCl and BSA in these systems, measurements were performed in the same conditions as before, replacing the BSA solution with water. The nanoparticles lost their red colour upon the addition of NaCl, acquiring a clear aspect, with no trace of the purple hue observed in the presence of BSA. Once again, this alteration was accompanied by alterations in the UV-Vis spectra, consistent with other spectra reported in the literature for AuNPs in the presence of increasing NaCl concentrations [24]. Once again, a drastic increase in hydrodynamic diameter was observed, surpassing the values observed for the AuNPs in the presence of BSA and NaCl. These results are once again indicative of the occurrence of aggregation phenomena. Comparing the hydrodynamic diameter measurements obtained for AuNPs-NaCl in the presence and absence of BSA underscores the role of BSA in the AuNPs stabilisation in solution. The presence of BSA appears to help the nanoparticle's stabilisation in the presence of higher ionic strength, although some aggregation persists. Additionally, considering the zeta-potential values obtained for the AuNP-NaCl condition of ca. -3.8 mV, being less negative than those presented by the AuNPs alone but not as positive as the system in the presence of BSA (ca. 55 mV). These differing values might arise due to the absence of a protein corona. As no protein corona exists, fewer $Na^+$ ions can interact with the negatively charged citrate molecules present on the surface of the particle, thereby neutralizing part of the surface charges available. Under these conditions, the ratio between $Na^+$ ions and citrate molecules was approximately even, as almost all charges were neutralized. The slight negative charge remaining most likely originates from the citrate molecules that did not interact with the sodium ions in solution.

### 3.3. High-Throughput Colorimetric Protein Detection in $H_2O$

Following the above-described assays, the method was scaled down and further optimized for a high-throughput analysis in ultrapure water. Using a 96-well plate as a high-throughput platform, four conditions were prepared, as seen in **Figure 3**. The four conditions tested yielded a clear differential colorimetric profile. Condition 1 combined the AuNPs in a constant concentration with increasing [BSA] ranging from 0 to 97 µg/mL (0, 1, 2, 5, 10, 25, 50, 97 µg/mL). Additionally, a constant NaCl concentration was added to each of the wells. Condition 2 consists of the AuNPs in the presence of BSA without the addition of NaCl. Condition 3 consists of the AuNPs in the presence of NaCl without adding BSA. Finally, Condition 4 consists of AuNPs in water without BSA or NaCl. Similarly to what was verified and discussed in the previous section, the presence of BSA in solution, in contact with AuNPs, allows for the formation of a protein corona, which cannot be readily identifiable through a naked-eye assessment from the simple addition of protein to the AuNPs, requiring a revealing agent, which for the purposes of this work was NaCl. By increasing the ionic strength of the solutions, the nanoparticles tended to aggregate, losing their optical properties. This aggregation, associated with a loss of colour, is also verified in Condition 3, in which, in the absence of BSA, the solution went from a red/pink colouration, as seen in Conditions 2 and 4, to a transparent/grey colour verified in Condition 3. As seen in Condition 1, upon adding NaCl to the BSA-AuNPs complex, the wells acquired a gradient of colouration, ranging from a grey/purple hue to the expected red/pink, traditional of the AuNPs. With a lower [BSA], the amount of protein interacting with the AuNPs will be smaller, forming a less defined protein corona.

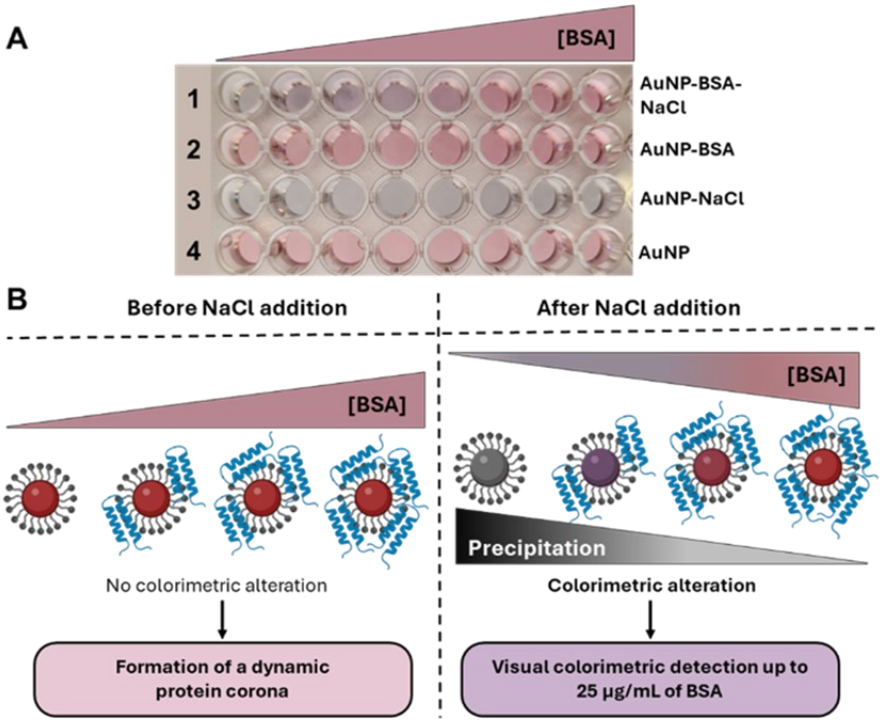


**Figure 3.** (A) Colourimetric response of AuNPs-BSA solution (with increasing [BSA]), upon NaCl addition in water. (B) Schematic overview of the proposed mechanism of action for AuNP-protein interaction.

With the increase of [BSA], the interactions between protein and nanoparticles will also increase and strengthen the protein corona. Upon the addition of NaCl, the nanoparticles that have the strongest protein corona will not aggregate readily. This precipitation ratio will be inversely proportional to the concentration of BSA in the solution, meaning that the more protein in the solution, the less aggregation and precipitation phenomena will occur. This is also consistent with the observed colorimetric profile. The purple hue appears to be an intermediate state between total aggregation/precipitation and a complete protein corona that protects the nanoparticles and prevents the occurrence of these phenomena.

### 3.4. AuNPs-Protein Interaction in Human Urine Samples

Following the promising data obtained for scaling down the assay in water, the same methodology was applied to urine samples to assess the method's applicability for protein detection in biological samples. Six different urine samples were collected from healthy volunteers (n = 6; 50% male and 50% female). To ensure sample and biological diversity, the urines were collected from healthy individuals with different hydration levels on the same day. The urine samples were first subjected to a simple paper filtration to remove any solid deposits and then diluted in $H_2O$ to a 1:20 ratio. Each diluted urine sample was then spiked with specific volumes of BSA to ensure a protein gradient of 0 to 97 µg/mL. Following this, 170 µL of each spiked urine solution was added to a 96-well plate, followed by the subsequent addition of 30 µL of AuNPs and 20 µL of a 5M NaCl aqueous solution. The same colorimetric gradient was observed, consistent with the results obtained in the water-based assay as seen in **Figure 4**. The solution's colouration shifted from a grey/purple hue to a red/pink hue as the BSA concentration in the solution grew. The BSA concentration range in urine was like the one tested in water, displaying a similar colorimetric behaviour across different samples. To verify the consistency of the assay, various urine samples were evaluated through this method, resulting in colour changes like those observed in water. The first five wells, corresponding to a BSA concentration of 0-10 µg/mL, exhibited a purple/grey hue, while wells from the sixth onward remained with the red/pink hue upon NaCl addition. This consistency obtained between the various samples aligns with the proposed mechanism in which, with the increase of BSA in solution, a more stable protein corona forms around the particles, decreasing the precipitation/aggregation phenomena that could occur upon the increase of ionic strength modulated *via* NaCl addition. A similar procedure was performed with the human urine of a patient with colorectal cancer without the addition of BSA. The total protein quantity in the sample was also quantified using Bradford assay.

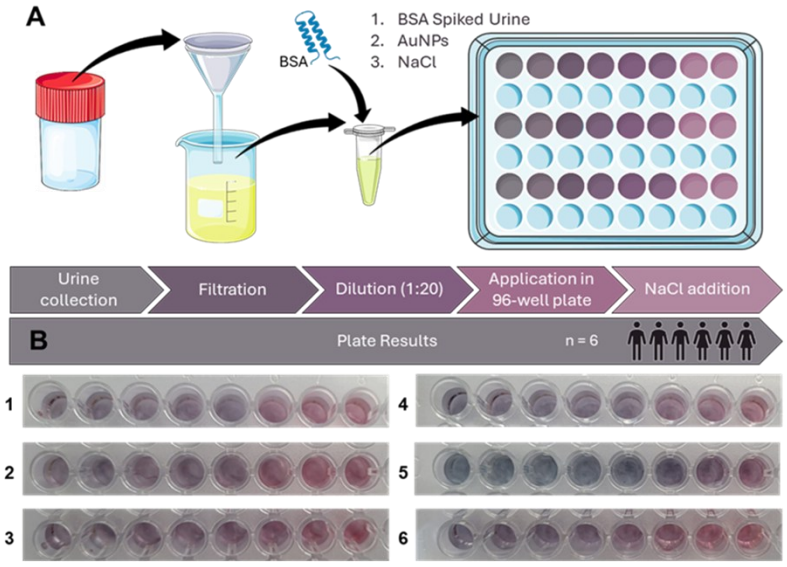


**Figure 4.** (A) Schematic overview of the urine analysis process, from urine collection and treatment to plate application. (B) Colorimetric response of AuNPs-BSA solution (with increasing [BSA]), upon NaCl addition in urine.

### 3.5. RGB Smartphone-Assisted Analysis for Protein Quantification

As the method described above allowed for a qualitative determination of protein in solution through a colorimetric alteration, we aimed to develop a quantitative approach for protein quantification in solution, using AuNPs as colorimetric indicators. This approach was based on others already published in the literature, where, through RGB analysis of a photograph, it is possible to quantify a specific analyte that triggers a colorimetric response on the indicator [21,26,27]. To verify if such an approach was feasible, the first step was to confirm if a linear correlation between the RGB response and the respective BSA concentration in the solution could be obtained. To this end, a BSA gradient in water was performed with the following concentrations: 0, 1, 2, 5, 10, 25, 50, 97 µg/mL, in the presence and absence of NaCl, like the above-mentioned assays in water. Images of the plates were captured with a Samsung Galaxy S21 FE 5G smartphone positioned ca. 20 cm above the plate. The plates were photographed under natural light, without direct sunlight irradiation, to prevent reflectance

interference in the 96-well plate. The captured images were then analysed using the free, open-source ImageJ Software [28] to conduct an RGB analysis. A comprehensive colorimetric analysis was performed, obtaining the respective RGB means, as well as the individual Red, Blue and Green Channels for each well. A selection of 5000 pixels, circular area measurement in ImageJ, was performed in the center part of the wells and all subsequent measurements and colorimetric information was derived from this selection. From here, following a similar approach already reported in the literature, the Response % (R%) was calculated using **Equation 1**, as illustrated in **Figure 5**.

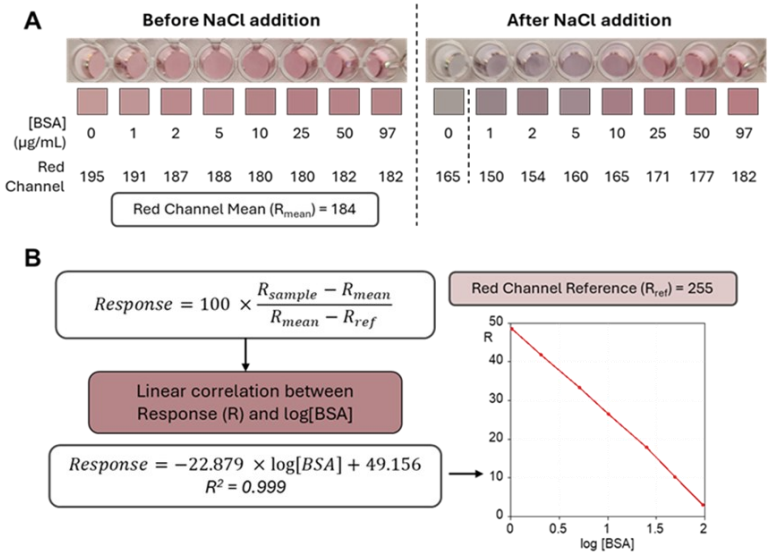


**Figure 5.** (A) Colorimetric analysis of the water-based calibration curve. (B) Mathematical deduction for Response % calculation and linear correlation between Response % and log [BSA].

This percentage was calculated for all the obtained variations of the RGB analysis: RGB mean, Red Channel mean, Blue Channel mean, and Green Channel mean. The analysis demonstrated that the Red Channel values exhibited the most reliable results, demonstrating a strong linear correlation with protein concentration in solution. In contrast, the blue and green channels had a lower variation in response to the protein gradient and were discarded from further analysis. From here, all further studies were conducted exclusively using the Red Channel mean values. **Figure 5** shows the images obtained, their colorimetric analysis, and their respective mathematical approaches. Using the Red Channel mean values it is possible to calculate the Response (%) and correlate it with the log [BSA] values. A strong linear correlation between these two variables was obtained, demonstrating the feasibility of protein quantification through this method. Moreover, the Limit of Detection (LOD) was also calculated [21] from this dataset, being 1.19 µg/mL, with respect to BSA concentration, a value comparable to other protein quantification methods, as seen in **Table SN1**. From here, we moved on to the evaluation of biological samples under the same conditions as described in the above sections, with respect to the assays involving urine samples. Once again, a constant BSA concentration gradient was maintained in the samples. Plate images were captured with three different smartphone models (Samsung Galaxy S21 FE 5G, OPPO Reno 8 Lite and iPhone 14 Pro) to introduce variation in the analysis and assess the consistency of the method across different camera and smartphone models. Once again, the images were obtained under natural light without direct sun irradiation to avoid the occurrence of reflections in the photograph, at ca. 20 cm from the plate.

The images obtained were evaluated using the ImageJ software, with mean Red Channel values obtained for each condition. After this colorimetric analysis, the recovery percentage was calculated to assess the accuracy of each smartphone model. Additionally, an ANOVA statistical analysis (n = 6; α = 0.05) was performed to evaluate the potential statistical variance within each smartphone model. The results, as shown in **Table SN2**, indicate that for all models, the p-values were greater than 0.05, suggesting no significant variation in recovery percentages among the individual measurements for each smartphone model. **Table 1** summarises the results obtained for each smartphone model tested. All p-values were $p > 0.05$. The complete recovery data for all BSA concentrations and respective Recovery % values are included in the Supplementary Material. From the previous table's analysis, it becomes clear that the Recovery (%) values were close to 100%, demonstrating the assay's reliability in estimating a quantitative determination of protein in urine in the proposed conditions. Moreover, the statistical ANOVA analysis also demonstrates no significant differences between the smartphone models used, proposing that this method might be used regardless of the smartphone model and camera characteristics used. In addition to these analysis and validation tests, a similar approach was conducted using a urine sample from a patient with colorectal cancer as a preliminary proof of concept for the implementation of this methodology in clinically relevant samples. This sample underwent a parallel assessment through the Bradford assay to allow for a comparative analysis between one of the most employed and established protein quantification methods and the proposed colorimetric method.

**Table 1.** Summary of the Response % obtained for each smartphone model.

| Smartphone model | Individual | %Recovery ± Standard Deviation |
|---|---|---|
| Samsung Galaxy S21 FE 5G | 1 | 111 ± 12 |
| | 2 | 105 ± 14 |
| | 3 | 108 ± 6 |
| | 4 | 125 ± 12 |
| | 5 | 105 ± 17 |
| | 6 | 111 ± 11 |
| iPhone 14 Pro | 1 | 95 ± 10 |
| | 2 | 113 ± 14 |
| | 3 | 112 ± 11 |
| | 4 | 113 ± 15 |
| | 5 | 115 ± 15 |
| | 6 | 109 ± 10 |
| OPPO Reno 8 Lite | 1 | 104 ± 9 |
| | 2 | 104 ± 14 |
| | 3 | 114 ± 7 |
| | 4 | 109 ± 10 |
| | 5 | 110 ± 13 |
| | 6 | 99 ± 9 |

**Figure 6** summarises the protein quantification results obtained from the two methods. The image was analysed using the ImageJ software, analysing the section highlighted in **Figure 6**.

From these data, we obtained a Response % of 44.59, which translates to a protein concentration of ca. 1.8 ± 0.2 µg/mL. Considering the dilution factors, the protein concentration in the urine sample calculated through our method was 37 ± 3 µg/mL. In comparison, Bradford quantification yielded a total protein concentration of ca. 41 ± 1 µg/mL. These two values are similar to each other, allowing for the validation of this assay as a powerful tool for protein quantification in urine through a simple, fast and high-throughput method, which relies on a simple photograph analysis obtained *via* a smartphone camera.

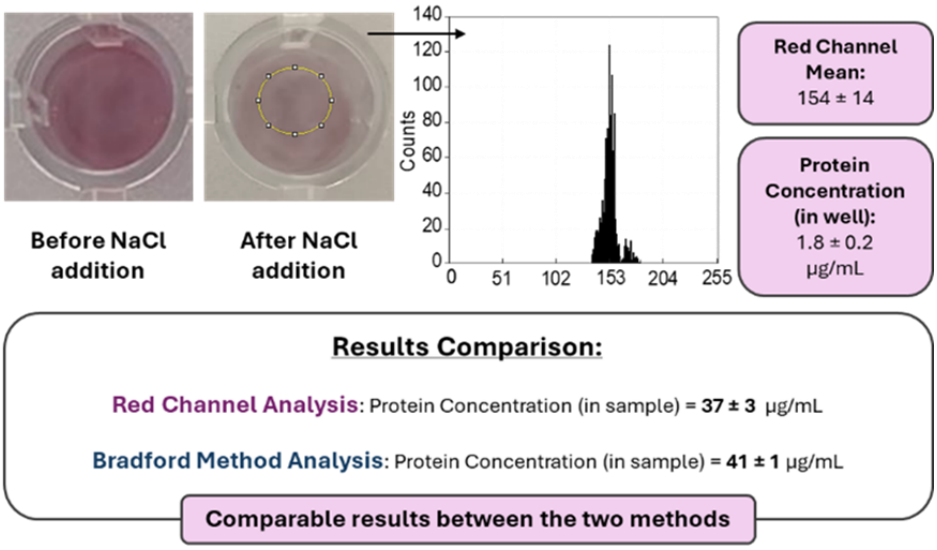


**Figure 6.** Summary of the colorimetric analysis of the patient's urine and respective protein quantification results obtained from the Red Channel Analysis and Bradford Method Analysis.

## 5. Concluding Remarks

In this study, we have demonstrated the feasibility of using gold nanoparticles (AuNPs) for sensitive and specific protein detection, mainly albumin, in urine samples. The interaction between AuNPs and proteins, facilitated by NaCl, induced distinct colorimetric changes that were quantitatively analysed using RGB values obtained from smartphone images. This method showed promising results in visually detecting protein concentrations as low as 25 µg/mL in both aqueous solutions and urine samples. Integrating smartphone-based RGB analysis further enhances the method's accessibility and usability, enabling the determination of protein with a detection limit of 1.19 µg/mL. Moreover, the assay results were also effective for monitoring protein in CRC, where a protein concentration value of 37.17 µg/mL was determined and further validated by the Bradford method. This approach shows great potential for the early detection and monitoring of urinary protein through non-invasive analysis. By offering a rapid, cost-effective, and portable method for protein quantification, our findings may offer a useful tool for monitoring proteinuria in patients.

## Supplementary Material

The following supplementary material is available: **Table SN1**: Limits of Detection (LOD) for various techniques for protein detection and quantification; **Table SN2**: Response% data obtained for each smartphone model and each specific condition.

## Acknowledgements

This work was financed by national funds from FCT - Fundação para a Ciência e a Tecnologia, I.P., under the scope of the project UID/50006/2023 of the Associate Laboratory for Green Chemistry-LAQV REQUIMTE; as well as the PROTEOMASS Scientific Society (Portugal) for funding support (General Funding Grant 2023–2024). J.G. thanks FCT/MCTES for doctoral support (Grant 2022.09495.BD; https://doi.org/10.54499/2022.09495.BD). E.O. thanks Universidade Nova de Lisboa and Fundação para a Ciência e a Tecnologia (FCT) for the Assistant Professor contract granted under the FCT Tenure Programme (2023.11076.TENURE.116). H.M.S. thanks LAQV for his research contract support. We extend our sincere gratitude to Professors C. Lodeiro and J.L. Capelo for their invaluable contributions, particularly in securing funding for state-of-the-art instrumentation at NOVA FCT through collaborative efforts, which have been essential for the success of this research.

## Informed Consent Statement

Informed consent was obtained from all subjects involved in the study.

## References

[1] K. Tryggvason, E. Pettersson, Causes and consequences of proteinuria: the kidney filtration barrier and progressive renal failure, J Intern Med 254 (2003) 216–224. https://doi.org/10.1046/J.1365-2796.2003.01207.X.

[2] J. Park, D.W. Shin, K. Han, D. Kim, S. Chun, H.R. Jang, Associations Between Kidney Function, Proteinuria, and the Risk of Kidney Cancer: A Nationwide Cohort Study Involving 10 Million Participants, Am J Epidemiol 190 (2021) 2042–2052. https://doi.org/10.1093/aje/kwab140.

[3] S. Aitekenov, A. Gaipov, R. Bukasov, Review: Detection and quantification of proteins in human urine, Talanta 223 (2021) 121718. https://doi.org/10.1016/j.talanta.2020.121718.

[4] A.S.A. Naderi, R.F. Reilly, Primary Care Approach to Proteinuria, The Journal of the American Board of Family Medicine 21 (2008) 569–574. https://doi.org/10.3122/jabfm.2008.06.070080.

[5] J.E. Toblli, P. Bevione, F. Di Gennaro, L. Madalena, G. Cao, M. Angerosa, Understanding the Mechanisms of Proteinuria: Therapeutic Implications, Int J Nephrol 2012 (2012) 1–13. https://doi.org/10.1155/2012/546039.

[6] D. Lim, D.-Y. Lee, S.H. Cho, O.Z. Kim, S.W. Cho, S.K. An, H.W. Kim, K.H. Moon, M.H. Lee, B. Kim, Diagnostic accuracy of urine dipstick for proteinuria in older outpatients, Kidney Res Clin Pract 33 (2014) 199–203. https://doi.org/10.1016/j.krcp.2014.10.003.

[7] J.G. Song, K.C. Baral, G.-L. Kim, J.-W. Park, S.-H. Seo, D.-H. Kim, D.H. Jung, N.L. Ifekpolugo, H.-K. Han, Quantitative analysis of therapeutic proteins in biological fluids: recent advancement in analytical techniques, Drug Deliv 30 (2023). https://doi.org/10.1080/10717544.2023.2183816.

[8] F. Jia, Q. Liu, W. Wei, Z. Chen, Colorimetric sensor assay for discrimination of proteins based on exonuclease I-triggered aggregation of DNA-functionalized gold nanoparticles, Analyst 144 (2019) 4865–4870. https://doi.org/10.1039/C9AN00918C.

[9] L. Treuel, G.U. Nienhaus, Toward a molecular understanding of nanoparticle–protein interactions, Biophys Rev 4 (2012) 137–147. https://doi.org/10.1007/s12551-012-0072-0.

[10] P. Breznica, R. Koliqi, A. Daka, A review of the current understanding of nanoparticles protein corona composition, Med Pharm Rep 93 (2020) 342–350. https://doi.org/10.15386/mpr-1756.

[11] S.R. Saptarshi, A. Duschl, A.L. Lopata, Interaction of nanoparticles with proteins: relation to bio-reactivity of the nanoparticle, J Nanobiotechnology 11 (2013) 26. https://doi.org/10.1186/1477-3155-11-26.

[12] G. Bashiri, M.S. Padilla, K.L. Swingle, S.J. Shepherd, M.J. Mitchell, K. Wang, Nanoparticle protein corona: from structure and function to therapeutic targeting, Lab Chip 23 (2023) 1432–1466. https://doi.org/10.1039/D2LC00799A.

[13] Y.T. Ho, B. Poinard, E.L.L. Yeo, J.C.Y. Kah, An instantaneous colorimetric protein assay based on spontaneous formation of a protein corona on gold nanoparticles, Analyst 140 (2015) 1026–1036. https://doi.org/10.1039/C4AN01819B.

[14] S.H. Elagamy, L. Adly, M.A. Abdel Hamid, Smartphone based colorimetric approach for quantitative determination of uric acid using Image J, Scientific Reports 2023 13:1 13 (2023) 1–9. https://doi.org/10.1038/s41598-023-48962-0.

[15] R. Sivakumar, N.Y. Lee, Recent progress in smartphone-based techniques for food safety and the detection of heavy metal ions in environmental water, Chemosphere 275 (2021) 130096. https://doi.org/10.1016/J.CHEMOSPHERE.2021.130096.

[16] T. Zhao, X. Liang, X. Guo, X. Yang, J. Guo, X. Zhou, X. Huang, W. Zhang, Y. Wang, Z. Liu, Z. Jiang, H. Zhou, H. Zhou, Smartphone-based colorimetric sensor array using gold nanoparticles for rapid distinguishment of multiple pesticides in real samples, Food Chem 404 (2023) 134768. https://doi.org/10.1016/J.FOODCHEM.2022.134768.

[17] F.J. Cao, H.H. Cheng, S.X. Ma, F. Jiao, D.M. Dong, Three-channel smartphone-based aptamer sensor for multiplexed detecting antibiotics in water through resonance light scattering, Sens Biosensing Res 38 (2022) 100533. https://doi.org/10.1016/J.SBSR.2022.100533.

[18] B. Peng, J. Zhou, J. Xu, M. Fan, Y. Ma, M. Zhou, T. Li, S. Zhao, A smartphone-based colorimetry after dispersive liquid–liquid microextraction for rapid quantification of calcium in water and food samples, Microchemical Journal 149 (2019) 104072. https://doi.org/10.1016/J.MICROC.2019.104072.

[19] J. Turkevich, P.C. Stevenson, J. Hillier, A study of the nucleation and growth processes in the synthesis of colloidal gold, Discuss Faraday Soc 11 (1951) 55. https://doi.org/10.1039/df9511100055.

[20] M.M. Bradford, A rapid and sensitive method for the quantitation of microgram quantities of protein utilizing the principle of protein-dye binding, Anal Biochem 72 (1976) 248–254. https://doi.org/10.1016/0003-2697(76)90527-3.

[21] E. Tan, İ.M. Kahyaoğlu, S. Karakuş, A sensitive and smartphone colorimetric assay for the detection of hydrogen peroxide based on antibacterial and antifungal matcha extract silver nanoparticles enriched with polyphenol, Polymer Bulletin 79 (2022) 7363–7389. https://doi.org/10.1007/s00289-021-03857-w.

[22] G.A. Marcelo, M.P. Duarte, E. Oliveira, Gold@mesoporous silica nanocarriers for the effective delivery of antibiotics and by-passing of β-lactam resistance, SN Appl Sci 2 (2020) 1354. https://doi.org/10.1007/s42452-020-3023-6.

[23] A. Gomes, J.M. Carnerero, A. Jimenez-Ruiz, E. Grueso, R.M. Giráldez-Pérez, R. Prado-Gotor, Lysozyme–AuNPs Interactions: Determination of Binding Free Energy, Nanomaterials 11 (2021) 2139. https://doi.org/10.3390/nano11082139.

[24] S. Vijayakumar, S. Ganesan, Preparation and stability of gold nanoparticles, Indian Journal of Physics 86 (2012) 989–995. https://doi.org/10.1007/s12648-012-0161-8.

[25] S. Bhattacharjee, DLS and zeta potential – What they are and what they are not?, Journal of Controlled Release 235 (2016) 337–351. https://doi.org/10.1016/j.jconrel.2016.06.017.

[26] G. de Carvalho Oliveira, C.C.S. Machado, D.K. Inácio, J.F. da Silveira Petruci, S.G. Silva, RGB color sensor for colorimetric determinations: Evaluation and quantitative analysis of colored liquid samples, Talanta 241 (2022) 123244. https://doi.org/10.1016/j.talanta.2022.123244.

[27] L. Engel, I. Benito-Altamirano, K.R. Tarantik, C. Pannek, M. Dold, J.D. Prades, J. Wöllenstein, Printed sensor labels for colorimetric detection of ammonia, formaldehyde and hydrogen sulfide from the ambient air, Sens Actuators B Chem 330 (2021) 129281. https://doi.org/10.1016/j.snb.2020.129281.

[28] C.A. Schneider, W.S. Rasband, K.W. Eliceiri, NIH Image to ImageJ: 25 years of image analysis, Nat Methods 9 (2012) 671–675. https://doi.org/10.1038/nmeth.2089.

TRANSLATIONAL CHEMISTRY
AN INTERFACE JOURNAL
HTTPS://WWW.TRANSLATIONALCHEMISTRY.COM/

ORIGINAL ARTICLE | DOI: 10.5584/translationalchemistry.v1i2.250

# Fluorous Tails and Anion Effects as Dual Drivers of Ionic Self-Assembly in Triazolium Ionic Liquid Crystals

Ignazio Fiduccia[1,¥], Carla Rizzo[1,¥], Davide Ricci[1], Andrea Pace[1], Ivana Pibiri[*]

[1]Department of Biological, Chemical and Pharmaceutical Sciences and Technologies (STEBICEF), University of Palermo, Viale delle Scienze, Ed. 17, 90128 Palermo, Italy. [¥]Both authors contributed equally to this work.

**Received:** 10 December 2025 **Accepted:** 17 December 2025 **Available Online**: 24 December 2025

## Abstract

A series of perfluoroheptyl-substituted 1,2,4-triazolium ionic liquid crystals differing for the phenyl alkoxy substitution pattern (4-substituted, 3,4-substituted, 3,5-substituted) and the counter-ion ($OTf^-$, $PF_6^-$, $NTf_2^-$) have been investigated. Anion-exchange metathesis of three triazolium triflates gave five additional salts, all characterized by Differential Scanning Calorimetry and Polarized Optical Microscopy. Data reveal a consistent counter-ion effect: $NTf_2^-$ derivatives exhibit lower melting and clearing temperatures than their $PF_6^-$ analogues. Mesophase breadth and complexity are primarily dictated by cation structure, with 3,5-disubstituted derivatives showing narrow mesophase windows, while 4- and 3,4-substituted cations exhibit broader ranges and multiple transitions. Polarized Optical Microscopy observations corroborate smectic behavior in single-chain derivatives and layered or columnar organization in dialkyloxy analogues. Besides, dendritic growth in the 3,4-substituted $PF_6^-$ salt suggests discotic aggregation. Overall, the combined effects of selective anion exchange and controlled peripheral substitution provide an effective strategy to tune mesophase type, thermal behavior and supramolecular organization in perfluoroalkyl triazolium ionic liquid crystals, offering transferable design principles for engineering fluorinated ILCs with targeted properties for structured electrolytes, ion-conductive materials and responsive soft devices.

**Keywords:** Fluorinated materials, Ionic liquid crystals, Anion methatesis, Heterocyclic compounds , Triazolium salts.

## 1. Introduction

Ionic liquid crystals (ILCs) are low-melting organic salts that combine persistent orientational order with ionic mobility, so they occupy an intermediate regime between conventional liquid crystals and ionic liquids [1–3]. The coexistence of anisotropic supramolecular order and mobile charge carriers gives rise to combined properties such as low volatility, ionic conductivity and directional supramolecular order, which make ILCs attractive for applications in energy storage, electrochemical devices, sensing and separation technologies [4–7]. Early work on ILCs focused on classical cation families such as imidazolium and pyridinium thanks to their synthetic accessibility and well-studied self-assembly behavior [1,2]. In recent years the field has broadened to include alternative heterocyclic scaffolds, including oxadiazole and triazole cores, which offer distinct electronic distributions and substitution patterns and therefore additional handles to tune molecular shape and mesophase formation [8–12]. Synthetic approaches that transform 1,2,4-oxadiazoles into 1,2,4-triazoles by ANRORC mechanism (Addition of Nucleophiles, Ring Opening and Ring Closure) have been widely used to introduce perfluoroalkyl substituents on the heterocyclic core in a concise and reliable manner [8,13,14]. Incorporation of perfluoroalkyl segments into mesogenic molecules modifies nanoscale segregation and molecular packing relative to purely hydrocarbon analogues. Fluorous domains often stabilize smectic or columnar arrangements while affecting thermal stability and ionic transport [5,9,15]. This triphilic architecture, in which ionic, hydrocarbon and fluorous subdomains coexist, leads to distinctive mesoscale organization and to opportunities for designing directional ionic channels and selective supramolecular assemblies [16–18]. The specific balance between van der Waals interactions among alkyl chains, fluorous segregation and Coulombic forces determines whether a system favors smectic layering, columnar stacking or other mesomorphic symmetries [19,16,20]. Counter-ion identity represents a second, experimentally accessible design variable that strongly affects phase behavior [1,11,21]. Anion size, polarizability and charge delocalization influence ion pairing, lattice cohesion

***Corresponding author:** Ivana Pibiri | ivana.pibiri@unipa.it

and the free volume available for chain motion. Systematic anion exchange by metathesis is therefore a routine and effective strategy to probe how the anion controls melting and clearing temperatures, mesophase breadth and ionic dynamics [11,21]. Within the 1,2,4-triazolium family, previous studies have shown that perfluoroalkyl tail length, the number and position of alkoxy substituents on the aromatic ring, and the identity of the counter-ion collectively govern mesophase type, including smectic, columnar or other mesophase types, and the thermal stability of those phases [5,10,11,18]. Because these structural and ionic variables are interdependent, comparative studies that hold the perfluoroalkyl tail constant while varying only peripheral alkoxy substitution and counter-ion provide a direct route to separate geometric and ionic effects on mesomorphism. Such systematic datasets are valuable both for mechanistic interpretation and for practical design rules. To facilitate direct comparison with earlier studies, **Scheme 1** collects selected literature triazolium salts together with the new compounds prepared in this work. The upper panel reproduces the 4-substituted triazolium triflates and the related $NTf_2^-$ analogue described by Rizzo *et al.* [21] and the 3,5-disubstituted triazolium triflate reported by Riccobono *et al.* [11]. The lower panel presents the triazolium salts synthesized in the present study, which differ from previous ones in the pattern of alkoxy substitution, on the phenyl ring and in the counter-ion. Specifically, a series of dialkyloxy-phenyl 1,2,4-triazolium salts bearing a fixed perfluoroheptyl substituent has been synthesized. The cationic cores share the same perfluoroalkyl tail but differ in the position of the long alkoxy chains on the phenyl ring, which were introduced in the 4-, 3,4- and 3,5-arrangements. Selected triazolium triflates were converted into $PF_6^-$ and $NTf_2^-$ salts by controlled anion metathesis. The products were characterized by differential scanning calorimetry (DSC) and polarized optical microscopy (POM). Because the perfluoroalkyl tail is constant across the series, this dataset allows us to isolate the separate contributions of peripheral substitution pattern and counter-ion identity on mesophase type, transition temperatures and mesoscale ordering in this family of perfluoroalkyl triazolium ILCs. This study complements and extends recent triazolium ILC work in the literature and provides a systematic dataset to isolate the roles of peripheral substitution and anion identity.

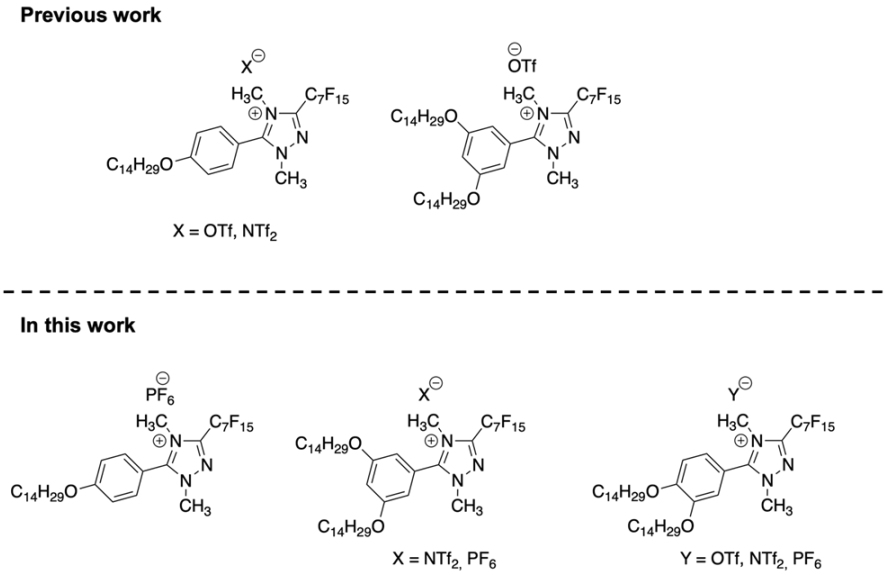


**Scheme 1 | Structures of triazolium salts.** Upper panel: literature triazolium salts reproduced for comparison; 4-substituted triazolium triflates and the corresponding $NTf_2^-$ derivative from Rizzo *et al.* [21], and the 3,5-disubstituted triazolium triflate from Riccobono *et al.* [11]. Lower panel: triazolium salts synthesized in this work.

## 2. Materials and methods

### 2.1. General

2.1.1. Materials

Piperonal, sodium hydroxide, hydroxylamine hydrochloride, methylhydrazine, boron tribromide, pentadecafluorooctanoyl chloride, potassium carbonate, 1-bromotetradecane, methyl trifluoromethanesulfonate, ethyl acetate, petroleum ether, dimethyl sulfoxide, *N,N*-dimethylformamide, toluene, chloroform, methanol, ethanol (96%), acetonitrile, and pyridine were purchased from a commercial source and used as received. Two triazolium triflates (*5-(3,5-bis(tetradecyloxy)phenyl)-1,4-dimethyl-3-(perfluoroheptyl)-1H-1,2,4-triazol-4-ium trifluoromethanesulfonate* and *5-(4-(tetradecyloxy)phenyl)-1,4-dimethyl-3-(perfluoroheptyl)-1H-1,2,4-triazol-4-ium trifluoromethanesulfonate*) were synthesized as described by Rizzo *et al.* [21] and Riccobono *et al.* [11].

2.1.2. Methods

$^1$H-NMR spectra were recorded on Bruker instrument operating at 300 MHz MHz spectrometer. Chemical shifts were referenced to the residual solvent peak. High-resolution mass analyses (HPLC/ESI/Q-TOF HRMS) were performed using HPLC/MS-grade water and acetonitrile containing 0.1% (v/v) formic acid. Chromatographic separations were carried out on an Agilent 1260 Infinity system equipped with a Luna Omega Polar C18 column (5 µm, 150 x 2.1 mm) and a Phenomenex C18 guard cartridge (4 x 3 mm). The flow rate was set at 1 mL/min whilst the column

maintained at 40 °C. A linear gradient was employed as follows: 95% to 5% water over 10 min, 5% to 95% water over the next 10 min, and finally 95% to 5% water during the last 5 min. Sample injections were 10 µL, and chromatograms were monitored using MS TIC. Mass spectra were registered on an Agilent 6540 UHD accurate-mass Q-TOF spectrometer equipped with a Dual AJS ESI source working in positive mode. $N_2$ was used as a desolvation gas at 300 °C and a flow rate of 9 L/min. The nebulizer pressure was set to 45 psi. The Sheath gas temperature was set at 350 °C and a flow of 12 L/min. The capillary voltage was adjusted to 3.5 kV, and the fragmentor to 110 V. Data were collected over an m/z range of 150-2000. POM was conducted using a Zeiss Axio Imager.A2m microscope (Carl Zeiss, Göttingen, Germany) equipped with a Linkham LTS420E hot stage controlled by a Linkpad T95-LTS unit. Samples were mounted between a glass slide and coverslip and subjected to heating and cooling cycles at 5 °C·min$^{-1}$. Photomicrographs were captured with an Axiocam ICC1 camera at magnifications of 5x, 10x, and 20x under cross-polarized illumination. DSC was performed using a TA Instruments 2920 DSC system equipped with a refrigerated cooling accessory. Approximately 4 mg of sample were sealed in aluminum TA Tzero Hermetic Pans. Heating and cooling scans were conducted at 10 ° C·min$^{-1}$ under a nitrogen flow of 60 mL·min-1. Each analysis consisted of three consecutive heating and cooling cycles in a range comprised between -50 °C and 220 °C in dependence of compound analyzed.

### 2.2. Synthesis of 3,4-Methylenedioxybenzonitrile (1)

Piperonal (6.1 g; 40.6 mmol) was dissolved in DMSO. $NH_2OH{\cdot}HCl$ (5.2 g; 1.9 mol eq.) was added, and the mixture was stirred at room temperature for 10 min. The DMSO was then removed by sublimation using a freeze dryer. The crude residue was isolated and purified by column chromatography, using a 10:1 petroleum ether/ethyl acetate mixture as the eluent. A white solid was obtained. **3,4-Methylenedioxybenzonitrile (1)**: white solid. Yield = 82%. $^1$H NMR (300 MHz, $CDCl_3$) δ: 7.21 (dd, J = 8.1, 1.5 Hz, 1H), 7.04 (d, J = 1.5 Hz, 1H), 6.86 (d, J = 8.1 Hz, 1H), 6.07 (s, 2H).

### 2.3. Synthesis of N-Hydroxy-1,3-benzodioxole-5-carboximidamide (2)

3,4-Methylenedioxybenzonitrile (4.9 g; 33.3 mmol) was dissolved in EtOH (70 mL), and a mixture of two aqueous solutions of NaOH (1.6 g; 1.2 mol eq.) and $NH_2OH{\cdot}HCl$ (2.7 g; 1.2 mol eq.) was added. The reaction mixture was refluxed for 6 h. After evaporation to dryness, water was added to the residue, leading to the precipitation of the N-Hydroxy-1,3-benzodioxole-5-carboximidamide (2). A white solid was obtained. **N-Hydroxy-1,3-benzodioxole-5-carboximidamide (2)**: white solid. Yield = 85.6%. $^1$H NMR (300 MHz, DMSO-d6) δ: 9.51 (s, 1H), 7.21 – 7.17 (m, 2H), 6.90 (d, J = 8.7 Hz, 1H), 6.03 (s, 2H), 5.73 (s, 2H).

### 2.4. Synthesis of 1,2,4-Oxadiazole (3)

*N*-Hydroxy-1,3-benzodioxole-5-carboximidamide (4.7 g; 26.1 mmol) was dissolved in toluene, and pentadecafluorooctanoyl chloride (13 mL; 2 mol eq.) together with pyridine (4.2 mL; 2 mol eq.) were added. The reaction mixture was refluxed for 6 h. After evaporation to dryness, water was added while maintaining the pH between 4 and 5. The product was isolated by extraction with ethyl acetate and purified by column chromatography, using a 10:1 petroleum ether/ethyl acetate mixture as the eluent. A white solid was obtained. **Compound (3)**: white solid. Yield = 45.5%. $^1$H NMR (300 MHz, $CDCl_3$) δ: 7.70 (dd, J = 8.1, 1.4 Hz, 1H), 7.55 (s, 1H), 6.93 (d, J = 8.1 Hz, 1H), 6.07 (s, 2H).

### 2.5. Synthesis of the Perfluoroalkylated Triazole Derivative (4)

Compound (3) (0.5 g; 0.89 mmol) was dissolved in 3 mL of *N,N*-dimethylformamide, and methylhydrazine (471 µL; 10 mol eq.) was added. The reaction was carried out at 153 °C for 2 h, leading to the formation of a perfluoroalkylated triazole ring. The reaction mixtures were combined in a flask, water was added, and the solution was neutralized with HCl. The product was isolated by extraction with diethyl ether and purified by column chromatography, using a 5:1 petroleum ether/ethyl acetate mixture as the eluent. A white solid was obtained. **Compound (4)**: white solid. Yield = 76%. $^1$H NMR (300 MHz, $CDCl_3$) δ: 7.21 – 7.18 (m, 2H), 6.95 (d, J = 7.8 Hz, 1H), 6.07 (s, 2H), 4.06 (s, 3H).

### 2.6. Synthesis of the Compound (5)

Compound (4) (0.5 g; 0.87 mmol) was dissolved in toluene (50 mL) and reacted with $BBr_3$ (250 µL; 3 mol eq.) under reflux for 3 h. Water was then added, and the reaction was maintained under reflux for an additional 30 min. The reaction mixture was transferred to a flask, concentrated to dryness to remove toluene, then water was added and the mixture was neutralized with a saturated $NaHCO_3$ solution. The product was isolated by extraction with ethyl acetate and purified by column chromatography, using a 5:1 petroleum ether/ethyl acetate mixture as the eluent. A yellow liquid was obtained. **Compound (5)**: Yellow liquid. Yield = 80%. $^1$H NMR (300 MHz, $CDCl_3$) δ: 7.12 (s, 1H), 6.96 (d, J = 8.2 Hz, 1H), 6.88 (d, J = 8.2 Hz, 1H), 4.01 (s, 3H).

### 2.7. Synthesis of the Triazole precursor (6)

In a pressure tube, compound (5) (0.4 g; 0.715 mmol) was dissolved in acetonitrile (7 mL), followed by the addition of $K_2CO_3$ (0.6 g; 6 mol eq.). Subsequently, 1-bromotetradecane (1 mL; 5 mol eq.) was added. The reactions were maintained at 82 °C under stirring. The formation of the perfluoroalkyl-substituted triazoles was monitored by Thin-Layer Chromatography. The reaction mixture was transferred into a 250 mL flask, concentrated to dryness to remove acetonitrile, then water was added and the mixture was neutralized by addition of HCl. The product was isolated and purified by extraction with ethyl acetate followed by column chromatography, using a 20:1 petroleum ether/ethyl acetate mixture as the eluent. The product was obtained as white solid. **Compound (6)**: white solid. Yield = 82%. $^1$H NMR (300 MHz, $CDCl_3$) δ: 7.24 (d, J = 9.6 Hz, 1H), 7.19 (dd, J = 8.3, 1.8 Hz, 1H), 6.97 (d, J = 8.3 Hz, 1H), 4.10

– 4.02 (m, 7H), 1.84 (h, J = 6.3 Hz, 4H), 1.55 – 1.21 (m, 44H), 0.87 (t, J = 6.3 Hz, 6H).

### 2.8. Synthesis of Trifluoromethanesulfonate Triazolium Salt

A solution of Compound (6) (0.5 g; 0.52 mmol) in toluene (10 mL) was placed in a sealed tube, and $CF_3SO_2OCH_3$ (1.5 mL; 26 mol eq.) was added. The mixture was heated at 110 °C for 2 h. After completion, the reaction was concentrated under reduced pressure to remove toluene, followed by addition of water and neutralization of the excess $CF_3SO_2OCH_3$ with NaOH. The product was isolated by extraction with ethyl acetate and purified by column chromatography using a 5:1 petroleum ether/ethyl acetate mixture as the eluent. The compound was obtained as a white solid. HPLC-MS analysis confirmed the identity of the compound and the absence of significant organic impurities. **5-(3,4-bis(tetradecyloxy) phenyl)-1,4-dimethyl-3-(perfluoroheptyl)-1H-1,2,4-triazol-4-ium trifluoromethanesulfonate [Tr-7,p-m14][OTf] (7)**: white solid. Yield = 67%. $^1$H NMR (300 MHz, $CDCl_3$) δ: 7.45 (d, J = 2.1 Hz, 1H, Har), 7.24 (d, J = 2.0 Hz, 1H, Har), 7.08 (d, J = 8.5 Hz, 1H, Har), 4.13 – 4.04 (m, 7H, $OCH_2$ + N-$CH_3$), 3.90 (s, 3H, N-$CH_3$), 1.85 (dt, J = 14.2, 7.2 Hz, 4H, $CH_2$), 1.48 (q, J = 7.2 Hz, 4H, $CH_2$), 1.26 (d, J = 2.4 Hz, 40H, $CH_2$), 0.90 – 0.84 (m, 6H, $CH_3$). HRMS: m/z = calcd for $C_{45}H_{67}F_{15}N_3O_2$ $[M]^+$ 966.4988; found 966.5008. The triflate triazolium salt obtained in Section 2.8 is reported here and its preparation is described above. Two other triazolium triflate salts used as precursors for the anion-exchange (metathesis) reactions were synthetized according to previously published procedures [11,21] and are therefore not detailed here.

### 2.9. Synthesis of Bis(trifluoromethanesulfonyl)imide Salts

In separate 50 mL flasks, methyl triflate salts (80 mg; 0.08 mmol) were dissolved in methanol (5 mL). Lithium bis (trifluoromethanesulfonyl)amide (3.5 mol eq.) was added, and the mixtures were stirred at 40 °C for approximately 15 min. Water was then added dropwise until complete precipitation of the bis (trifluoromethanesulfonyl)imide salts occurred. The products were obtained as white solids. HPLC-MS analysis confirmed the identity of the compound and the absence of significant organic impurities. **5-(3,4-bis(tetradecyloxy)phenyl)-1,4-dimethyl-3-(perfluoroheptyl)-1H-1,2,4-triazol-4-ium trifluoromethanesulfonate [Tr-7,p-m14][$NTf_2$] (8)**: white solid. Yield = 91%. $^1$H NMR (300 MHz, Acetone-d6) δ: 7.51 (dd, J= 8.7, 1.6 Hz, 1H, Har), 7.45 (d, J = 1.4 Hz, 1H, Har), 7.38 (d, J = 8.4 Hz, 1H, Har), 4.30 (s, 3H, N-$CH_3$), 4.24 – 4.14 (m, 5H, $OCH_2$ + N-$CH_3$), 4.09 (t, J= 6.2 Hz, 2H, $OCH_2$), 1.95 –1.75 (m, 4H, $CH_2$), 1.63 –1.20 (m, 44H, $CH_2$), 0.88 (t, J= 5.8 Hz, 6H, $CH_3$). HRMS: m/z = calcd for $C_{45}H_{67}F_{15}N_3O_2$ $[M]^+$ 966.4988; found 966.5004. **5-(3,5-bis (tetradecyloxy)phenyl)-1,4-dimethyl-3-(perfluoroheptyl)-1H-1,2,4-triazol-4-ium trifluoromethanesulfonate [Tr-7,m-m14] [$NTf_2$] (9)**: white solid. Yield = 80%. $^1$H NMR (300 MHz, CDCl3) δ: 6.80 (s, 3H, Har), 4.12 (s, 3H, N-$CH_3$), 4.07 (t, J = 8.3 Hz, 2H, $OCH_2$), 4.00 (t, J = 5.5 Hz, 2H, $OCH_2$), 3.93 (s, 3H, N-$CH_3$), 1.86 – 1.73 (m, 4H, $CH_2$), 1.51 – 1.21 (m, 44H, $CH_2$), 0.87 (t, J = 6.6 Hz, 6H, $CH_3$). HRMS: m/z = calcd for $C_{45}H_{67}F_{15}N_3O_2$ $[M]^+$ 966.4988; found 966.4994.

### 2.10. Synthesis of Hexafluorophosphate Salts

In separate 50 mL flasks, methyl triflate salts (80 mg; 0.08 mmol) were dissolved in methanol (5 mL). Ammonium hexafluorophosphate (3.5 mol eq.) was added, and the mixtures were stirred at 40 °C for approximately 15 min. Water was then added dropwise until complete precipitation of the hexafluorophosphate salts occurred. The products were obtained as white solids. HPLC-MS analysis confirmed the identity of the compound and the absence of significant organic impurities. **5-(4-(tetradecyloxy)phenyl)-1,4-dimethyl-3-(perfluoroheptyl)-1H-1,2,4-triazol-4-ium trifluoromethanesulfonate [Tr-7,p14][$PF_6$] (10)**: white solid. Yield = 63%. $^1$H NMR (300 MHz, Acetone-d6) δ: 7.90 (d, J = 8.8 Hz, 2H, Har), 7.37 (d, J = 8.8 Hz, 2H, Har), 4.28 (s, 3H, N-$CH_3$), 4.20 (t, J = 6.5 Hz, 2H, $OCH_2$), 4.15 (s, 3H, N-$CH_3$), 1.92 – 1.78 (m, 2H, $CH_2$), 1.57 – 1.24 (m, 22H, $CH_2$), 0.87 (t, J = 6.4 Hz, 3H, $CH_3$).
HRMS: m/z = calcd for $C_{31}H_{39}F_{15}N_3O$ $[M]^+$ 754.2848; found 754.2854. **5-(3,4-bis(tetradecyloxy)phenyl)-1,4-dimethyl-3-(perfluoroheptyl)-1H-1,2,4-triazol-4-ium trifluoromethanesulfonate [Tr-7,p-m14][$PF_6$] [11]**: white solid. Yield = 89%. 1H NMR (300 MHz, CD3CN) δ: 7.23 (s, 2H, Har), 7.10 (s, 1H, Har), 4.12 (t, J = 6.3 Hz, 2H, $OCH_2$), 4.04 (t, J = 6.2 Hz, 2H, $OCH_2$), 4.00 (s, 3H, N-$CH_3$), 3.81 (s, 3H, N-$CH_3$), 1.89 – 1.73 (m, 4H, $CH_2$), 1.59 – 1.20 (m, 44H, $CH_2$), 0.88 (t, J = 6.4 Hz, 6H, $CH_3$). HRMS: m/z = calcd for $C_{45}H_{67}F_{15}N_3O_2$ $[M]^+$ 966.4988; found 966.5011. **5-(3,5-bis(tetradecyloxy)phenyl)-1,4-dimethyl-3-(perfluoroheptyl)-1H-1,2,4-triazol-4-ium trifluoromethanesulfonate [Tr-7,m-m14][$PF_6$] (12)**: white solid. Yield = 51%. $^1$H NMR (300 MHz, CD3CN δ: 6.87 (t, J = 1.8 Hz, 1H, Har), 6.72 (d, J = 1.9 Hz, 2H, Har), 4.04 (t, J = 6.6 Hz, 4H, $OCH_2$), 4.01 (s, 3H, N-$CH_3$), 3.81 (s, 3H, N-$CH_3$), 1.84 – 1.70 (m, 4H, $OCH_2$), 1.52 – 1.23 (m, 44H, $CH_2$), 0.88 (t, J = 6.4 Hz, 6H, $CH_3$). HRMS: m/z = calcd for $C_{45}H_{67}F_{15}N_3O_2$ $[M]^+$ 966.4988; found 966.4996.

## 3. Results and Discussion

### 3.1. Synthesis of ILCs

ILCs were prepared following the multistep sequence shown in **Scheme 2**. Starting from piperonal, the amidoxime precursor (2) was obtained and converted into the corresponding 1,2,4-oxadiazole (3) by reaction with the selected perfluoroacyl chloride. Treatment of this oxadiazole with methylhydrazine induced an ANRORC-type transformation leading to formation of the 1,2,4-triazole scaffold (4). The reaction of triazole (4) with $BBr_3$ cleaved the methylenedioxy (acetal) unit to give the corresponding di-hydroxy intermediate (5). This intermediate (5) was alkylated with tetradecyl halide to deliver the dialkyloxy-phenyl 1,2,4-triazoles [Tr -7,p-m14] (6). Final *N*-methylation with methyl trifluoromethanesulfonate produced the corresponding triazolium triflate salt [Tr-7,p-m14][OTf] (7). Consistent with prior reports, methylation of these 3,4-disubstituted 1,2,4-triazoles proceeds

preferentially at the less sterically hindered and more nucleophilic N(4) site [11]. As noted above, two triazolium triflates used in this study were prepared following previously published procedures [11,21]. A third triazolium triflate was synthesized according to the workflow described in Section 2.8. All the three triflate salts were then employed as precursors in the anion-exchange protocol described here. As shown in **Scheme 3**, the three triazolium triflates were converted, by metathesis, into five distinct triazolium salts through replacement of $OTf^-$ with either $NTf_2$- or $PF_6^-$. The products of these transformations are two $NTf_2^-$ salts, [Tr-7,p-m14][$NTf_2$] (8) and [Tr-7,m-m14][NTf2] (9), and three $PF_6$ salts, [Tr-7,p14][$PF_6$] (10), [Tr-7,p-m14][$PF_6$] (11) and [Tr-7,m-m14][$PF_6$] (12) (see **Scheme 3** for the general reaction representation). By converting a common triazolium triflate platform into salts with markedly different counter-ions, the metatheses provide a controlled approach to probe how anion nature ($NTf_2^-$ vs $PF_6^-$ vs $OTf^-$) modulates mesomorphic windows, thermal transitions and ionic interactions in this class of perfluoroalkyl triazolium ILCs. The DSC and POM data discussed below directly compare the metathesis products with the parent triflate salts in order to isolate the role of the counter-anion in determining phase type, transition temperatures and textural features.

### 3.2. Thermal and *POM* analysis

The thermal behavior of all compounds was examined by DSC and POM. An initial rapid heating scan was carried out to ensure reproducible thermal conditions. Data reported correspond to the first cooling and the second heating scans and were reproducible upon further cycling (see **Figure SM1**, Supporting Information). Transition temperatures, transition enthalpies and the phase changes observed for the six ILCs studied are listed in **Table 1**.

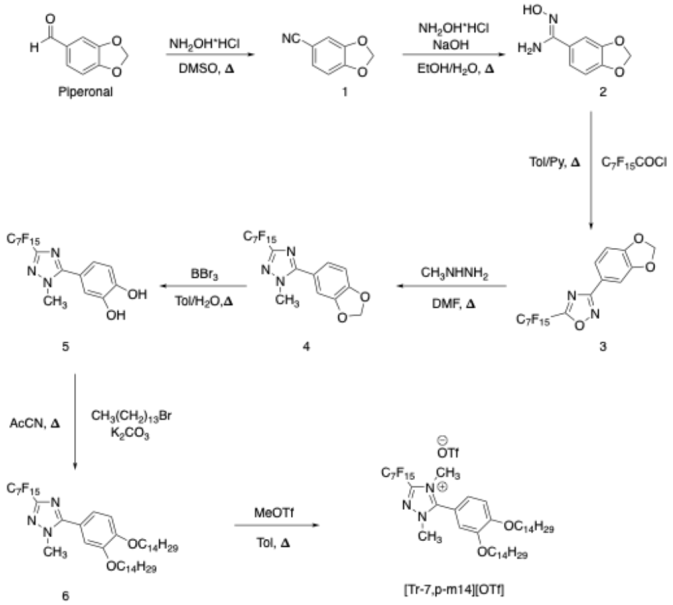


**Scheme 2 |** Synthetic route to triazole precursor 6 and to the related $OTf^-$ salt.

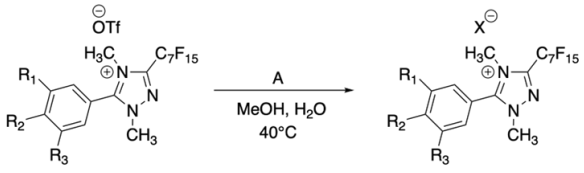


A = $LiNTf_2$ or $NH_4PF_6$

| Name Compound | $R_1$ | $R_2$ | $R_3$ | X |
|---|---|---|---|---|
| [Tr-7,p-m14][$NTf_2$] | -$OC_{14}H_{29}$ | -$OC_{14}H_{29}$ | -H | $NTf_2$ |
| [Tr-7,m-m14][$NTf_2$] | -$OC_{14}H_{29}$ | -H | -$OC_{14}H_{29}$ | $NTf_2$ |
| [Tr-7,p14][$PF_6$] | -H | -$OC_{14}H_{29}$ | -H | $PF_6$ |
| [Tr-7,p-m14][$PF_6$] | -$OC_{14}H_{29}$ | -$OC_{14}H_{29}$ | -H | $PF_6$ |
| [Tr-7,m-m14][$PF_6$] | -$OC_{14}H_{29}$ | -H | -$OC_{14}H_{29}$ | $PF_6$ |

**Scheme 3 |** Synthetic route to Trifluoromethanesulfonate Triazolium Salt.

**Table 1 |** Melting temperatures ($T_m$) and clearing temperatures ($T_c$) along with the corresponding enthalpies (ΔH) of triazolium salts obtained from the DSC traces upon heating and cooling.

| Compound | Heating Cycles | | | Cooling Cycles | | |
|---|---|---|---|---|---|---|
| | $T_m$ (°C)[a] | ΔH (KJ mol$^{-1}$) | Transition[c] | $T_c$ (°C)[b] | ΔH (KJ mol$^{-1}$) | Transition[c] |
| [Tr-7,p14][$PF_6$] (10) | 74.2 | 45.3 | *Cr → LC | | | |
| | 165.7 | 4.5 | LC→ LC' | 193.7 | 4.3 | Iso → LC' |
| | 196.7 | 4.2 | LC' → Iso | 158.7 | 3.4 | LC' → LC |
| [Tr-7,p-m14][OTf] (7) | | | | 146.9 | 5.53 | Iso → LC" |
| | 77.9 | 19.5 | Cr → LC | 116.3 | 0.6 | LC" → LC' |
| | 117.8 | 0.8 | LC → LC' | 80.4 | 6.1 | LC' → LC |
| | 146.5 | 5.6 | LC' → Iso | 67.2 | 7.1 | LC → Cr |
| [Tr-7,p-m14][$NTf_2$] (8) | 46.7 | 35.2 | Cr → LC | 112.2 | 2.0 | Iso → LC' |
| | 80.2 | 3.9 | LC → LC' | 70.8 | 3.4 | LC' → LC |
| | 115.7 | 3.5 | LC' → Iso | 41.2 | 34.2 | LC → Cr |
| [Tr-7,p-m14][$PF_6$] (11) | 22.7 | 13.7 | Cr → LC | 176.4 | 3.4 | Iso → LC' |
| | 171.6 | 12.2 | LC → Iso | 167.5 | 3.7 | LC' → LC |
| | | | | 25.1 | 15.6 | LC → Cr |
| [Tr-7,m-m14][$NTf_2$] (9) | -8.3 | 6.5 | Cr → Cr' | 67.3 | 2.9 | Iso → LC |
| | 11.6 | 4.2 | Cr' → Cr" | 32.5 | 6.6 | LC → Cr" |
| | 33.9 | 3.6 | Cr" → LC | 7.2 | 4.3 | Cr" → Cr' |
| | 54.7 | 16.5 | LC → Iso | -7.7 | 4.6 | Cr' → Cr |
| [Tr-7,m-m14][$PF_6$] (12) | 6.7 | - | Cr → G | 138.2 | 2.9 | Iso → LC |
| | 132.7 | 20.6 | G → LC | 126.7 | 8.5 | LC → G |
| | 141.2 | ** | LC → Iso | 3.1 | - | G → Cr |

[a] Transitions refer to the second heating cycles. Temperatures indicate the onset of each peak.

[b] Transitions refer to the first cooling cycles. Temperatures indicate the onset of each peak.

[c] Abbreviations: Iso - isotropic phase; LC - liquid crystalline phase; G - glass transition and Cr - crystalline solid state.

*Transition observed only after the first heating cycle and not detected in subsequent cycles.

** ΔH value is not reported due to broadening and overlapping DSC signals.

In all cases more than one transition can be observed from DSC traces both during heating and cooling ramps (**Figures 1 and 2**). For 4-substituted salt [Tr-7,p14][$PF_6$] (10), three transitions are detected during the first heating, though one of these events disappears from all subsequent heating cycles. From the second heating onward, the thermogram displays only two reproducible mesophase transitions, LC → LC' and LC' → Iso, indicating that the system adopts a stable mesomorphic sequence after the initial thermal activation. Upon cooling the material undergoes the Iso → LC' transition at the clearing temperature, followed by an internal reorganization within the mesophase (LC' → LC) (**Figure 1**), without reaching a crystalline ordered phase in the range of scanned temperature. The disappearance of the Cr → LC event after the first heating, combined with the fully reproducible mesophase behavior observed thereafter, is consistent with an irreversible rearrangement of the initial solid-state packing during the first thermal excursion. Similar transitions detectable exclusively in the initial heating cycle have been reported for both low molecular weight liquid crystals and ionic mesogens, where metastable crystalline domains convert into a more stable organization upon heating, eliminating the corresponding transition in subsequent scans [22,23]. [Tr-7,p-m14][OTf] (7) produced a multi-step thermotropic behavior. On heating, the $OTf^-$ salt undergoes a Cr → LC transition, followed by a LC → LC' reorganization and a final LC' → Iso clearing. The relatively large enthalpy of the low-temperature Cr → LC step indicates substantial loss of crystalline order upon entry into the first mesophase, whereas the small enthalpy for the LC → LC' step is typical of intramesophase rearrangements involving changes in lateral packing without gross positional disordering. During cooling the isotropic melt first forms a higher-temperature mesophase (Iso → LC''), which subsequently transforms to the lower-temperature mesophases sequence (LC'' → LC', LC' → LC) before finally crystallizing (LC → Cr). The cooling data show that the system accesses a succession of ordered states on cooling that mirror, in reverse, the heating reorganizations. The differences in onset temperatures and enthalpies indicate modest hysteresis and suggest that the LC↔LC' conversions are reversible but kinetically hindered to some extent. Overall, the $OTf^-$ salt displays clear multistep mesomorphic behavior in both scan directions, consistent with competing packing motifs stabilized by the relatively small coordinating $OTf^-$ anion [1,24] (**Figure 2**). The $NTf_2^-$ analogue showed three transitions on heating, which can be attributed to Cr → LC, LC → LC', and LC' → Iso. The very large enthalpy associated with the low-temperature crystalline loss suggests entry into a well-ordered mesophase with substantial disruption of the original crystalline lattice. On cooling the reverse sequence is observed: Iso → LC', LC' → LC and LC → Cr. The comparable magnitude of the crystallization enthalpy on cooling and the melting-like enthalpy on heating supports the assignment of a well-defined LC phase that forms and disappears with significant latent heat. The $NTf_2^-$ anion, being bulky and highly delocalized, often reduces ion pairing and enhances fluidity, which can stabilize distinct mesophases separated by modest LC ↔ LC' enthalpies [1,25]. This behavior is consistent with the clear, well-separated transitions observed here. The modest hysteresis between heating and cooling for the LC ↔ LC' steps suggests that these reorganizations are near-thermodynamic in nature but still subject to finite nucleation barriers (**Figure 2**) [26]. For [Tr-7,p-m14][$PF_6$] (11) the heating trace shows a low-temperature Cr → LC event and a single higher-temperature LC → Iso clearing, indicating a large mesomorphic stability window on heating. The cooling cycle, however, reveals a more complex path going from Iso → LC', LC' → LC to LC → Cr.

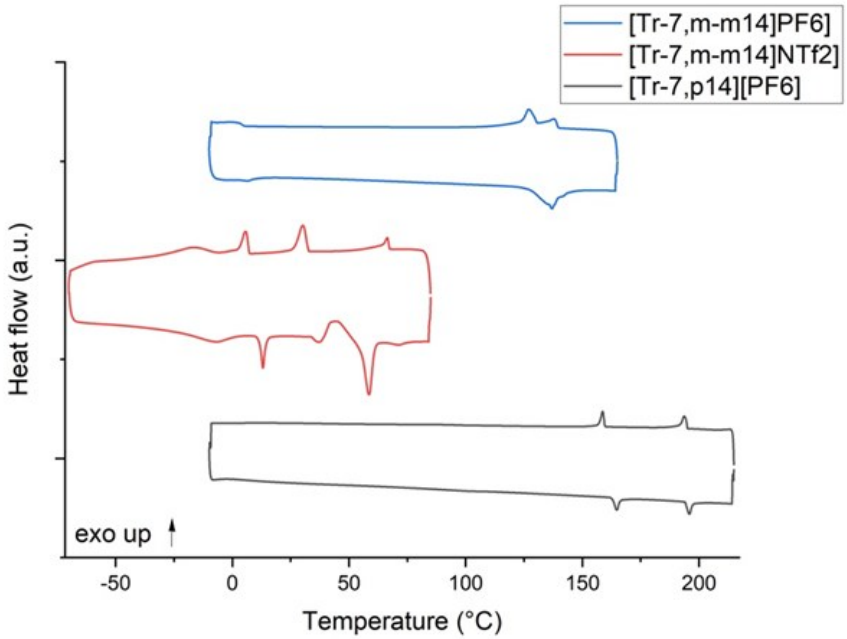


**Figure 1 |** DSC traces of $PF_6^-$ and $NTf_2^-$ triazolium salts. DSC traces of the 4- and 3,5-substituted $PF_6^-$ and $NTf_2^-$ triazolium salts, showing the main crystalline-mesophase transitions observed on heating and cooling.

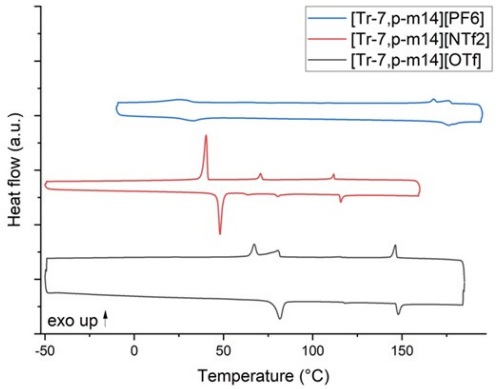


**Figure 2 |** DSC traces of $OTf^-$, $NTf_2^-$ and $PF_6^-$ triazolium salts. DSC traces of the p-m substituted $OTf^-$, $PF_6^-$ and $NTf_2^-$ triazolium salts, highlighting the multi-step mesophase behaviors and the counter-ion–dependent transition profiles.

The difference between the heating trace and the cooling one either suggests that certain mesophase reorganizations are kinetically accessible primarily upon cooling or small enthalpy LC ↔ LC' events may be masked by broadened baselines on heating. The $PF_6^-$ anion, being more compact and less polarizable than $NTf_2^-$, probably tends to favor tighter ionic lattices and may restrict the mobility needed for some mesophase transformations during heating, hence producing the observed difference (**Figure 2**). [Tr-7,m-m14][$NTf_2$] (9) presents a sequence of low-temperature solid–solid transitions on heating (Cr → Cr', Cr' → Cr''), followed by Cr → LC and LC → Iso. The cooling run reproduces the mesophase formation (Iso → LC), followed by LC → Cr'', Cr'' → Cr and Cr' → Cr. The comparatively low temperatures and moderate enthalpies of the Cr → LC and LC → Iso steps indicate modest mesophase stability, consistent with m–m substitution producing less favorable mesomorphic packing than 4-substituted isomers (**Figure 1**). [Tr-7,m-m14][$PF_6$] (12) shows a low-temperature glass transition, followed on heating by Cr' → LC and LC → Iso. On cooling, the system passes from Iso → LC to LC → Cr' and finally Cr' → Cr. The presence of a glass transition suggests that at low temperatures the system falls out of equilibrium and that recrystallization might be kinetically limited. However, the formation of a mesophase with substantial enthalpy (Cr' → LC) indicates robust mesomorphic ordering at elevated temperatures. The high-temperature mesophase window and the relative magnitudes of ΔH on heating and cooling align with $PF_6^-$ favoring well-defined but possibly less fluid mesophases compared with $NTf_2^-$ analogues (**Figure 1**). A comparison of the transition temperatures of the newly synthesized compounds with those of the corresponding analogues previously reported in the literature [11,21] confirms the strong influence of the counter-ion on the mesophase behaviors. Moving from the smallest anion $PF_6^-$ to the larger one $NTf_2^-$ resulted in a decrease of both melting and clearing temperatures. The stability range of the mesophases also depends on the cation structure. Cations bearing alkyl substituents in the 3,5-positions, which provide a more extended and symmetric shape, displayed narrow mesophase windows, ranging from about 4 °C for the $OTf^-$ salt to about 14 °C for the $NTf_2^-$ salt. By contrast, cations with a single long alkyl chain in the 4-position, or with alkyl chains in the 3,4-positions, present considerably wider mesophase ranges and a larger number of distinct mesophases (**Figure 3**). Phase identification by POM was carried out during heating and cooling ramps and the textures of

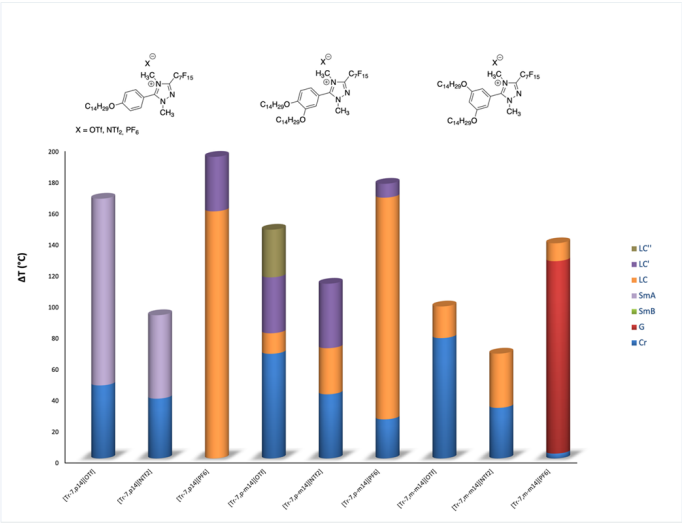


**Figure 3 | Comparative DSC traces and POM analysis with literature analogues.** DSC analysis of the triazolium salts studied in this work together with the previously reported analogues [11,21], recorded during the cooling ramp. The traces highlight the characteristic thermal transitions and phase-change behavior across the different substitution patterns and counter-ion.

the mesophases were examined to understand the liquid-crystalline nature. Materials that showed focal-conic textures under crossed polarizers were identified as smectic mesophases [26,27] (**Figure 4**), while marble-like textures, characteristic of layered ordering, were observed for compounds bearing two long alkyl chains (**Figure 5**). By the POM analysis, single-chain (4-substituted) derivatives showed focal-conic textures, ascribable to smectic phases. In particular, a SmA-like on cooling from the isotropic liquid was observed in [Tr-7,p-14][$PF_6$] (10), and a further transition (SmA ↔ SmB) at lower temperature (105 °C). This interpretation is consistent with previous reports on triazolium and other ionic liquid crystals [2,21]. On the other hand, it is noteworthy that [Tr-7,p-m14][$PF_6$] (11), [Tr-7,p-m14][OTf] (7) and [Tr-7,m-m14][$PF_6$] (12) exhibited dendritic growth on cooling from the isotropic liquid, a behavior commonly associated with discotic mesophases and consistent with supramolecular aggregation of the mesogens into disk-like assemblies.

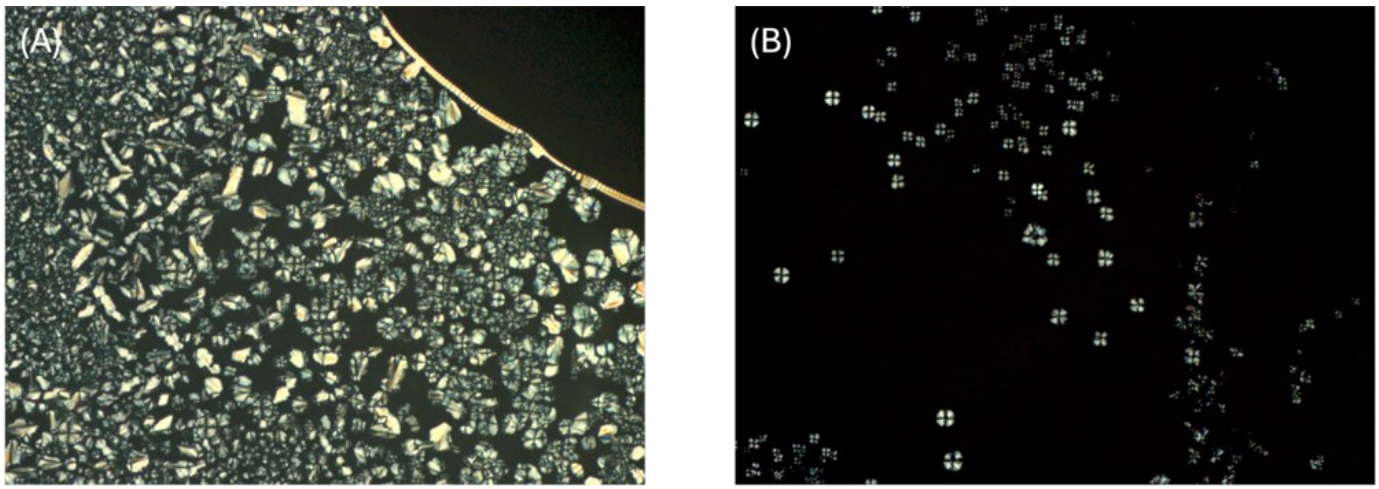


**Figure 4 |** Focal-conic textures. Microphotographs of selected focal conic textures observed in the studied materials, obtained upon cooling from the isotropic liquid. (A) SmB mesophase of [Tr-7,p14][$PF_6$] (10) recorded at 105 °C (200x). (B) SmA mesophase of [Tr-7,p14][$PF_6$] (10) recorded at 197 °C (200x).

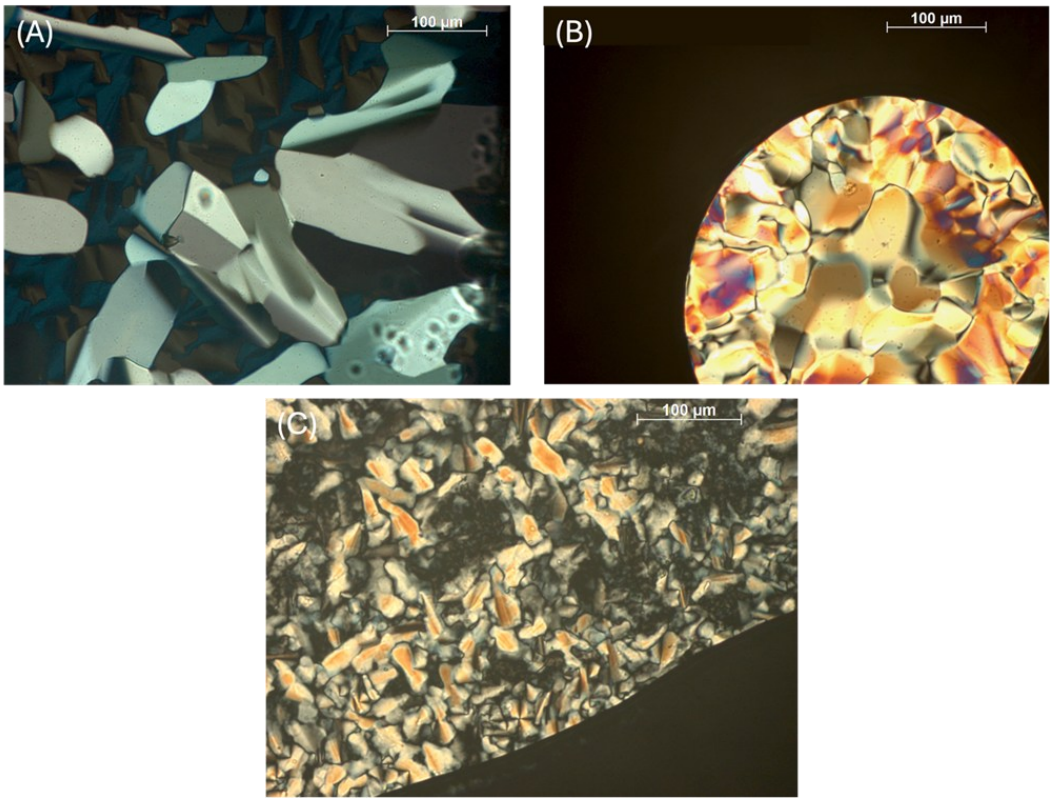


**Figure 5 |** Marble-like textures. Microphotographs of selected marble-like textures observed in the studied materials, obtained upon cooling from the isotropic liquid. (A) LC mesophase of [Tr-7,p-m14][OTf] (7) recorded at 149 °C (100x). (B) LC mesophase of [Tr-7,p-m14][$PF_6$] (11) recorded at 172.7 °C (100x). (C) LC' mesophase of [Tr-7,m-m14][$PF_6$] (12) recorded at 138 °C (200x).

## Concluding Remarks

Six ILCs derived from 3-perfluoroalkyl-1,2,4-triazolium cores were synthesized and characterized to assess how thermal behavior is affected by counter-ion and by the alkyl substitution pattern on the phenyl ring. DSC results showed a systematic trend: for the series studied, $NTf_2^-$ derivatives generally present lower melting and clearing temperatures than their corresponding $PF_6^-$ analogues. Mesophase stability and the number of observed mesophases are cation dependent and strongly influenced by the alkyl substitution pattern on the phenyl ring. Cations bearing two alkyl chains in the 3,5-positions display relatively narrow mesophase windows, whereas cations with a single long chain at the 4-position or with 3,4-substitution exhibit broader mesophase ranges and a larger number of distinct transitions. POM observations can give information about LC transition nature: single-chain (4-substituted) derivatives show focal-conic textures consistent with smectic phases, while dialkyloxy derivatives give marble-type textures. Notably, dendritic growth on cooling from the isotropic liquid was observed in [Tr-7,p-m14][$PF_6$] (11), [Tr-7,p-m14][OTf] (7) and [Tr-7,m-m14][$PF_6$] (12), morphologies consistent with discotic-type supramolecular aggregation. These results indicate that the interplay between cation shape and anion volume determines not only the onset temperatures of mesophase formation but also the accessibility of intramesophase reorganizations (LC ⟷ LC', SmB ⟷ SmA). Broad, stable mesophase windows are favored by 4-substitution and by the $NTf_2^-$ anion, whereas $PF_6^-$ and more symmetric 3,5-substituted cations stabilize narrower, higher-temperature mesophase regimes. Enthalpy changes can further support these assignments, with larger ΔH values marking transitions between crystalline and mesomorphic states, and smaller ΔH values characterizing orientational rearrangements within the liquid-crystalline phases. Overall, these findings underscore that selective anion exchange combined with controlled cation substitution provides an effective strategy to tune mesophase type, thermal stability, mesophase breadth, and the richness of phase sequences in triazolium-based ionic liquid crystals. The structure-mesophase relationships identified here offer directly transferable criteria for designing fluorinated ionic liquid crystals as functional materials in anisotropic electrolytes, directional ion-transport systems for devices in which fine control of mesophase windows and supramolecular order is crucial.

## Supplementary Material

The following supplementary material is available: **Table SM1**: LDSC analysis of the p-m substituted $OTf^-$, $PF_6^-$ and $NTf_2^-$ triazolium salts, highlighting the multistep mesophase behavior, the counterion-dependent transition profiles, and the reproducibility across multiple heating-cooling cycles.

## Author contributions

Conceptualization, I.P.; Methodology, I.P., A.P.; Formal analysis, I.P. C.R. and I.F.; Investigation, I.F., D.R., C.R.; Writing—original draft, I.F., C.R.; Writing—review & editing, I.P., C.R., D.R.; Visualization, A.P., D.R.; Supervision, I.P.; Funding acquisition, I.P. All authors have read and agreed to the published version of the manuscript.

## Acknowledgements

The University of Palermo is gratefully acknowledged.

## References

[1] K.V. Axenov, S. Laschat, Thermotropic Ionic Liquid Crystals, Materials (Basel) 4 (2011) 206–259. https://doi.org/10.3390/ma4010206.

[2] K. Goossens, K. Lava, C.W. Bielawski, K. Binnemans, Ionic Liquid Crystals: Versatile Materials, Chem Rev 116 (2016) 4643–4807. https://doi.org/10.1021/cr400334b.

[3] N. Kapernaum, A. Lange, M. Ebert, M.A. Grunwald, C. Haege, S. Marino, A. Zens, A. Taubert, F. Giesselmann, S. Laschat, Current Topics in Ionic Liquid Crystals, Chempluschem 87 (2022) e202100397. https://doi.org/10.1002/cplu.202100397.

[4] A. Abate, A. Petrozza, G. Cavallo, G. Lanzani, F. Matteucci, D.W. Bruce, N. Houbenov, P. Metrangolo, G. Resnati, Anisotropic ionic conductivity in fluorinated ionic liquid crystals suitable for optoelectronic applications, J. Mater. Chem. A 1 (2013) 6572–6578. https://doi.org/10.1039/C3TA10990A.

[5] M. Hird, Fluorinated liquid crystals--properties and applications, Chem Soc Rev 36 (2007) 2070–2095. https://doi.org/10.1039/b610738a.

[6] Q. Ruan, M. Yao, D. Yuan, H. Dong, J. Liu, X. Yuan, W. Fang, G. Zhao, H. Zhang, Ionic liquid crystal electrolytes: Fundamental, applications and prospects, Nano Energy 106 (2023) 108087. https://doi.org/10.1016/j.nanoen.2022.108087.

[7] A.F.M. Santos, J.L. Figueirinhas, M. Dionísio, M.H. Godinho, L.C. Branco, Ionic Liquid Crystals as Chromogenic Materials, Materials 17 (2024) 4563. https://doi.org/10.3390/ma17184563.

[8] S . Buscemi, A. Pace, I. Pibiri, N. Vivona, D. Spinelli, Fluorinated heterocyclic compounds. An expedient route to 5-perfluoroalkyl-1,2,4-triazoles via an unusual hydrazinolysis of 5-perfluoroalkyl-1,2,4-oxadiazoles: first examples of an ANRORC-like reaction in 1,2,4-oxadiazole derivatives, J Org Chem 68 (2003) 605–608. https://doi.org/10.1021/jo0262762.

[9] F. Lo Celso, I. Pibiri, A. Triolo, R. Triolo, A. Pace, S. Buscemi, N. Vivona, Study on the thermotropic properties of highly fluorinated 1,2,4-oxadiazolylpyridinium salts and their perspective applications as ionic liquid crystals, Journal of Materials Chemistry 17 (2007) 1201–1208. https://doi.org/10.1039/b615190f.

[10] A. Riccobono, R.R. Parker, A.C. Whitwood, J.M. Slattery, D.W. Bruce, I. Pibiri, A. Pace, 1,2,4-Triazolium ions as flexible scaffolds for the construction of polyphilic ionic liquid crystals, Chemical Communications 54 (2018) 9965–9968. https://doi.org/10.1039/c8cc04704a.

[11] A. Riccobono, G. Lazzara, S.E. Rogers, I. Pibiri, A. Pace, J.M. Slattery, D.W. Bruce, Synthesis and mesomorphism of related series of triphilic ionic liquid crystals based on 1,2,4-triazolium cations, Journal of Molecular Liquids 321 (2021) 114758. https://doi.org/10.1016/j.molliq.2020.114758.

[12] M.S. Weber, M. Schulze, G. Lazzara, A.P. Piccionello, A. Pace, I. Pibiri, Oxadiazolyl-pyridinium as cationic scaffold for fluorinated ionic liquid crystals†, Applied Sciences (Switzerland) 11 (2021). https://doi.org/10.3390/app112110347.

[13] S. Buscemi, A. Pace, A.P. Piccionello, I. Pibiri, N. Vivona, G. Giorgi, A. Mazzanti, D. Spinelli, Five-to-six membered ring-rearrangements in the reaction of 5-perfluoroalkyl-1,2,4-oxadiazoles with hydrazine and methylhydrazine, Journal of Organic Chemistry 71 (2006) 8106–8113. https://doi.org/10.1021/jo061251e.

[14] I. Pibiri, A. Pace, S. Buscemi, N. Vivona, L. Malpezzi, Designing fluorous domains. synthesis of a series of pyridinium salts bearing a perfluoroalkylated azole moiety, Heterocycles 68 (2006) 307–321. https://doi.org/10.3987/COM-05-10633.

[15] I. Zama, G. Gorni, V. Borzatta, M.C. Cassani, C. Crupi, G. Di Marco, Fluorinated imidazolium salts having liquid crystal characteristics, Journal of Molecular Liquids 223 (2016) 749–753. https://doi.org/10.1016/j.molliq.2016.08.101.

[16] G. Cavallo, G. Terraneo, A. Monfredini, M. Saccone, A. Priimagi, T. Pilati, G. Resnati, P. Metrangolo, D.W. Bruce, Superfluorinated Ionic Liquid Crystals Based on Supramolecular, Halogen-Bonded Anions, Angew Chem Int Ed Engl 55 (2016) 6300–6304. https://doi.org/10.1002/anie.201601278.

[17] G. Cavallo, A. Abate, M. Rosati, G. Paolo Venuti, T. Pilati, G. Terraneo, G. Resnati, P. Metrangolo, Tuning of Ionic Liquid Crystal Properties by Combining Halogen Bonding and Fluorous Effect, Chempluschem 86 (2021) 469–474. https://doi.org/10.1002/cplu.202100046.

[18] A. Riccobono, A.C. Whitwood, R.R. Parker, S. Hart, A. Pace, J.M. Slattery, I. Pibiri, D.W. Bruce, Crystal and molecular structure of series of triphilic ionic liquid-crystalline materials based on the 1,2,4-triazolium cation, CrystEngComm 100 (2022). https://doi.org/10.1039/d2ce01354a.

[19] C. Tschierske, Liquid crystals: materials design and self-assembly, Springer Science & Business Media, 2012.

[20] G. Saielli, T. Margola, K. Satoh, Tuning Coulombic interactions to stabilize nematic and smectic ionic liquid crystal phases in mixtures of charged soft ellipsoids and spheres, Soft Matter 13 (2017) 5204–5213. https://doi.org/10.1039/c7sm00612h.

[21] C. Rizzo, I. Fiduccia, S. Buscemi, A. Palumbo Piccionello, A. Pace, I. Pibiri, Shaping 1,2,4-Triazolium Fluorinated Ionic Liquid Crystals, Applied Sciences (Switzerland) 13 (2023). https://doi.org/10.3390/app13052947.

[22] D.M. Duarte, R. Richert, K. Adrjanowicz, Watching the Polymorphic Transition from a Field-Induced to a Stable Crystal by Dielectric Techniques, Crystal Growth & Design 20 (2020) 5406–5412. https://doi.org/10.1021/acs.cgd.0c00626.

[23] W. Cao, Y. Wang, Phase Behaviors of Ionic Liquids Heating from Different Crystal Polymorphs toward the Same Smectic-A Ionic Liquid Crystal by Molecular Dynamics Simulation, Crystals 9 (2019) 26. https://doi.org/10.3390/cryst9010026.

[24] N.V. Ignat'ev, P. Barthen, A. Kucheryna, H. Willner, P. Sartori, A Convenient Synthesis of Triflate Anion Ionic Liquids and Their Properties, Molecules 17 (2012) 5319–5338. https://doi.org/10.3390/molecules17055319.

[25] F. Philippi, T. Welton, Targeted modifications in ionic liquids - from understanding to design, Phys Chem Chem Phys 23 (2021) 6993–7021. https://doi.org/10.1039/d1cp00216c.

[26] Peter J. Colling, M. Hird, Introduction to Liquid Crystals: Chemistry and Physics, 1st Edition, CRC Press, 1997. https://doi.org/10.1201/9781315272801.

[27] N. Osiecka-Drewniak, Z. Galewski, E. Juszyńska-Gałązka, Distinguishing the Focal-Conic Fan Texture of Smectic A from the Focal-Conic Fan Texture of Smectic B, Crystals 13 (2023) 1187. https://doi.org/10.3390/cryst13081187.